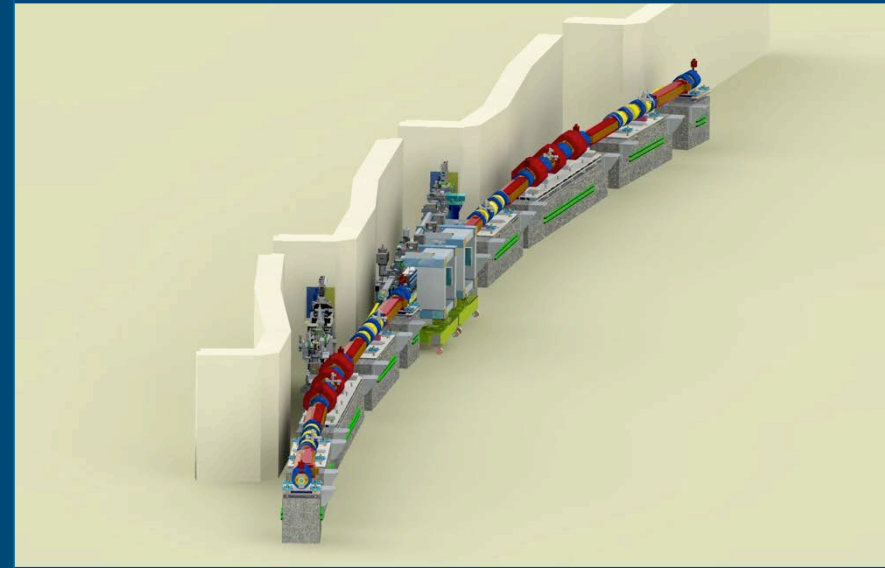


X-ray Optics Considerations for the APS Upgrade



Tim Graber
Physicist

APS Upgrade Forum
November 8, 2017

Specification, Procurement, and Installation

Optics/Components Specifications

- **Optics Simulations**
 - Preserving Brightness/Coherence
 - Maximizing Flux
 - Minimum Focal Spot Size
 - Slope Error
 - Height Error
 - Roughness
 - Crystal Quality
 - Thermal Distortion
 - X-ray Window Quality
- **Mechanical Properties**
 - Experiment Driven
 - Resolutions
 - Repeatability
 - Control System Requirements
 - Feedback Systems
 - Lowest Eigenfrequency
- **Environmental Considerations**
 - Vibration Mitigation
 - Temperature Stability

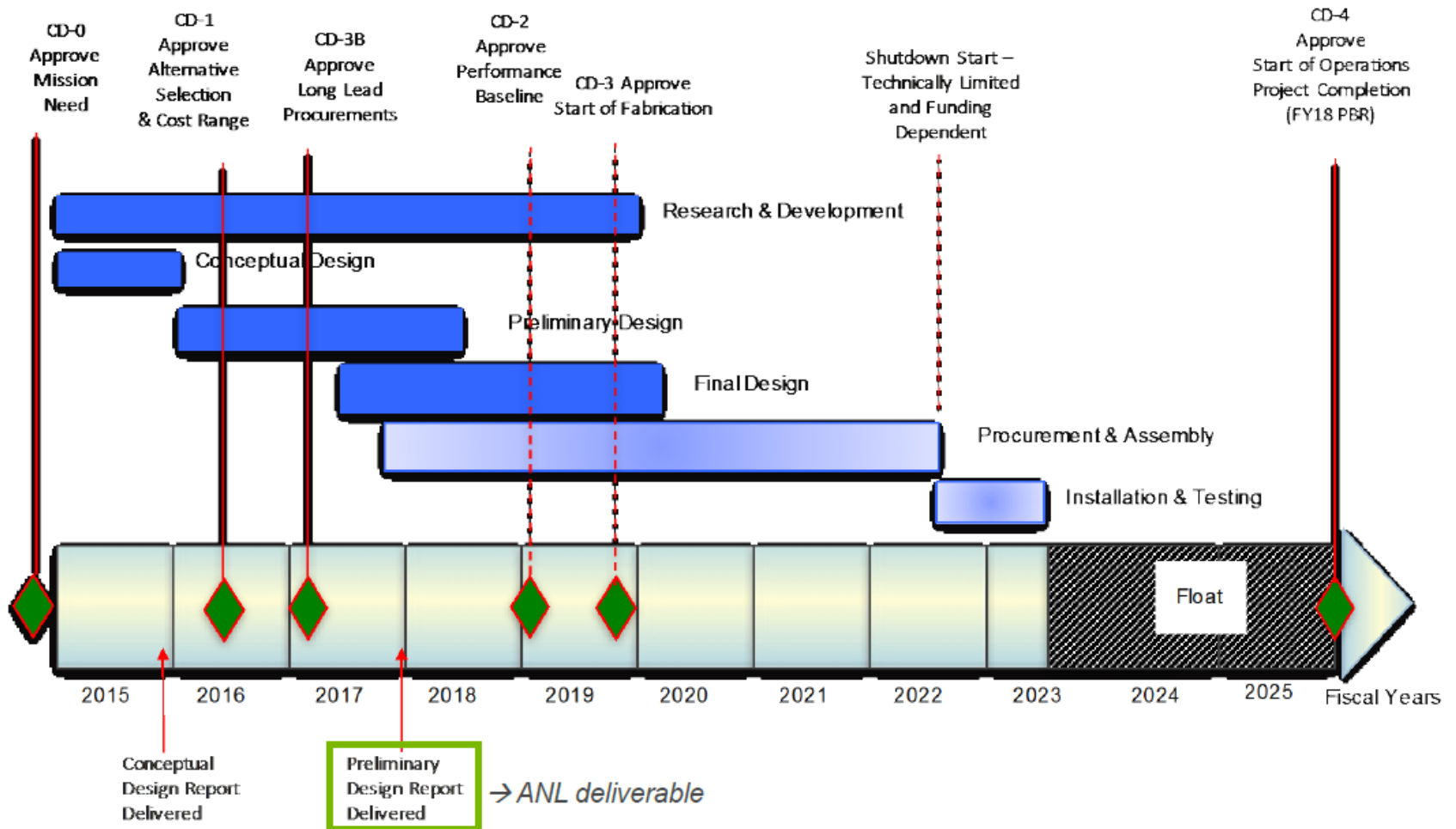
Concept to Hardware on the Floor

- **R&D Activities (28-ID)**
- **Identification of Vendors**
- **Procurement**
 - Statement of Work
 - APS-U Review
 - Request for Proposals
 - Proposal Evaluation
 - Contract Award
 - Vendor Communications
 - Delivery/Installation
- **Acceptance Tests**
- **Commissioning**
- **User Operations**

APS-U Optics Needs

Optics	Featured/Enhanced Beamlines
High-quality wavefront-preserving CRLs and translocators	CHEX, CSSI, XPCS, HEXM, 6-ID, 11-ID, 12-ID, 32-ID, 15-ID
High- and ultra-precise focusing KB mirror systems	3DNano, ATOMIC, CSSI, InSitu, Polar, XPCS, 2-ID, 3-ID, 13-ID, 32-ID
High-heat load mirrors	3DNano, ATOMIC, CSSI, InSitu, Ptychoprobe, XPCS, 2-ID, 7-ID
New single mirror systems	15-ID, 32-ID
Mirror upgrade, repolishing, or replacement	5-ID, 13-ID, 26-ID
New horizontal HHL double-crystal monochromators	3DNano, ATOMIC, CHEX, CSSI, InSitu, Polar, Ptychoprobe, XPCS, 2-ID
Upgrade existing vertical HHL double-crystal monochromators	5-ID, 13-ID, 26-ID, 30-ID, 32-ID
Non-silicon monochromators	CHEX, Polar
High-energy bent-crystal Laue monochromator	HEXM, 1-ID, 11-ID
Zone Plates	Ptychoprobe, 26-ID, BNP-ID
Multi-layer optics	ATOMIC, CSSI, InSitu, XPCS, 25-ID, 32-ID
Ultrahigh-resolution monochromators	27-ID, 30-ID

Project Schedule



- Overall schedule funding dependent
- Project utilizing CD-3B authority to adjust to funding fluctuations as appropriate and with full knowledge of BES

First Test Case for the Specification-Procurement-Installation Cycle

- General Optics LLP Purchase for the Enhancement Program
- Initial Budget Estimate Prepared for CD-3B Review
- Received CD-3B Approval July 2016 for purchases in FY17, FY18, and FY19
- **First Purchase:** Horizontally Deflecting Double-crystal Monochromator for 2-ID

• Optics Simulations

- Preserving Brightness/Coherence
- Maximizing Flux
- Focal Spot Minimization

• Mechanical Properties

- Experiment Driven
- Resolutions
- Repeatability
- Control System Requirements
- Feedback Systems
- Lowest Eigenfrequency



• Identification of Vendors

• Procurement

- Statement of Work
- APS-U Review
- Request for Proposals
- Proposal Evaluation
- Contract Award
- Vendor Communications
- Delivery/Installation

X-ray Optics Simulations

Invited Paper

X-ray optics simulation and beamline design for the APS upgrade

Xianbo Shi^a, Ruben Reininger^a, Ross Harder^a, and Dean Haeffner^a

^aAdvanced Photon Source, Argonne National Laboratory, Argonne, Illinois 60439, USA;

ABSTRACT

The upgrade of the Advanced Photon Source (APS) to a Multi-Bend Achromat (MBA) will increase the brightness of the APS by between two and three orders of magnitude. The APS upgrade (APS-U) project includes a list of feature beamlines that will take full advantage of the new machine. Many of the existing beamlines will be also upgraded to profit from this significant machine enhancement. Optics simulations are essential in the design and optimization of these new and existing beamlines. In this contribution, the simulation tools used and developed at APS, ranging from analytical to numerical methods, are summarized. Three general optical layouts are compared in terms of their coherence control and focusing capabilities. The concept of zoom optics, where two sets of focusing elements (e.g., CRLs and KB mirrors) are used to provide variable beam sizes at a fixed focal plane, is optimized analytically. The effects of figure errors on the vertical spot size and on the local coherence along the vertical direction of the optimized design are investigated.

Keywords: beamline design; X-ray optics simulation; beam coherence; zoom optics;

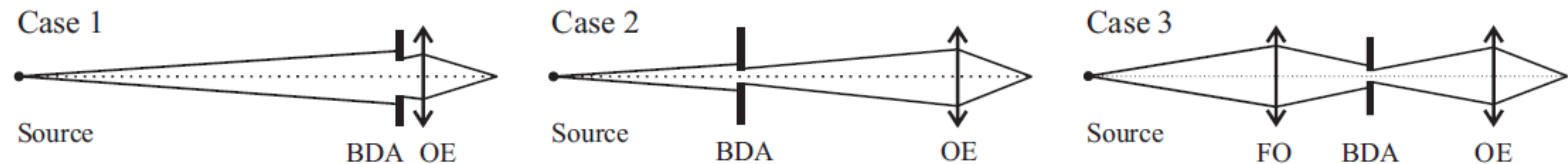


Figure 1. Schematics of three general beamline layouts for beam coherence control and focusing. BDA: beam defining aperture; OE: optical element for focusing; FO: first optics for focusing.

Why a Horizontally Deflecting Monochromator?

- Rumors to the effect that HDCMs are more stable with regard to vibrations
- The horizontal source size will be a factor of ~ 4 larger in high brightness mode (324 bunch). Less sensitive to vibrational source broadening

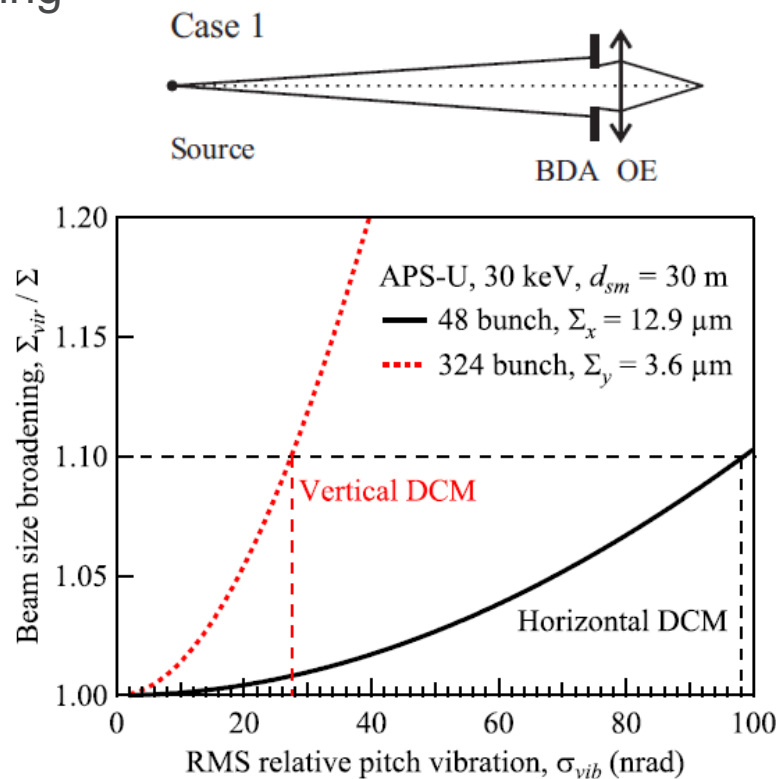
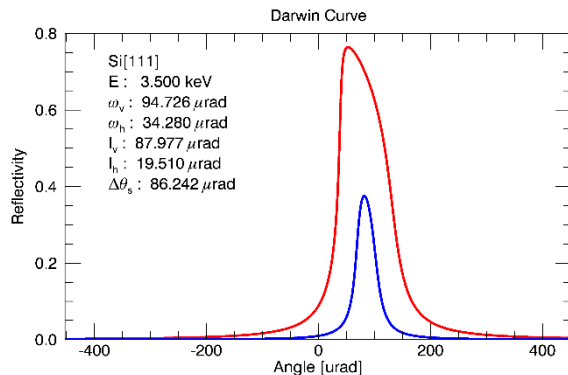
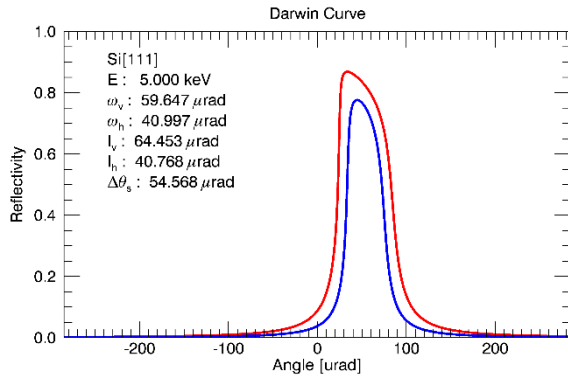
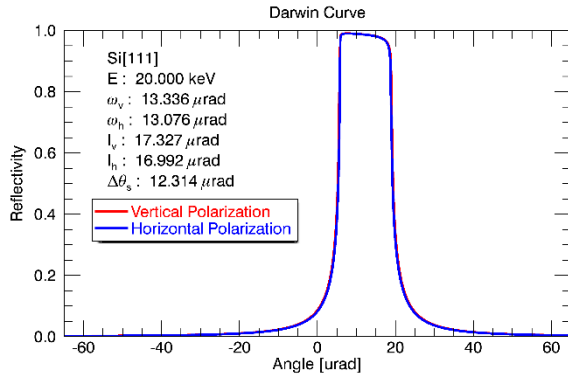


Figure 4. Virtual source size broadening (Σ_{vir}/Σ) as a function of the RMS relative pitch vibration σ_{vib} for a horizontal DCM (solid line) and a vertical DCM (dotted line) at $d_{sm} = 30$ m.

Horizontal vs. Vertical Diffraction for a Horizontally Polarized Source

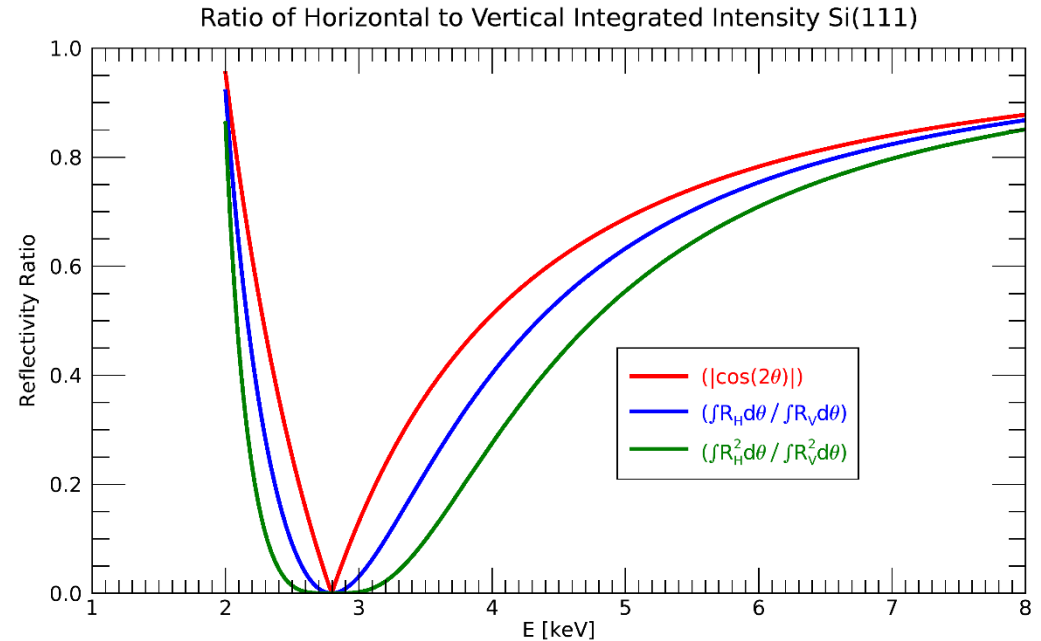


Horizontal vs. Vertical Diffraction for a Horizontally Polarized Source

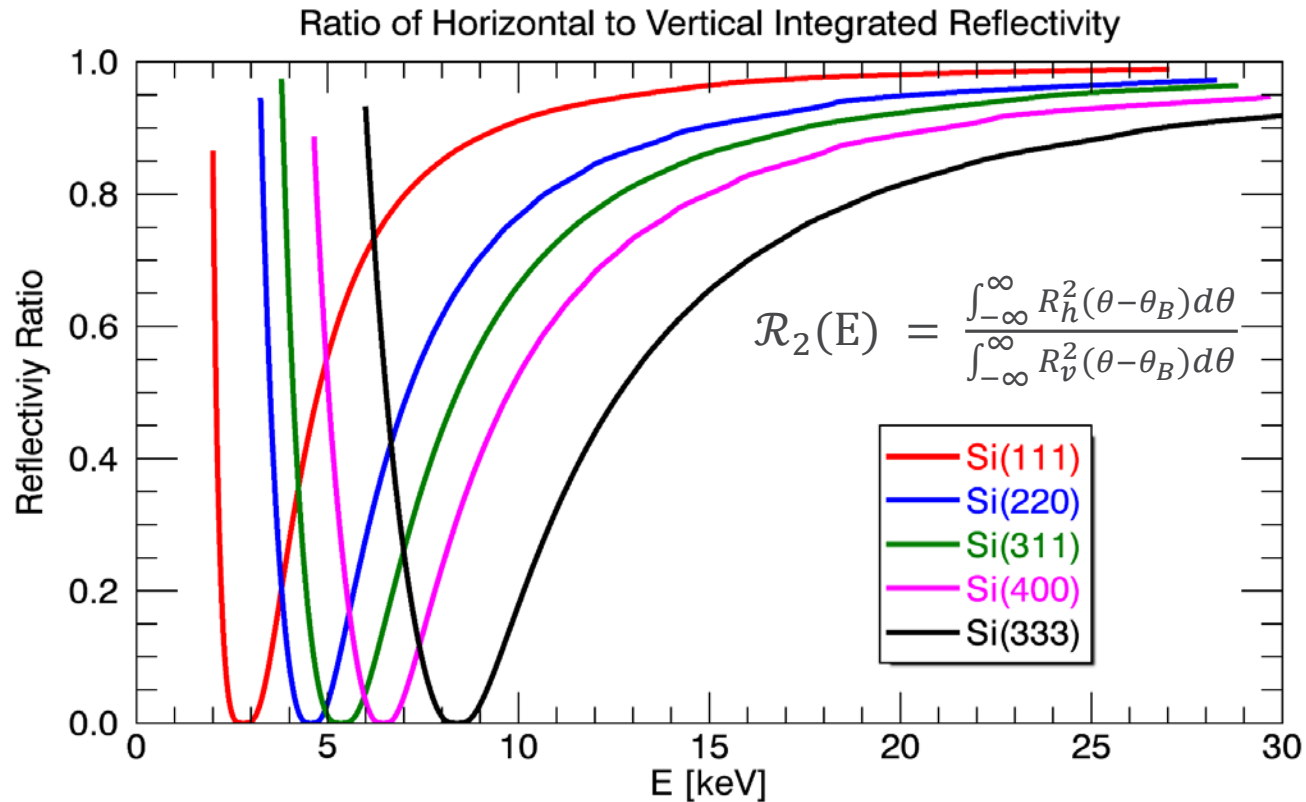
$$\mathcal{R}_0(E) = \frac{I_h}{I_v} = \frac{\omega_h}{\omega_v} = |\cos 2\theta_B|$$

$$\mathcal{R}_1(E) = \frac{\int_{-\infty}^{\infty} R_h(\theta - \theta_B) d\theta}{\int_{-\infty}^{\infty} R_v(\theta - \theta_B) d\theta}$$

$$\mathcal{R}_2(E) = \frac{\int_{-\infty}^{\infty} R_h^2(\theta - \theta_B) d\theta}{\int_{-\infty}^{\infty} R_v^2(\theta - \theta_B) d\theta}$$



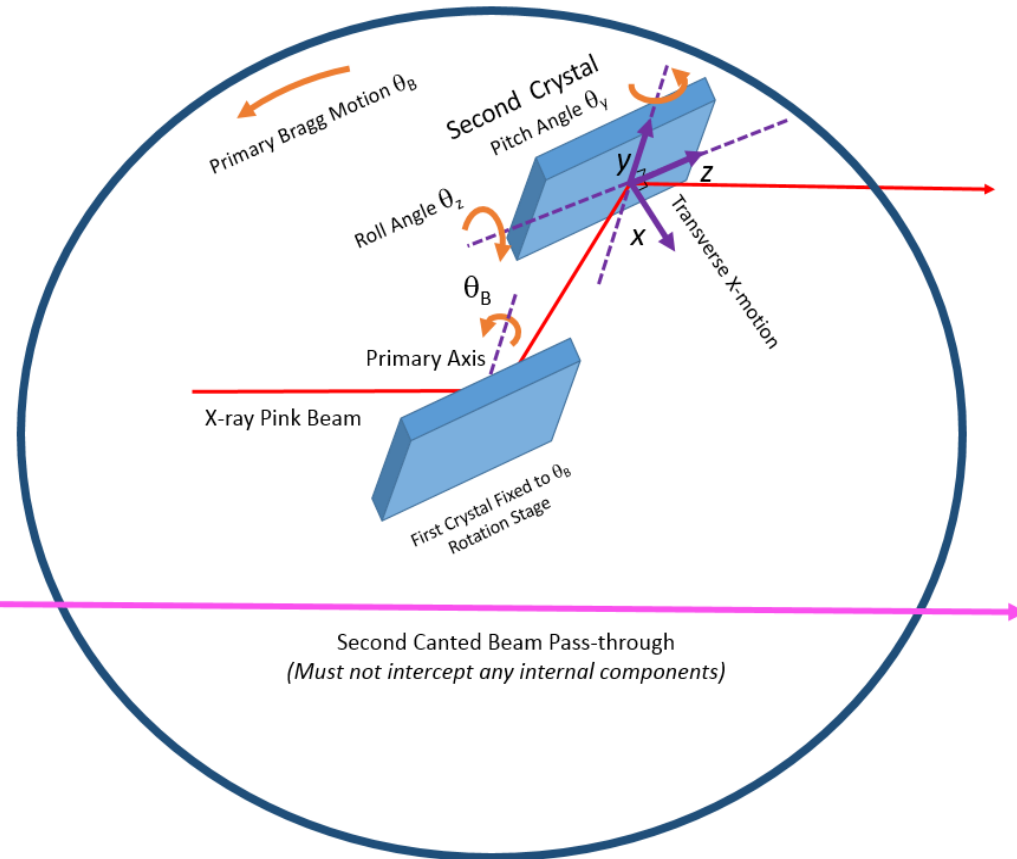
Polarization Effect on Crystal Reflectivity



Reflection	d [Å]	Energy Min [keV]	$\mathcal{R}_2(@10\text{keV})$
111	3.1356	2.80	0.91
220	1.9202	4.57	0.77
311	1.6375	5.35	0.66
400	1.3578	6.46	0.53
333	1.0452	8.39	0.18

Schematic representation of the crystal motions for the HDCM

- 5-30 keV Range
- 15-mm Fixed Offset
- θ_B Rotation
- X_T Translation
- First crystal fixed
- All motions on second crystal
- Second Crystal
 - X_{T2} Motion
 - θ_y Motion (Coarse & Fine)
 - θ_z Motion (Coarse & Fine)
- Piezo-drive fine motion capable of fast feedback
- Capacitive Sensors



HDCM Specifications

Parameters	Value
Energy Range Si [111]	5-30 keV
Fixed horizontal offset between incoming and outgoing beam	15.0 mm
Main Bragg Rotation [q_B]	
Range	-5° to 25°
Resolution*	$0.2 \mu\text{rad}$
Repeatability	$< 0.1 \mu\text{rad}$
Speed	1°s^{-1}
Angular Encoder Resolution	$< 0.1 \mu\text{rad}$
Overall X-direction Translation [X_T]	
Range	$\pm 4 \text{ mm}$
Resolution*	$5 \mu\text{m}$
Repeatability	$5 \mu\text{m}$
Speed	0.5 mm/s
*Resolution = Minimum Step Size	

HDCM Specifications Continued

Parameters	Value
2nd Crystal Coarse Pitch [θ_y]	
Range	$\pm 0.7^\circ$
Resolution*	0.5 μ rad
Repeatability	0.5 μ rad
2nd Crystal Fine Pitch [θ_y] Piezo Driven	
Range	100 μ rad
Resolution	< 50 nrad
Repeatability	< 1 mrad
2nd Crystal Coarse Roll [θ_z]	
Range	$\pm 1.0^\circ$
Resolution*	1.0 μ rad
Repeatability	0.50 μ rad
2nd Crystal Fine Roll [θ_z] Piezo Driven	
Range	125 μ rad
Resolution	< 50 nrad
Repeatability	< 1 μ rad
2nd Crystal Transverse X-direction [X_{2T}]	
Range	± 3 mm
Resolution*	0.2 μ m
Repeatability	0.2 μ m
*Resolution = Minimum Step Size	

Vibration Mitigation Criteria

Steve Kearney and Deming Shu

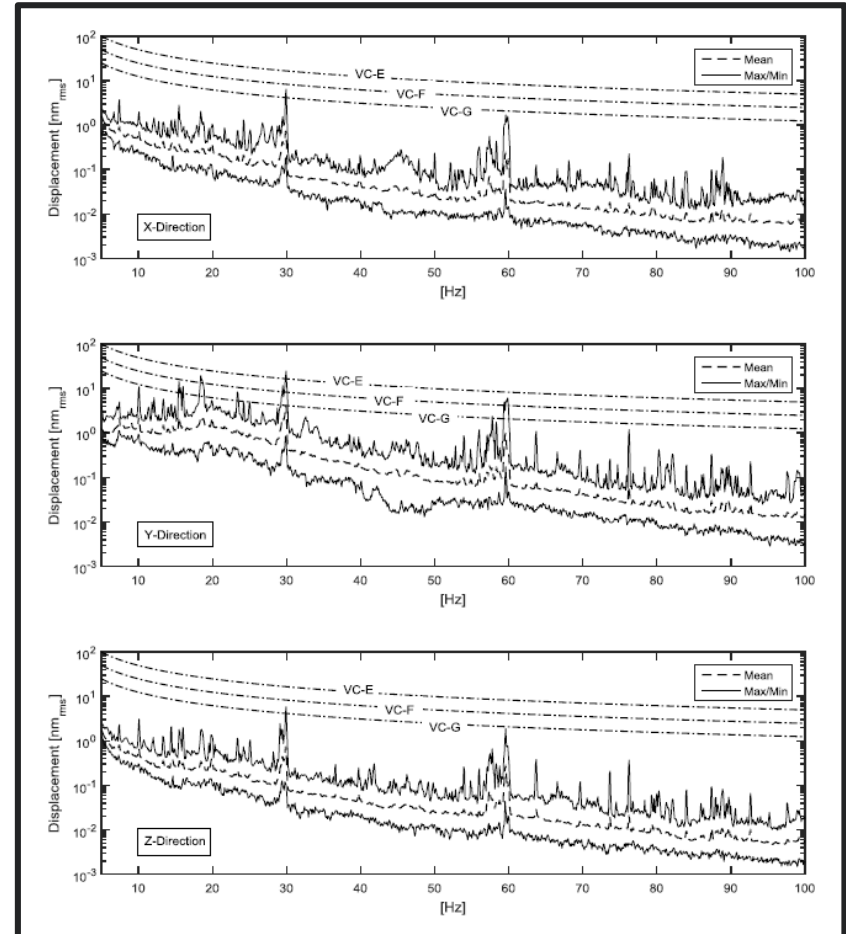
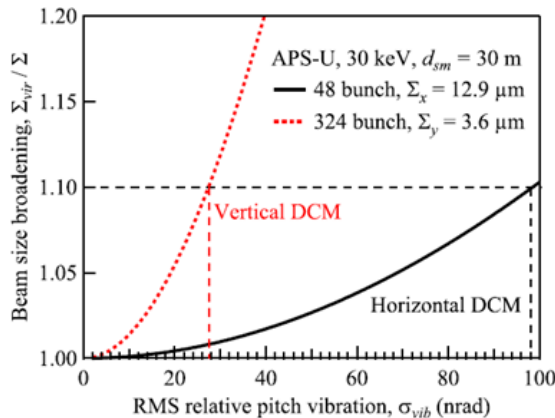
A Survey of Floor Vibration Noise at all Sectors in the APS Experiment Hall

Steven Kearney¹ and Deming Shu¹

¹X-ray Science Division, APS, Argonne National Laboratory, Argonne, IL. 60439

ANL/APS/LS-344

A vibration survey of the APS experiment hall floor was conducted. It was found that beamlines 10-20 have particularly low levels of vibration when compared to the rest of the facility. The vibration spectrum for each beamline floor can be found in the appendix. Throughout the majority of the 5-100 Hz vibration spectrum beamlines at the APS fall below the most stringent NEST vibration criteria. Lastly, it was concluded that the magnitude of vibrations at a particular beamline is largely dependent upon the magnitude of vibrations present at the nearby mezzanine support column.



Lowest Eigen Frequency should be > 100 Hz
Relative pitch Stability <50 nrad

Motion Tolerance and Acceptance Tests

Parameters*	Value
Parasitic Motions	
Parasitic pitch during X_{2T} translation [peak-to-peak]	< 1 μ rad (over 1mm)
Parasitic roll during X_{2T} translation [peak-to-peak]	< 1 μ rad (over 1 mm)
Parallelism of crystals during Bragg rotation [Peak-to-Peak]	< 0.8 μ rad (5-30 deg)
Parasitic pitch and roll during energy change [peak-to-peak]	< 5 μ rad (5-30 keV)
Vibrational Mechanics	
Natural vibration frequency of vessel and support structure	> 100 Hz
Natural vibration frequency of crystal cage	> 100 Hz
Relative pitch stability (1-2500 Hz) [RMS]	< 50 nrad
Relative roll stability (1-2500 Hz) [RMS]	< 50 nrad
*Specifications measured with x-ray beam are done without feedback	

- Parasitic Motions (CONTRACTOR Responsibility with APS Present)
 - Parasitic Pitch and Roll
 - Parallelism of Crystals During Bragg Rotation
 - Parasitic Roll During Energy Change
- Vibrations (CONTRACTOR Responsibility with APS Present)
 - Natural Frequency
 - Crystal Relative Vibrations
- Vacuum Integrity (CONTRACTOR Responsibility with APS Present)
- Motion controls, encoders, piezos, sensors, and cryocooler function (CONTRACTOR Responsibility with APS Present)

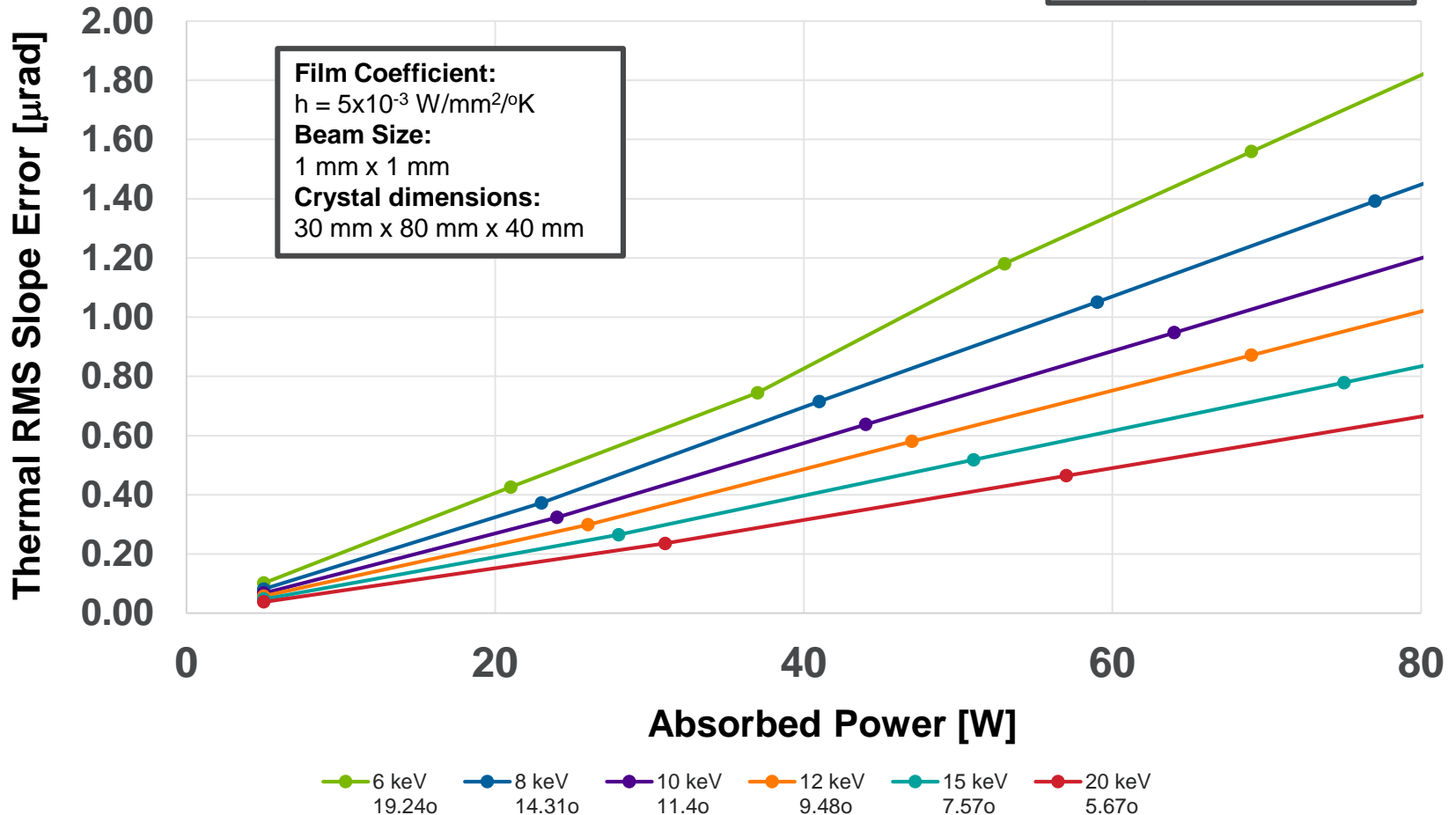
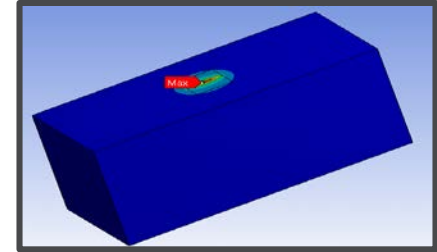
Crystal Specifications

Crystal Parameters	Value
Material	Silicon
Orientation	[111]
Unclamped Darwin width of [333] reflection @ 8 keV	1.9 arc-sec (9.2 μ rad)
Crystal surface roughness	< 30 Å
Unclamped Crystal Flatness [peak-to-peak]	< 30 nm
Clamped Crystal Flatness [peak-to-peak]	< 50 nm
Clamped Sagittal Twist	< 0.2 μ rad/cm
Miss-cut angle	$\pm 0.1^\circ$

- Manufactured by the APS to vendor dimensions
- The crystals will be checked at APS optically for flatness and roughness
- The unmounted crystals will be checked with x-ray diffraction using topography. The Darwin width of the Si [333] reflection at 8 keV shall no more than 10% larger than the theoretical value
- The crystals shall be checked in their mounting fixtures for strain-free mounting with x-ray diffraction using topography

Thermally Induced RMS Slope Error

Indirectly Cooled Silicon Crystal

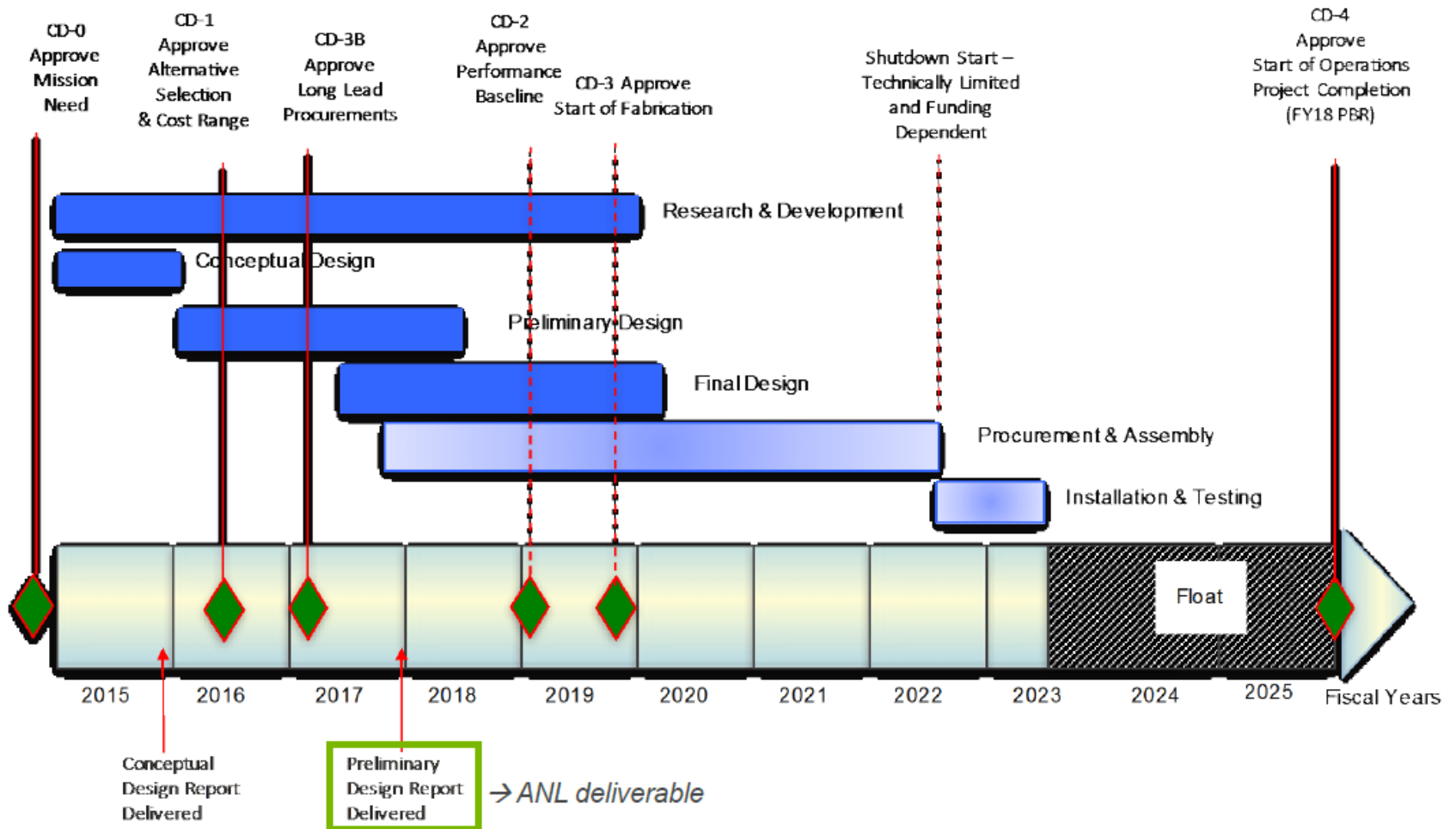


Path to Procurement and Award

- 5/10/17 First Version of RFP Completed
- 6/6/17 Revisions based on input from Working Group completed (ready for APS-U Review)
 - Barry Lai
 - Dana Capatina
 - Mike Fisher
 - Pete Jemian
 - Steve Kearney
 - Xianbo Shi
- 6/26/17 APS-U Review
 - Mark Beno
 - Patricia Fernandez (Chair)
 - Thomas Gog
 - Steve Heald
 - Paul Quinn (Diamond)
 - Deming Shu
- 8/1/17 After Revisions Purchase Approved in Paris
- 8/19/17 RFP to Vendors
- 9/19/17 Proposals from 6 Vendors, Evaluation Begins Based on Best Value Criteria
- 10/18/17 Contract Awarded to IDT

Climbing the Learning Curve will Improve Procurement Cycle

Project Schedule



- Overall schedule funding dependent
- Project utilizing CD-3B authority to adjust to funding fluctuations as appropriate and with full knowledge of BES

Procurement Award to IDT HDCM

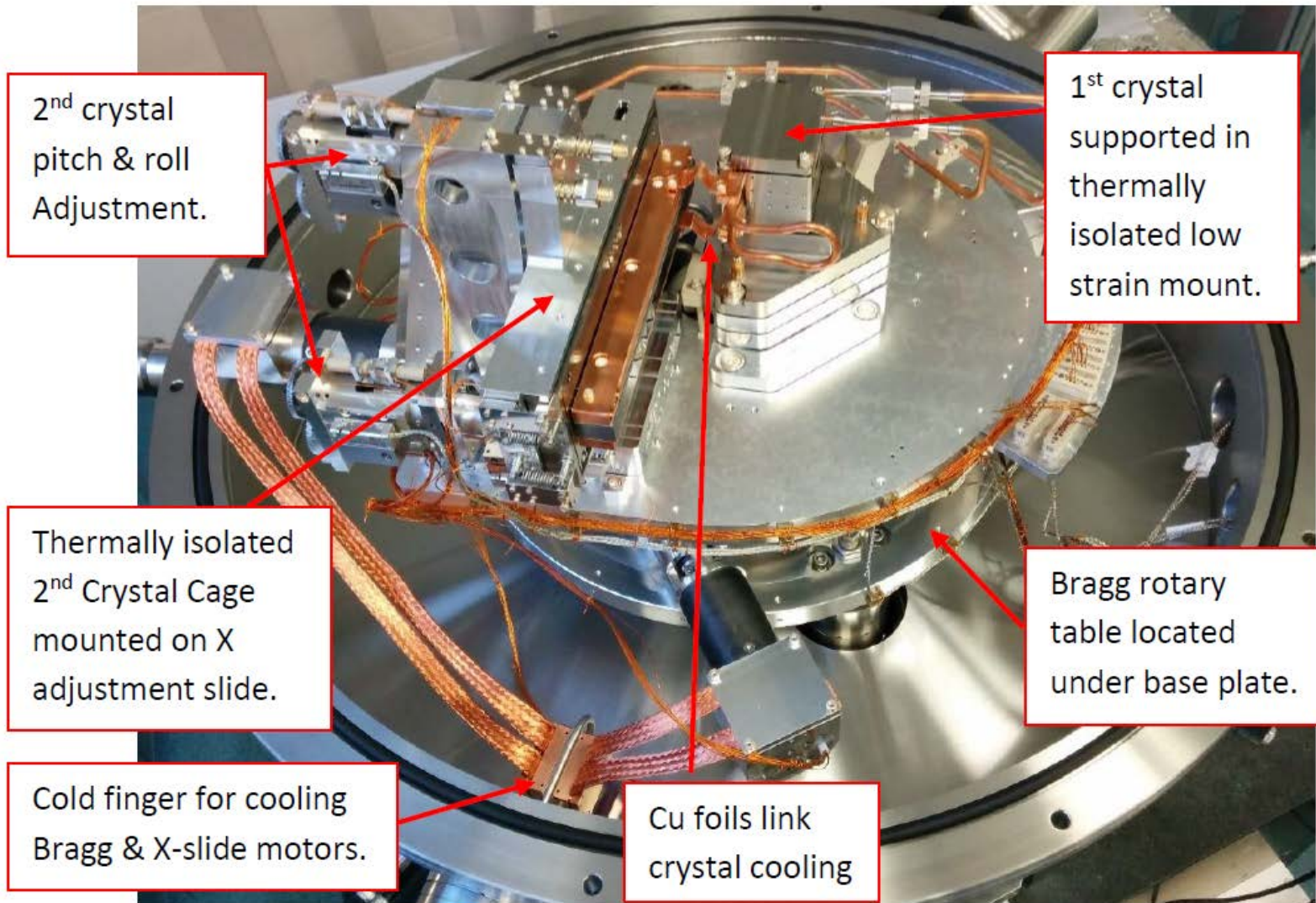
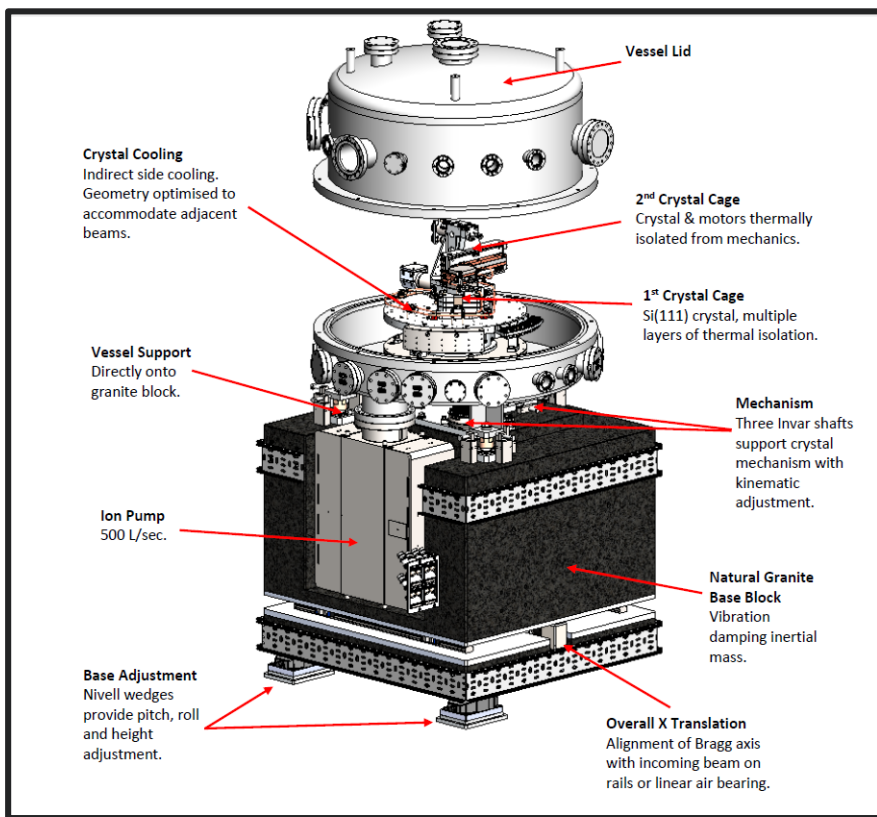
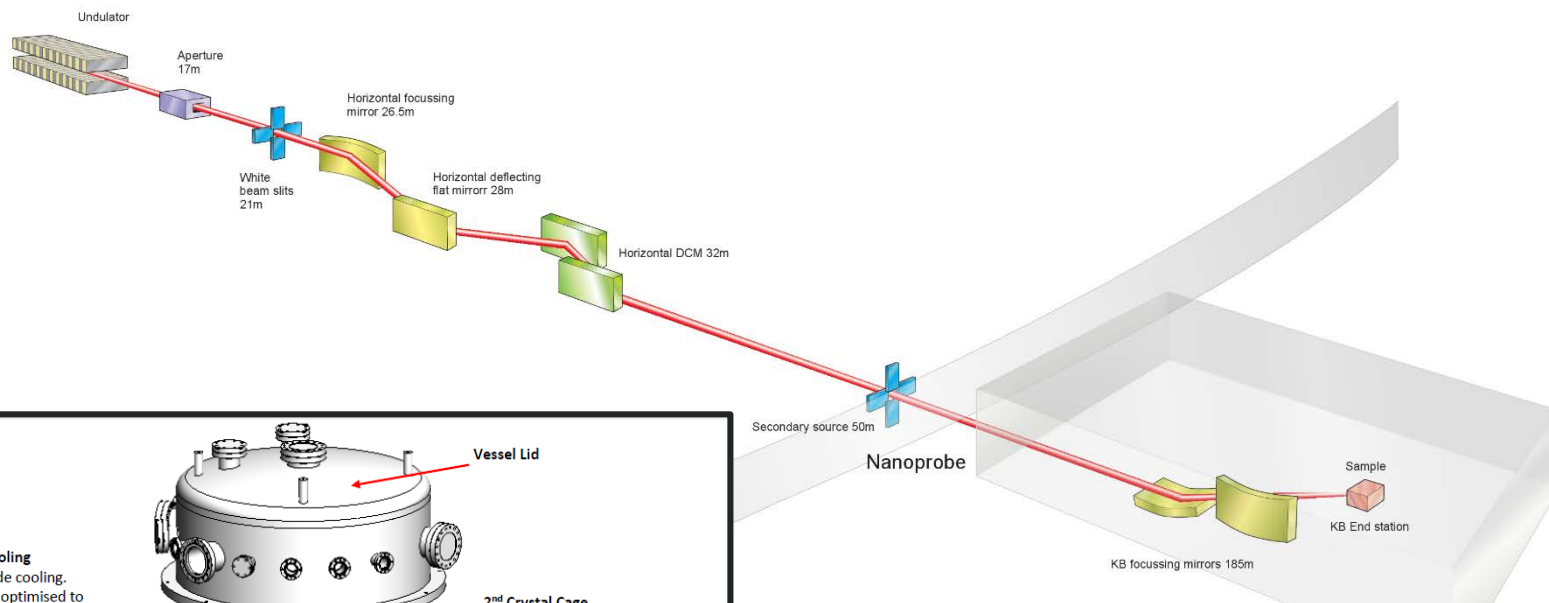


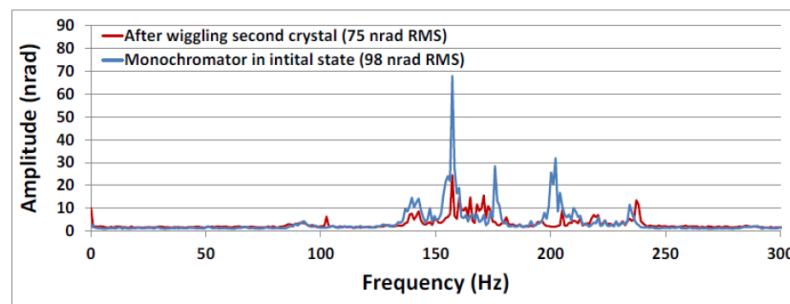
Figure 5: Internal view of mechanism of DCM installed on I14 at DLS.

Diamond I14: Hard X-ray Nanoprobe



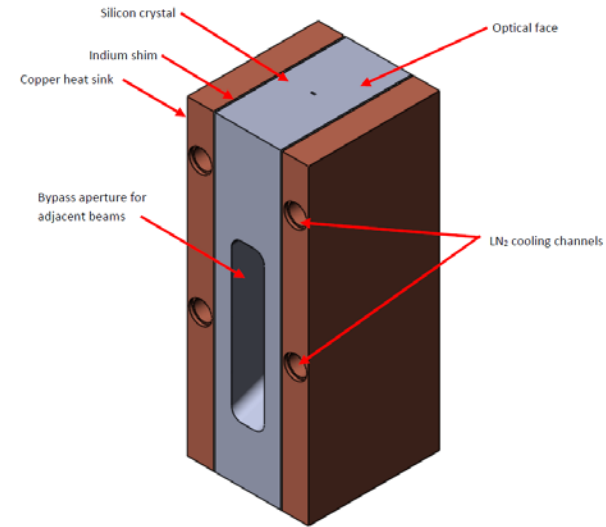
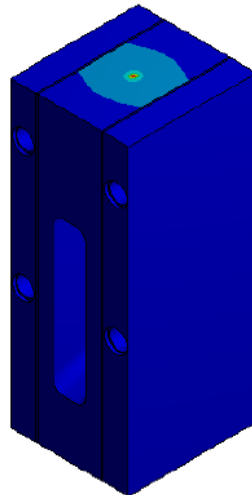
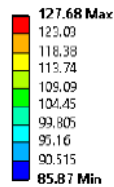
CAP SENSOR DATA

For this test a pair of cap sensors were mounted to the crystal cage assembly. One is mounted from the 1st crystal assembly measuring the distance to the 2nd crystal face, and the other is mounted from the 2nd crystal cage measuring back to the 1st crystal face. The change in distances can be converted to a relative angle. Again, no significant modes were observed below 100 Hz and the first major peak is observed near 160 Hz.

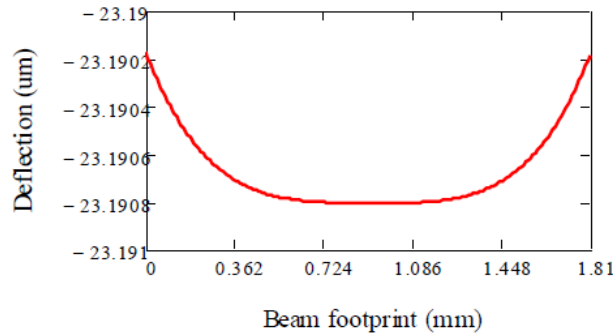


IDT FEA Thermal Analysis

G: Scenario 2, 2 bore
 Temperature
 Type: Temperature
 Unit: K
 Time: 1
 15/09/2017 14:55



Thermal Bend



Thermal Slope

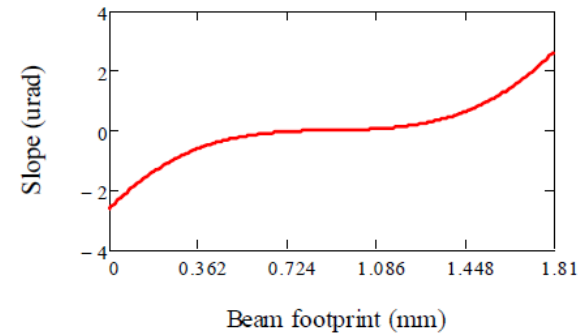


Figure 6: Bypass aperture crystal design, Scenario 2.

Upper left: temperature (K), upper right: stress in crystal (MPa),

middle: temperature (K) in coolant bores,

lower left: thermal bend (μm), lower right: thermal slope (μrad), RMS slope over beam footprint is 1.02 μrad .

Thoughts for the Future APS-U Optics Procurements

- Develop Working Groups that guide the design/specification of standard components such as white-beam mirrors and monochromators
 - APS has developed standard designs in past with the Kohzu monochromator, optical tables,
- Use standardized components as much as possible
- Develop a strategy for acceptance testing of optical components: Mirror, Monochromators, CRLs ...
- Engineering group focused on **FEA** modeling **T**hermal, **M**echanical, and **E**nvironmental effects in monochromators, mirrors, and transfocators
- Feedback information to vendors in a collaborative fashion

Monochromator Working Group

Monochromator based R&D on a generic set of beamline requirements to be carried out at 28-ID.

- Optimization and characterization of crystal cooling geometry.
 - Develop standard crystal mount
 - Determination of operating parameters through FEA calculations and measurement
 - Thermal deformation of the first crystal leads to an additional focusing element
- Thermo-mechanical
 - Eliminate drifts in the monochromator from thermal loading due to Compton scattering that changes based on crystal position
 - Optimization of Compton shielding
 - Possibility of using heaters to stabilize temperature
- Vibration mitigation
 - Study sources of vibration (e.g. experimental floor and LN₂ cooling related)
 - Determine natural frequencies in the monochromator through measurement and FEA calculation
- Maintaining crystal parallelism and positioning
 - In-situ metrology
 - Real-time feedback
 - Fast position compensation
- On-site acceptance testing methods and criteria

Mirror Working Group

Specify a standard mirror systems for white and monochromatic beams based on a generic set of beamline requirements and R&D to be carried out at 28-ID.

- White-beam mirror optimization and characterization of cooling geometry.
 - Develop standard cooling geometry (e.g. side-cooled, internal cooling, ...)
 - Determination of operating parameters
 - Study thermal deformation of the mirror surface leading to figure error
 - FEA simulations of under-cut mirror substrate to mitigate thermal deformation of reflecting surface
- Mechanical bender, adaptive optics, or fixed figure
 - Identify appropriate focusing mechanisms
 - High demagnification will require fixed figure or adaptive optics
- Vibration mitigation
 - Experimental floor frequencies
 - Measure natural frequencies in the granite support structure
 - FEA modeling of support structure
- Mirror angle and surface
 - In-situ metrology
 - Real-time feedback
 - Fast position compensation
- On-site acceptance testing methods and criteria

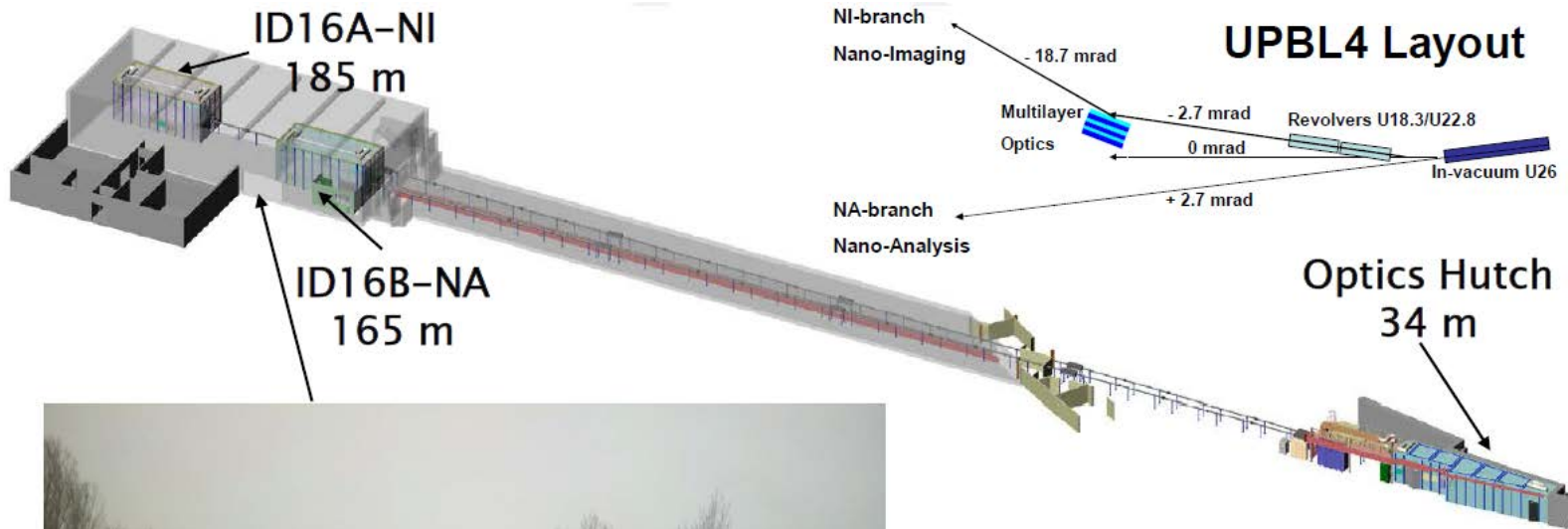
Thermal Stability and Vibration Mitigation Working Group

Develop criteria and methods to create a thermally stable environment in the experimental stations required for sample and beam stability at the nanometer level.

Issues to address:

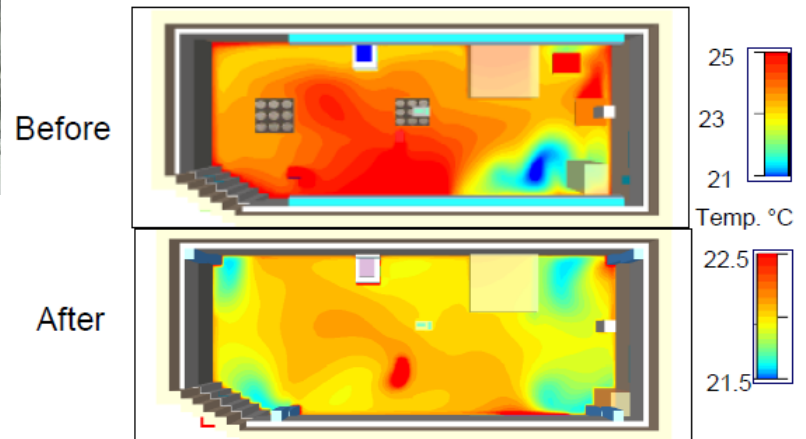
- Use 28-ID experimental station as a test bed.
- Determine stable operating points (e.g. temperature drift ± 0.05 °C with acceptable vibration power spectrum)
- FEA simulation of experimental station to simulate temperature fluctuations, air currents, vibration sources, and their effects on experimental apparatus
 - Requires multiple temperature, air speed, accelerometer sensors for model calibration
 - Determine optimum placement of air ducts to reduce instability caused by air speed fluctuations
 - Determine spectrum and sources of seismic (ground) and acoustic (air) vibration and their effect on experimental apparatus
 - Develop mitigation strategies.
- Develop multiple layers of thermal protection
 - Personnel protocols
 - Thermal barriers such as curtains
 - Phase-change insulation such as Energain by DuPont to reduce day/night variations
 - Standardized insulation for stations
- Extend stabilizing technology being developed for the storage ring to beamlines (FOE as well as the experimental station)

Thermal Stability of Nanoprobe Beamline



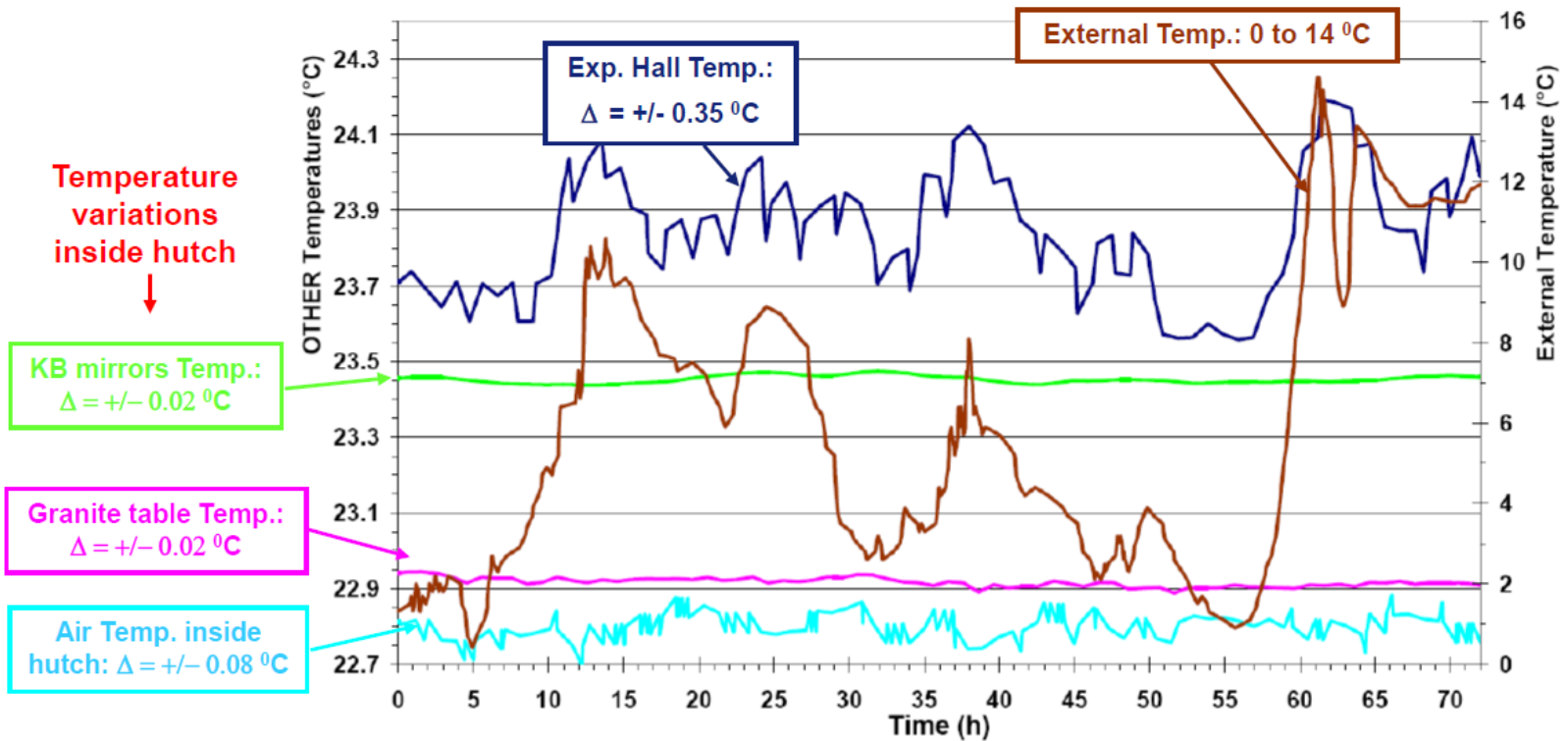
- Hired an outside contractor to develop an FEA model of the hutch
- Air speed variations and temperature fluctuations

Modelled temperature profile in hutch: *courtesy R. Baker*



Spatial gradient improved from degrees to tenths of a degree

Temperature stability recorded over 72 hours

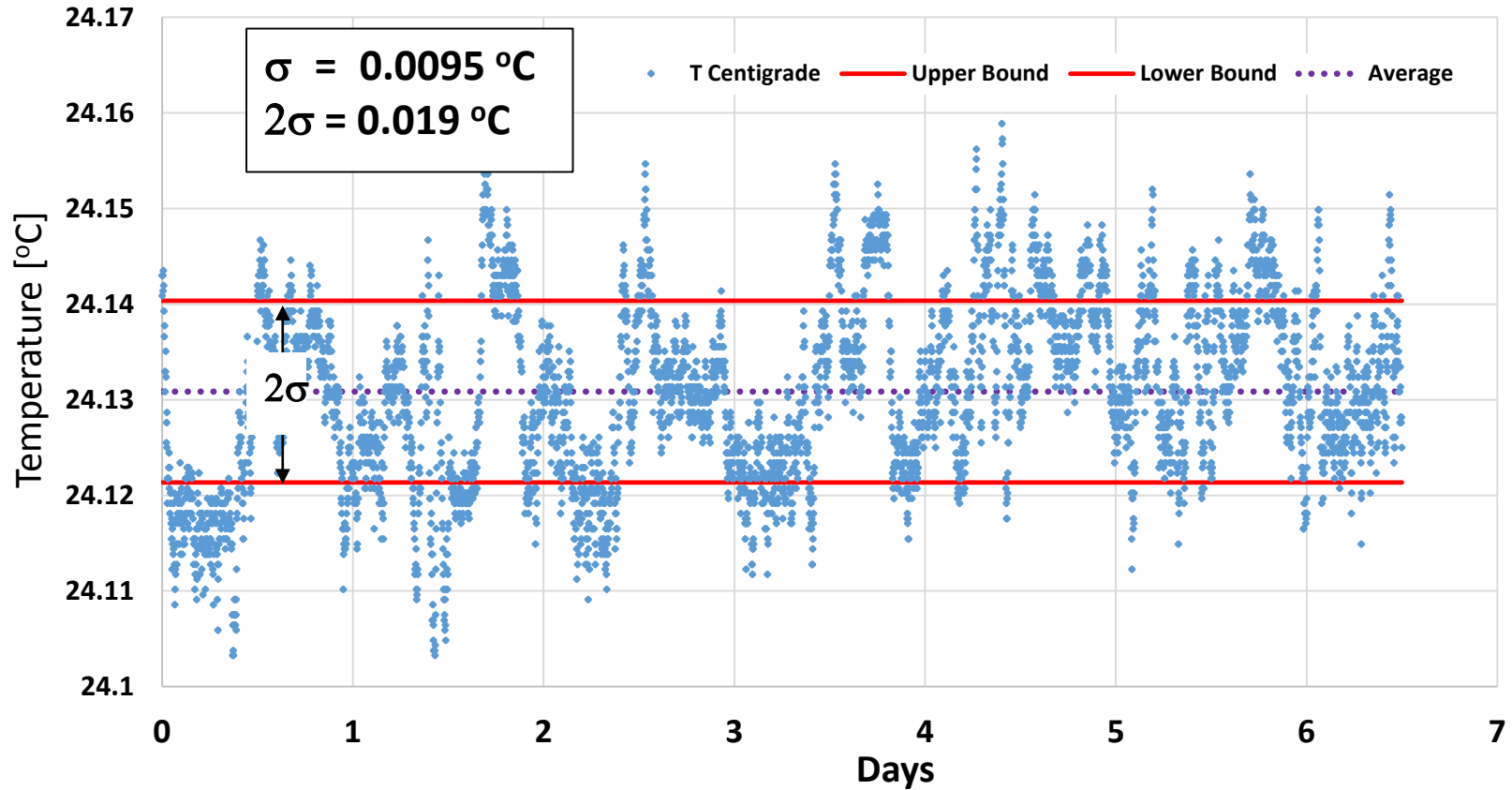


Courtesy R. Baker

Storage Ring Temperature Stability Project

Lester Erwin

Storage Ring Tunnel Temperature for S19



$\sigma = 0.017 \text{ }^\circ\text{F}$
 $2\sigma = 0.034 \text{ }^\circ\text{F}$

Efficiency of Horizontal Monochromators for APS-U Beamlines

Timothy Graber

Advanced Photon Source Upgrade, APS, Argonne National Laboratory,
Argonne, IL 60439

ANL/APS/LS-347

A study of the reduction of reflected x-ray intensity as a function of photon energy for a horizontally deflecting double-crystal monochromator used with a horizontally polarized undulator is described. Integrated Darwin reflectivity curves for silicon crystals and their ratio are presented for both σ and π polarizations. The most common crystallographic orientations [111], [220], [311], [400], and [333] are considered.

1 Introduction

The APS-U is planning a major upgrade to the APS storage ring that will significantly increase x-ray brilliance more than two orders of magnitude by reducing machine emittance from 3.1 nm-rad to 41 pm-rad. This is accomplished by replacing the current double-bend achromat lattice with a multi-bend achromat (MBA) lattice. The ultra-low MBA emittance leads to a reduction in the electron-beam source size and divergence and thereby produces significantly more coherent x-ray flux. For example, the coherent fraction for the MBA lattice will be $\sim 11.6\%$ at 8 keV for a 4.8 m long undulator compared to 0.08% for the present lattice. Furthermore, a reduction in the horizontal source size by a factor of ~ 20 will lead to smaller focal spot sizes and an increase in focused x-ray flux density. To take maximum advantage of these cutting-edge source properties, the APS-U is planning the construction of eight new featured beamlines along with many enhancements to existing beamlines.

Table 1 The electron source properties at the center of the straight section for the present-day APS lattice and for the 41 pm-rad MBA lattice are given. Note that two couplings are possible for 324-bunch mode. They are a high-brightness mode with 10% coupling and a standard mode with 99% coupling.

Parameter	Present Lattice	MBA 324	MBA 324	MBA 48
κ	0.01	0.10	0.99	0.99
σ_x [μm]	275	14.5	12.1	12.7
σ_x' [μrad]	11	2.9	2.4	2.5
σ_y [μm]	10	2.8	7.4	7.6
σ_y' [μrad]	3.5	1.5	3.9	4.1

Table 1 lists the RMS electron-beam source size and divergence at the center of the straight section for the present storage ring lattice and the MBA in 324 and 48 bunch modes. These new source properties along with continued improvements to the figure error of x-ray optics will enable focal spot sizes as small as 10 nm.

For these beamlines, vibration and source motion become critical considerations in the overall equation for final focal-spot size. For example, the minimum specifications for MBA storage-ring AC-RMS motions (0.01- 1 kHz) of the electron-beam position and trajectory angle are specified to be 1/10 of the source properties listed in Table 1. For 324-bunch mode with 10% coupling they are 1.45 μm and 0.29 μrad horizontally and 0.28 μm and 0.15 μrad for vertically¹. The maximum allowed vibration or figure error of an optical component should be smaller than these minimum machine specifications such that the convolution of errors is dominated by the machine specifications.

To reduce the effect of vibration caused by double crystal monochromators (DCM), many facilities are replacing vertically deflecting DCMs with horizontally deflecting models. This geometry has the advantage of not having to cantilever several motion-control stages in the vertical direction and in so doing reduce the possibility of floor vibrations or liquid-nitrogen turbulence exciting low-frequency eigen modes in the monochromator. Additionally, depending on the bunch mode and machine coupling, the horizontal electron-beam source size is 2 to 5 times larger than the vertical source size (see Table 1). Therefore, with a horizontally deflecting DCM, the final beamline focal-spot size will be less sensitive to source motion or monochromator vibration.

A possible drawback of employing horizontally deflecting monochromators at synchrotron radiation sources, where standard undulators produce an electric-field polarization almost entirely in the orbit plane, is the reduction of the Darwin-curve width (and therefore reflected intensity) as a function of Bragg angle. The reduction in reflected intensity when the electric field vector is in the plane of incidence (π -polarization) is due to destructive interference between the incoming and outgoing electric fields as the Bragg angle approaches 45°. This APS Light Source Note documents this effect for horizontally deflecting DCMs.

2 Calculation

Darwin Width and Energy Bandpass

The equation for the width of the Darwin curve^{2, 3} is given by Eq. 1,

$$\omega_i = \frac{2}{\sin 2\theta_B} \frac{r_e \lambda^2}{\pi V} C_i |F| e^{-M} \quad (1)$$

where θ_B is the Bragg angle, r_e is the classical electron radius, λ is the wavelength of the radiation, C_i is the polarization factor and is 1 for σ -polarization (vertically deflecting) and $|\cos 2\theta|$ for π -polarization (horizontally deflecting), $|F|$ is the magnitude of the crystal structure factor, V is the unit-cell volume, and e^{-M} is the Debye-Waller factor. If the dispersion correction ($f' + if''$) is included, the crystal structure factor F is complex. The Darwin width is the angular interval for which the reflectivity is unity in the case of zero absorption. It is related to the FWHM by $\omega_{FWHM} = \frac{3}{2\sqrt{2}} \omega_D = 1.061 \omega_D$.

For the APS-U running in 324-bunch mode with 99% coupling, the RMS electron-beam divergences are $\sigma'_x = 2.4 \mu\text{rad}$ for the horizontal and $\sigma'_y = 3.9 \mu\text{rad}$ for the vertical. The RMS photon-beam divergence (Σ'_x, Σ'_y) for $i = x, y$ is given by⁴

$$\Sigma'_i = \sqrt{\sigma_i'^2 + \frac{\lambda}{2L}} \quad (2)$$

where λ is the wavelength of the radiation and $L = 2.4 \text{ m}$ is the length of a standard planar undulator.

Figure 1 shows the Darwin widths for horizontal and vertical polarization (ω_h, ω_v) plotted (left axis) along with the photon-beam divergences (Σ'_x, Σ'_y) multiplied by 2.35 to convert to FWHM values. The energy bandpass is plotted according to the right axis, which is indicated by an arrow in Panel (a). Three cases are presented in Fig. 1. Panel (a) shows the [111] reflection of silicon, (b) [220], and (c) [311]. The energy bandpass of a DCM is approximated by multiplying the width of the convolution of the Darwin curve and the photon-beam angular distribution by $\cot \theta_B$ and the monochromator energy E . The energy bandpass ΔE is given by Eq. (3)

$$\Delta E = E \sqrt{\Omega_i^2 + \omega_i^2} \cot \theta_B \quad (3)$$

where $\Omega_i = 2.35 \Sigma'_i$. Panel (a) Fig. 1 shows the case where the Darwin width is greater than the beam divergence and the energy bandpass is dominated by the Darwin width. Panel (b), the [220] case, the Darwin width and the beam divergence contribute equally to ΔE . For the [311] case in Panel (c), the beam-divergence begins to dominate the

convoluted width and therefore ΔE . Since $\sigma'_x < \sigma'_y$ for the MBA with 99% coupling, the energy bandpass actually improves slightly for the horizontal geometry. This is not true for 10% coupling where $\sigma'_x = 2.9 \mu\text{rad}$ for the horizontal and $\sigma'_y = 1.5 \mu\text{rad}$.

Integrated Reflectivity

To calculate the reduction in reflected intensity due to x-ray polarization as function of energy the Darwin curve is integrated for the both horizontal and vertical cases and a ratio is taken. The integrated reflectivity for zero absorption (neglecting the dispersion correction) can be calculated in closed form and is given by²

$$I_i = \int_{-\infty}^{\infty} R(\theta - \theta_B) d\theta = \frac{8}{3 \sin 2\theta_B} \frac{r_e \lambda^2}{\pi V} C_i |F| e^{-M} \quad (4)$$

The ratio of the horizontal to the vertical intensity $\mathcal{R}_o(E)$ for the case of zero absorption is given simply by

$$\mathcal{R}_o(E) = \frac{I_h}{I_v} = \frac{\omega_h}{\omega_v} = |\cos 2\theta_B| \quad (5)$$

where E is given by Bragg's law $E = \frac{hc}{2d \sin \theta_B}$. For the case of zero absorption, the ratio $\mathcal{R}_o(E)$ is proportional to the ratio of the Darwin widths. Note that the factor C_h for horizontal polarization is $|\cos 2\theta|$ for dynamic diffraction rather than $|\cos 2\theta|^2$ which is true for kinematic diffraction^{2,3}.

In this simple model, several effects that could affect the intensity of the beam have been neglected. They are (1) absorption in the crystal, (2) the fact that there are two crystals reflecting in a typical DCM, and (3) the difference between the horizontal and vertical divergence of the x-ray beam incident on the monochromator. For the last effect (3), we note that the monochromator we are considering is assumed to have its crystals arranged in a nondispersive (+n,-n) geometry. In this geometry, the divergence properties of the x-ray beam are not changed by the monochromator and differing horizontal and vertical photon-beam divergences mainly affect the energy bandpass of the monochromator as shown in Fig. 1.

In the case where photon absorption is included (1), the crystal structure factor is calculated using both the real and imaginary parts of the dispersion correction. Figure 2 shows the Silicon [111] Darwin reflectivity curves, with absorption included, for a vertically diffracting crystal (red) and a horizontally diffracting crystal (blue) with the electric field polarization in the horizontal direction. Three energies (a) 20, (b) 4, and (c) 3 keV are shown. Note that the energy for a Bragg angle of 45° is 2.8 keV for Si [111]. For horizontal polarization, the reflectivity curve is reduced in both peak reflectivity as well as width and the shape of the Darwin curve becomes more Gaussian as the Bragg angle approaches 45° . The reduction in total reflectivity for a horizontally deflecting single

crystal as a function of energy is given by the ratio of the integrated horizontal reflectivity divided by the integrated vertical reflectivity (Eq. 4).

$$\mathcal{R}_1(E) = \frac{\int_{-\infty}^{\infty} R_h(\theta-\theta_B)d\theta}{\int_{-\infty}^{\infty} R_v(\theta-\theta_B)d\theta} \quad (6)$$

Figure 3 shows the reflectivity ratio $\mathcal{R}_1(E)$ as a function of energy for Silicon [111] for three cases. The red curve is a plot of $|\cos 2\theta|$ which is $\mathcal{R}_0(E)$ in the case of zero crystal absorption. The blue curve shows the reflectivity ratio for a single crystal with absorption taken into account (Eq. 6). For case (2), where two crystals are present in a nondispersive (+n,-n) geometry, the total reflected intensity is proportional to the product of the Darwin curves for each crystal. The green curve in Fig. 3 is a plot of the square of the single-crystal reflectivity integrated over angle and is appropriate for two consecutive reflections in a DCM arranged in a nondispersive geometry. The DCM reflectivity ratio is given by Eq. 7.

$$\mathcal{R}_2(E) = \frac{\int_{-\infty}^{\infty} R_h^2(\theta-\theta_B)d\theta}{\int_{-\infty}^{\infty} R_v^2(\theta-\theta_B)d\theta} \quad (7)$$

Figure 3 clearly shows that, absorption has the effect of extending the energy region of near-zero ratio around the 45° Bragg energy. Two consecutive reflections further broaden the minimum and reduce the DCM reflectivity $\mathcal{R}_2(E)$ by as much as 25% around the minimum when compared to the simple $|\cos(2\theta)|$ model for zero absorption.

Figure 4 shows the integrated reflectivity (I_v and I_h) as a function of energy with vertical orientation (σ -polarization) and horizontal orientation (π -polarization) for the most commonly used DCM reflections of Silicon: [111], [220], [311], [400], and [333]. The vertical orientation is shown as a dashed line. Figure 5 shows the DCM reflectivity ratio, $\mathcal{R}_2(E)$, for the same reflections. The energy of the minima and the reflectivity ratio $\mathcal{R}_2(E)$ at 10 keV for the curves in Fig. 5 are given in Table 2 as a function of reflection.

Table 2 List of the energy minima and the reflectivity ratio @10 keV for the curves in Fig. 5.

Reflection	d [Å]	Energy Min [keV]	$\mathcal{R}_2(@10\text{keV})$
111	3.1356	2.80	0.91
220	1.9202	4.57	0.77
311	1.6375	5.35	0.66
400	1.3578	6.46	0.53
333	1.0452	8.39	0.18

3 Conclusion

For beamlines using a standard planar undulator with the electric field polarization predominately in the horizontal plane, the reflected intensity for a horizontally deflecting Si [111] DCM at 6 keV is approximately 70% of the intensity of a vertically deflecting

monochromator (Fig. 5). For energies above 10 keV, the intensity loss is < 10% of a vertically deflecting DCM. If higher order reflections are required, the intensity loss becomes more significant. For these reflections, the decision to use a horizontally deflecting monochromator should be considered on a case-by-case basis. Additionally, when a higher order reflection and high stability are required, a vertically polarized undulator should be considered

4 Acknowledgments

I thank Dean Haeffner, Ruben Reininger, Xianbo Shi, and Tom Toellner for suggestions and comments that greatly improved the manuscript. Work supported by the U.S. Department of Energy, Office of Science, under Contract No. DE-AC02-06CH11357.

5 References

- [1] Nick Sereno, Beam Stability R&D for the APS MBA Upgrade, 2015 Libera Workshop.
- [2] Tadashi Matsushita and Hiro-O Hashizume, X-ray Monochromators, Handbook on Synchrotron Radiation Vol v1, edited E. Koch, (1983) 261.
- [3] Jens Als-Nielsen and Des McMorrow, Elements of Modern X-ray Physics, John Wiley & Sons, 2011.
- [4] Gianluca Geloni, Vitali Kocharyan, and Evgeni Saldin, J. Synchrotron Rad., **22**, 288–316, 2015.

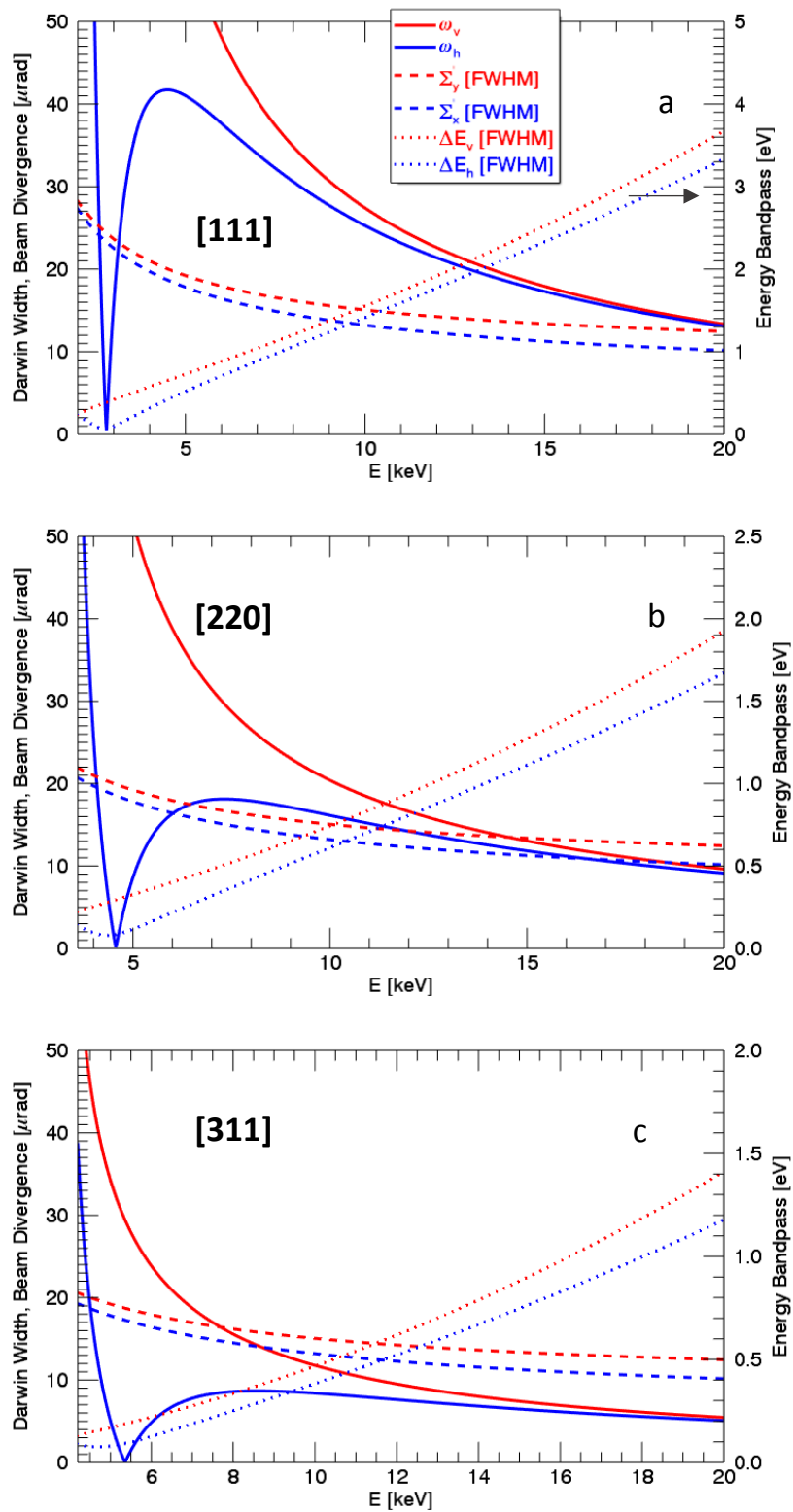


Figure 1 The Darwin width is plotted along with the horizontal and vertical x-ray beam divergences for APS-U source conditions on the left axis. The energy band-pass is plotted according to the right axis. Panel (a) Silicon [111], (b) [220], and (c) [311].

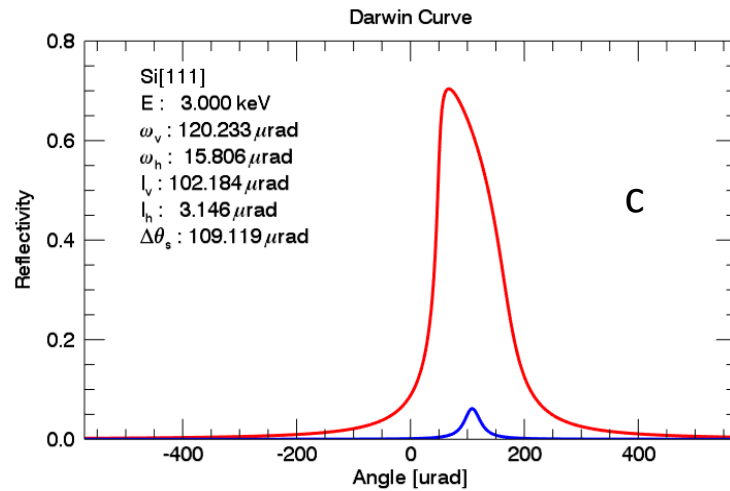
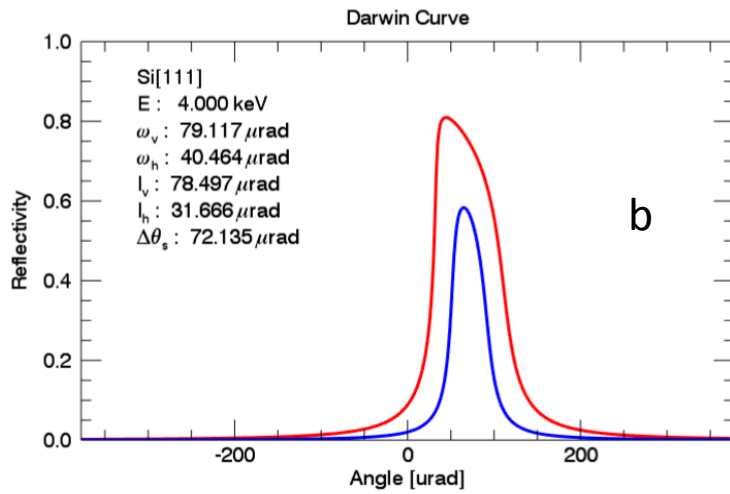
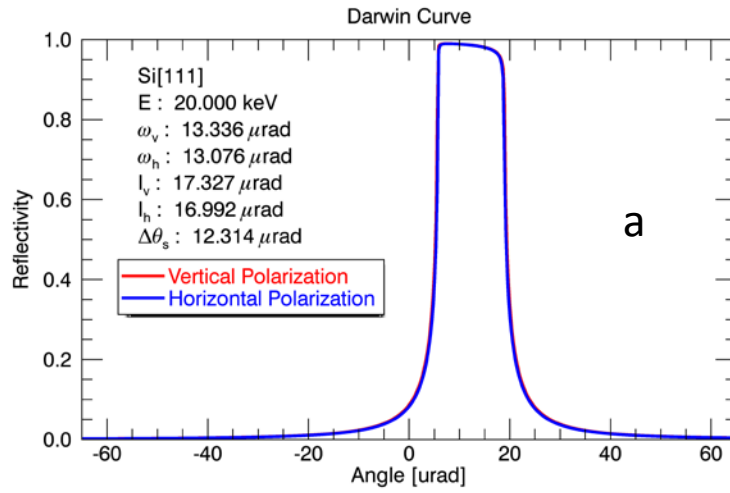


Figure 2 The Darwin curves are shown for the Silicon [111] reflection for vertical (red) and horizontal (blue) polarizations at 20, 4, and 3 keV. The Bragg angles are 5.7°, 29.6°, and 41.2°, respectively. Due to refraction, the centroid of the curve is offset from the origin by $\Delta\theta_s$.

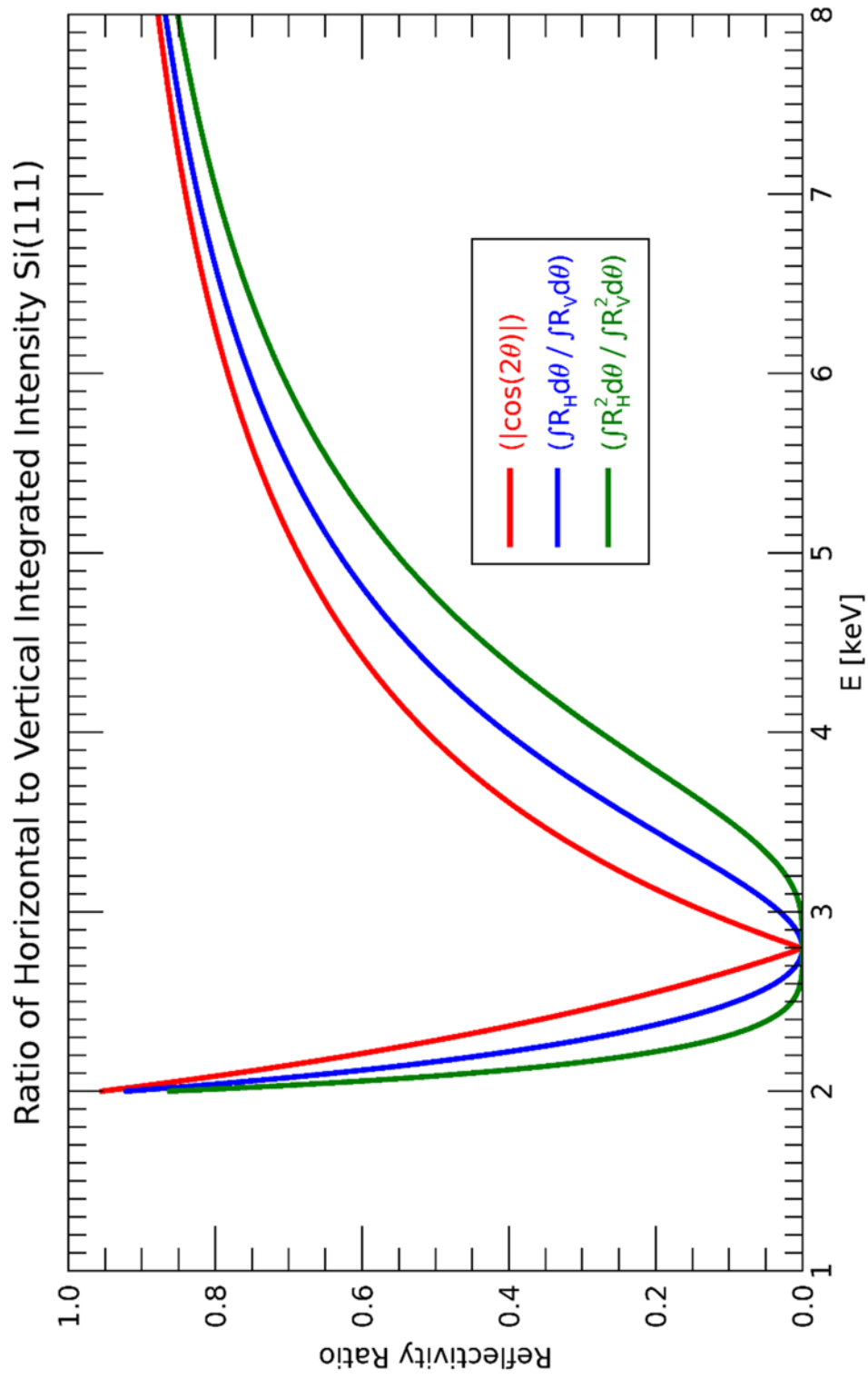


Figure 3 The ratio of the integrated reflectivity is shown as a function of energy for the Silicon [111]. The red curve is $|\cos(2\theta)|$ plotted against energy in keV. The blue curve is the integrated reflectivity of a single reflection and the green curve represents a reflection from two crystals in a non-dispersive geometry.

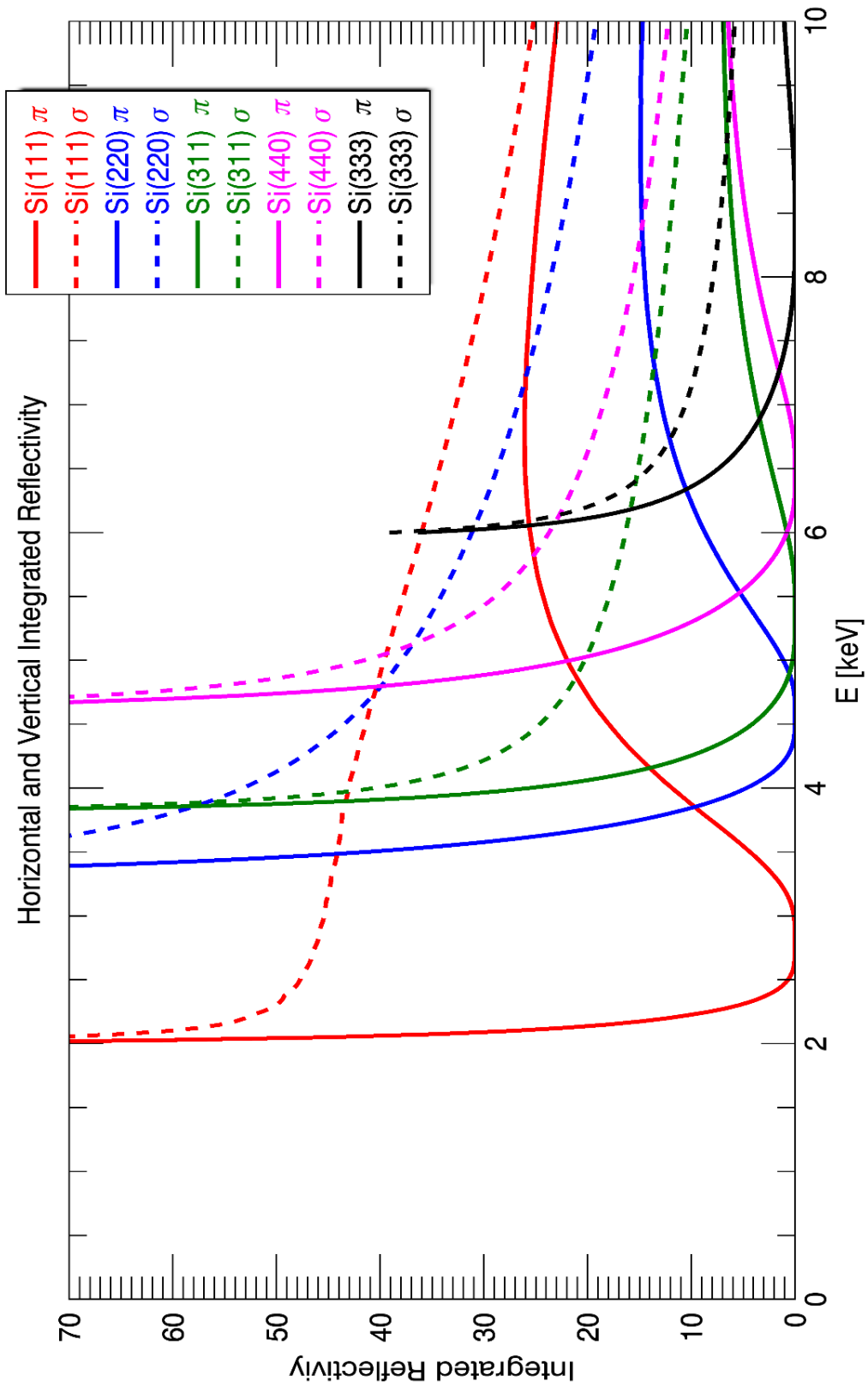


Figure 4 The vertical (dashed) and horizontal (solid) integrated reflectivity is shown as a function of energy for the Silicon [111], [220], [311], [400], and [333] reflections.

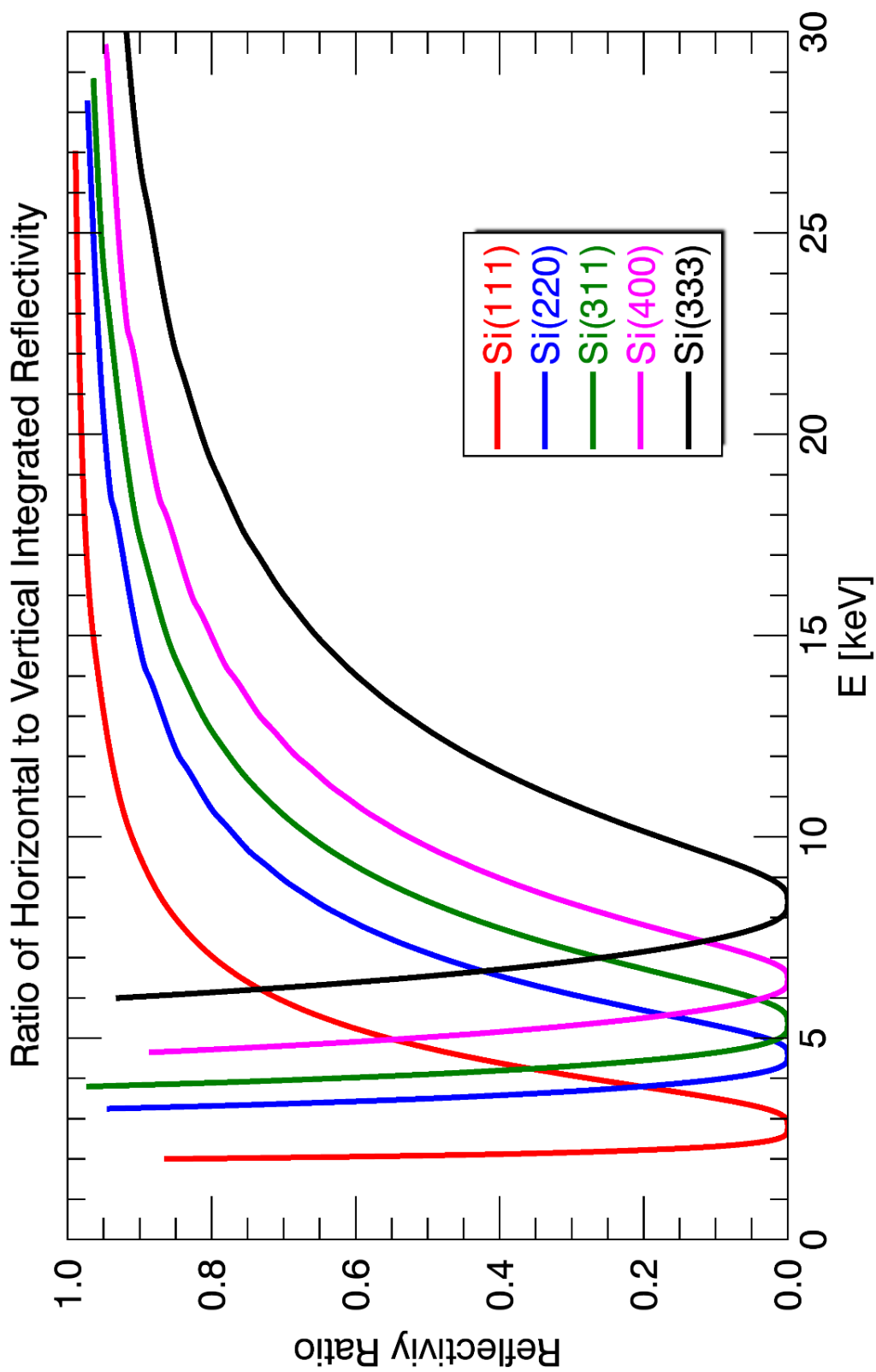


Figure 5 The ratio of the integrated reflectivity for a double crystal monochromator is shown as a function of energy for the Silicon reflections [111], [220], [311], [400], and [333].

A Survey of Floor Vibration Noise at all Sectors in the APS Experiment Hall

Steven Kearney¹ and Deming Shu¹

¹X-ray Science Division, APS, Argonne National Laboratory, Argonne, IL. 60439

ANL/APS/LS-344

A vibration survey of the APS experiment hall floor was conducted. It was found that beamlines 10-20 have particularly low levels of vibration when compared to the rest of the facility. The vibration spectrum for each beamline floor can be found in the appendix. Throughout the majority of the 5-100 Hz vibration spectrum beamlines at the APS fall below the most stringent NEST vibration criteria. Lastly, it was concluded that the magnitude of vibrations at a particular beamline is largely dependent upon the magnitude of vibrations present at the nearby mezzanine support column.

1 Introduction

Vibration noise in the experiment hall of the Advanced Photon Source (APS) is a potential primary source of mechanical noise induced into experiments being conducted at the APS. Therefore, understanding the current levels of vibration and locations of particularly low and high vibrations is of utmost importance. In addition, with the planned APS upgrade new beamline construction and/or redesigns of existing beamlines is expected, so it is beneficial to know the current levels of vibration at these locations for planning purposes. This survey was conducted at each beamline of the APS and presents the findings with a brief analysis of potential vibration sources as well as identifying locations of low vibration noise.

2 Procedure

A vibration noise survey was conducted at the Argonne National Laboratory Advanced Photon Source experiment floor. Data was recorded at all beamlines over multiple sessions. For consistency, measurements were only taken the day before the scheduled weekly machine intervention when most users were not running experiments, but with the beam still on. Also, to limit the influence of transient vibrations, data was recorded only after 5 pm or on the weekends. The specific dates of measurement sessions were: 3/28/2016, 4/4/2016, 4/11/2016, 4/18/2016, 4/25/2016, and 6/12/2016. In addition, a separate special case data set was recorded in sector 21 during electrical maintenance (4/30/2016) in which the mechanical air handling unit, DI pumps,

and vacuum pumps, were shut down in sectors 20-23. This data was then used to assess the contribution of these systems to the vibration noise in sector 21. This is just a single sector comparison, but due to the modular similarity of mechanical equipment around the storage ring this can be assumed to represent typical mechanical noise contributions for all beamlines.

To measure the vibration noise, 3 high sensitivity accelerometers were used (VibraMetrics 1030, Mistras Group Inc., Princeton Junction, NJ) for each Cartesian direction, see Table 1. In line with the accelerometers were 3 power supplies for each channel (VibraMetrics P5000, Mistras Group Inc., Princeton Junction, NJ). For data acquisition a Photon+ 4 channel (Brüel & Kjær) signal analyzer was used with RT Pro Version 7.20 dynamic signal analysis software (Brüel & Kjær). The data acquisition settings can be seen in Table 2.

Table 1. Specifications and settings of accelerometers used for each channel recorded. See Figure 1 for specific channel location and coordinate frame.

Channel	Direction	Model No.	Serial No.	Gain	Sensitivity [V/g]
1	X	VibraMetrics 1030	1349	x1	7.088
2	Y	VibraMetrics 1030	1625	x1	7.000
3	Z	VibraMetrics 1030	1493	x1	7.010

Data was acquired separately at all 35 beamlines of the APS. Two measurement points for each beamline were chosen based on similar construction geometry and for the best representation of vibrations for the entire beamline. These two points can be seen in Figure 1. The column floor point is assumed to represent the majority of the noise source to the floor for the nearest beamline. This assumption comes from the fact that the column is a support structure for the mechanical equipment mezzanine floor. There are many more columns than there are beamlines so the column closest to the floor measurement point was chosen, see Table 3 for the specific column measured and which beamline it represents. Similarly, the beamline floor point is assumed to represent the noise present for that entire beamline. Notice that the red dashed line shows many potential measurement points. This is required due to the varying construction designs and surrounding equipment layout of each column and end station.

Table 2. Parameter settings used in the RT Pro 7.2 dynamic signal analysis software for data acquisition.

Parameter	Value	Unit
Sampling Frequency	375	Hz
Number of Samples	4096	
Bandwidth	150	Hz
Frequency Resolution	0.091	Hz
Window	Hanning	
Averages	20	

For analysis, the data is presented in spectral RMS displacement and in mean RMS displacement for individual octave bands. RMS displacement is derived from the raw accelerometer voltage data using

$$U_{rms} = \frac{gV_{rms}}{(\text{gain})(\text{sensitivity})}, \text{ with } g = 9.81 \text{ m/s}^2. \quad (1)$$

The mean RMS displacement from defined frequency bands, adapted from (Rogers et al. 1997), is defined as

$$\bar{U}_k = \frac{1}{N_k} \sum_{i=f_{low}(k)}^{f_{high}(k)} U_{rms}(i), \quad (2)$$

with k defined as the band number, i representing each frequency bin, and N_k the number of bins in band k . In Equation (2) the units are still in RMS displacement with the RMS subscript removed for clarity. Presenting the data in bands rather than full spectral plots allows for a quick and concise comparison of a single value for each beamline. For this study standard octave bands were used and are listed in Table 4 as well as the number of frequency bins used in each band to calculate the mean.

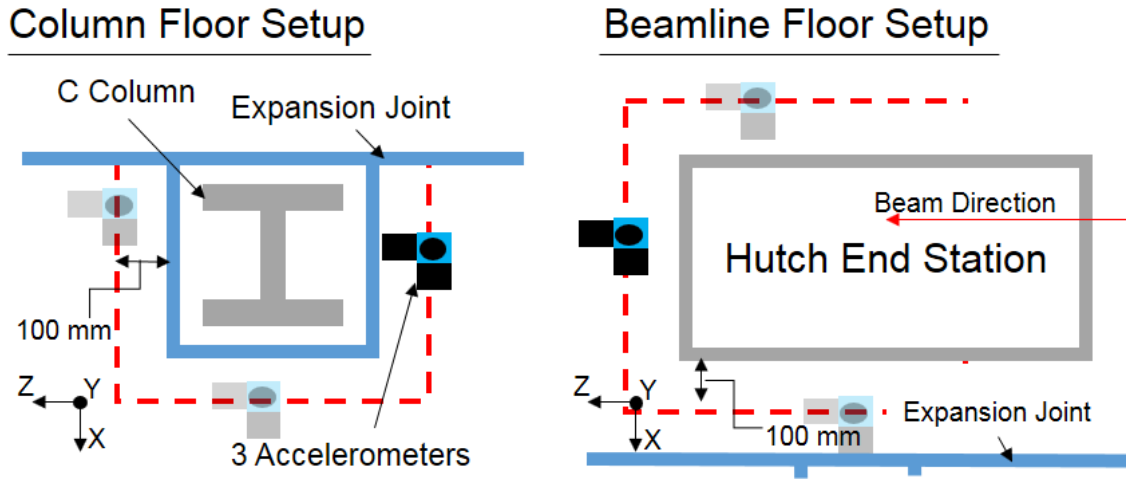


Figure 1. A bird's eye view of the two measurement points used for each beamline (not to scale). On the left is the setup for the column floor measurement point and on the right the beamline floor measurement point. For both, the coordinate frame is shown in the lower left with X away from the storage ring center, Y in the vertical direction, and Z in the beam direction. The hutch end station is located in the -X direction on the opposite side of the expansion joint of the column. The red dashed line represents potential placement locations of the sensor block, with the transparent blocks showing other potential locations, based on accessibility to the floor.

Table 3. Beamlines and the associated nearby column that was measured.

Beamline	Column	Beamline	Column	Beamline	Column
1	C069C	13	C104C	25	C140C
2	C072C	14	C106C	26	C143C
3	C074C	15	C110C	27	C145C
4	C078C	16	C113C	28	C149C
5	C081C	17	C116C	29	C152C
6	C083C	18	C119C	30	C154C
7	C086C	19	C121C	31	C159C
8	C090C	20	C125C	32	C162C
9	C093C	21	C129C	33	C165C
10	C095C	22	C131C	34	C167C
11	C098C	23	C135C	35	C169C
12	C101C	24	C137C		

Table 4. Octave bands used in the comparison of beamlines with upper and lower frequency bounds listed and the number of frequency bins averaged, N_k .

Octave Band k	f_{low} [Hz]	f_{high} [Hz]	N_k
1	2.8	5.5	30
2	5.5	11	62
3	11	22	121
4	22	44	241
5	44	88	482

3 Results and Discussion

3.1 Experiment Hall Floor Vibration Levels

Each beamline was individually measured at two points, the floor next to the nearest column and the beamline floor just outside the end station hutch. Full X, Y, Z spectrums of vibration displacement for each beamline floor can be seen in the Appendix. Every individual beamline floor vibration spectrum (designated by the ID # in the title over each plot) displays the beamline in a bold black line, and, for comparison, the maximum/minimum, and mean of all APS beamline floor vibrations are plotted in solid gray and red dash dot lines, respectively. From these spectrums a trend starts to appear; a trend that beamlines close to each other tend to have similar levels of noise. This trend will be much more clear when we look at band data in the next section.

We can also use the entire set of beamline floor data to see the magnitude of vibrations in the APS experiment hall as a whole. Figure 2, displays the X, Y, Z spectral vibration magnitude range of all the beamlines. Included in this plot are a few of the most stringent standard vibration criteria (VC) created by the Institute of Environmental Sciences and Technology (IEST) (Amick et al. 2005). Each curve is subsequently more sensitive and thus harder to achieve, with VC-E at $3.2 \mu\text{m/s}$, VC-F at $1.56 \mu\text{m/s}$, and VC-G at $0.78 \mu\text{m/s}$. VC-E, is described as “Challenging to achieve ... Assumed to be adequate for the most demanding of sensitive systems.”, with an achievable detail size in microelectronics fabrication of less than 100 nm. As can be seen in Figure 2 almost all of the floor vibrations are below the VC-E curve with the exception being the maximum line at 30 Hz. Even more encouraging is that the majority of vibration magnitudes are below the most stringent VC-G curve with only 5 peaks in the maximum line breaking the VC-G curve at 15 Hz, 18 Hz, 23 Hz, 30 Hz, and 60 Hz. Overall the entire APS experiment hall floor is an extremely quiet facility and a very good starting point to build the most sensitive equipment on. However, there is still room for improvement, particularly in the 10 – 60 Hz band, which will be made more clear in Section 3.3.

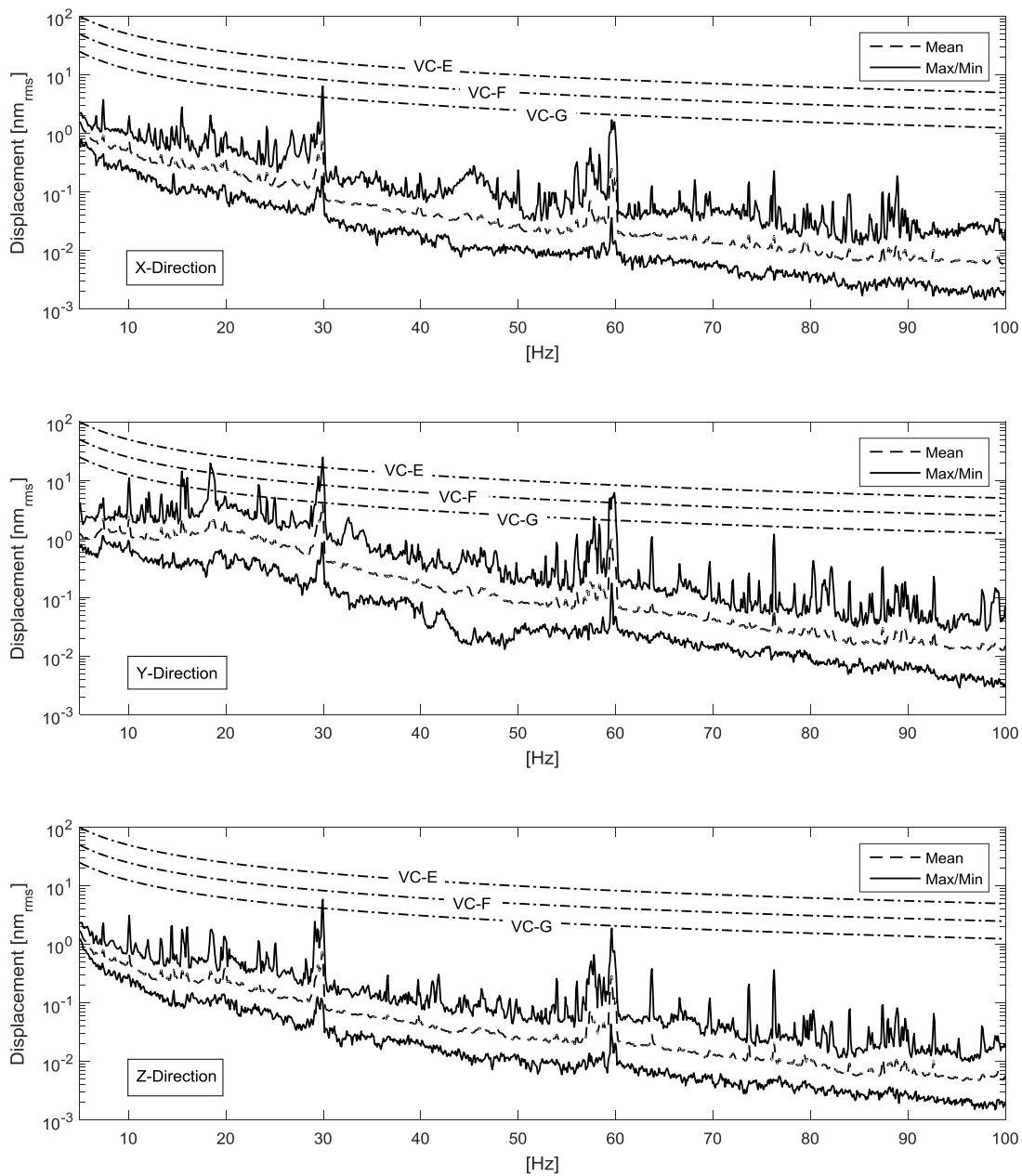


Figure 2. Vibration displacement spectrum of the entire experiment hall for all beamline floors in all 3 directions. The dashed line is the mean of all beamline floors, the solid black line represents the maximum and minimum vibrations of all beamlines, and VC curves are shown with dash dot lines.

3.2 Comparison of Beamline Vibration Bands

One of the goals of this survey was to elucidate locations in the APS experiment hall that are particularly quiet. Using mean RMS displacement data for a particular octave band assigns a single scalar magnitude to a beamline for that band, which makes direct comparison of beamline to beamline much more straight forward. Figures 3-5, display the 5 octave bands for each beamline in the X, Y, and Z directions, respectively. Also included are the mean RMS displacement vibrations for the columns as well.

From the band plots two trends can be seen. The first trend is that the higher the vibration magnitude in the column floor the higher the vibration magnitude of the beamline floor. This can be seen by following the trend of the column curve which then mirrors the beamline curves, particularly in the octave bands 1-3. In octave bands 4 and 5 we start to see a separation in magnitude, which makes sense as higher frequency vibrations dampen at a much greater rate than low frequency vibrations. However, even with the separation in magnitude the trends of column and beamline seem to still have the same general profile.

The second trend is that there is a clear region of the experiment hall that has particularly low magnitude vibrations. This region is located approximately in beamlines 10-20. However, in the bands 4 and 5 there seems to be a greater variation from beamline to beamline. Even beamlines right next to each other can have much higher vibration magnitudes, which is also reflected in the columns. This might be in direct response to a particularly noisy localized area in the mechanical mezzanine floor. There are also two major outliers. In the maximum extreme is beamline 29, and it is clear that column 152 nearby 29-ID is also particularly noisy. So, it is likely that the high vibrations at 29 are from some noisy source on the mezzanine nearby. On the other hand, is the minimum extreme, and this is located at beamline 16, especially in the Y direction. Beamline 16-ID is unique in that the floor is actually a bridge over a road access tunnel. It is possible that being constructed on a bridge structure the floor is more isolated from the lower frequency noise associated with ground motion and traffic, and that noise from the mechanical equipment on the mezzanine floor has a longer direct path to the beamline floor allowing for greater damping of vibrations by the time they reach the measurement point.

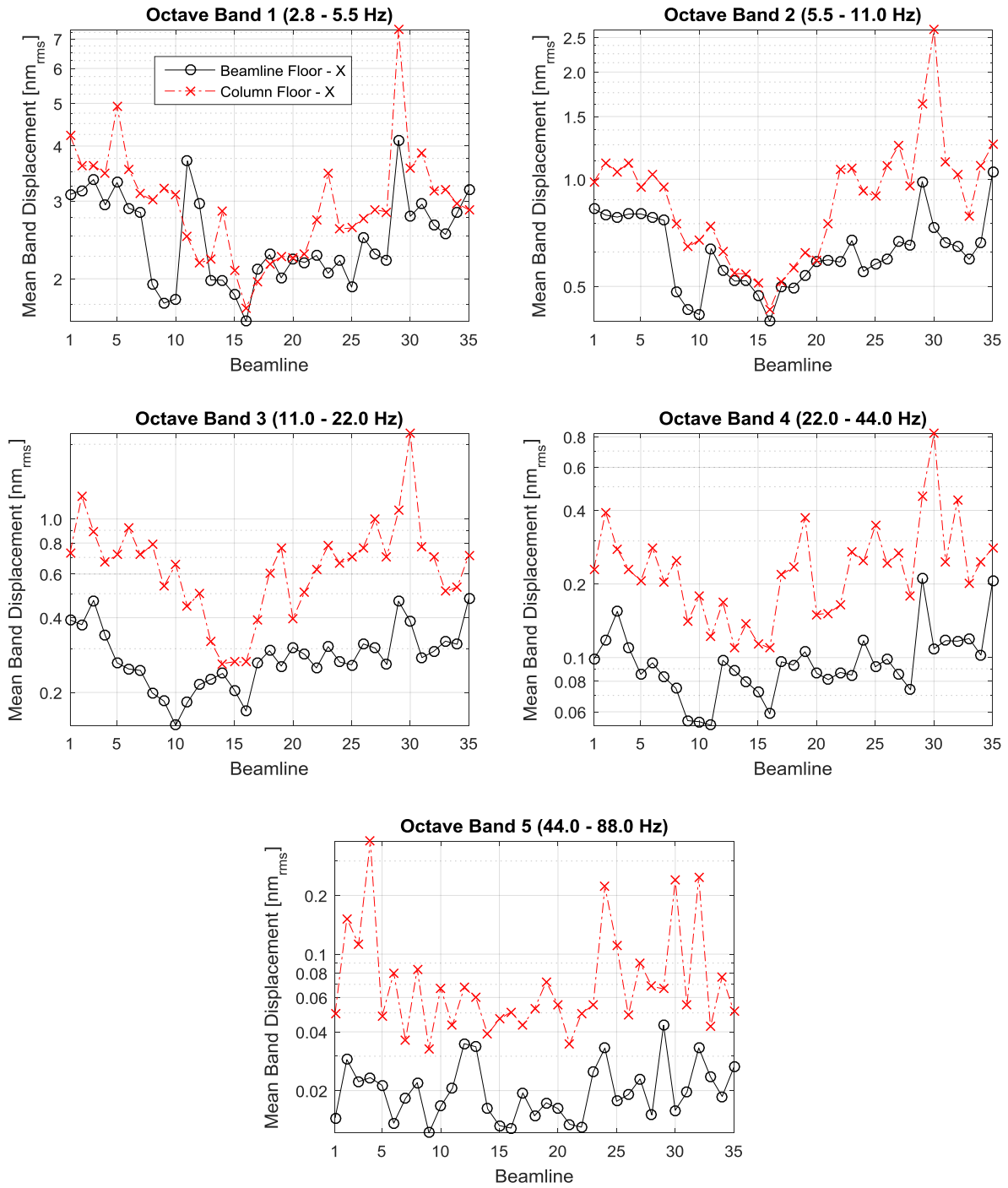


Figure 3. Mean displacement vibration for all beamlines in the X direction for each octave band.

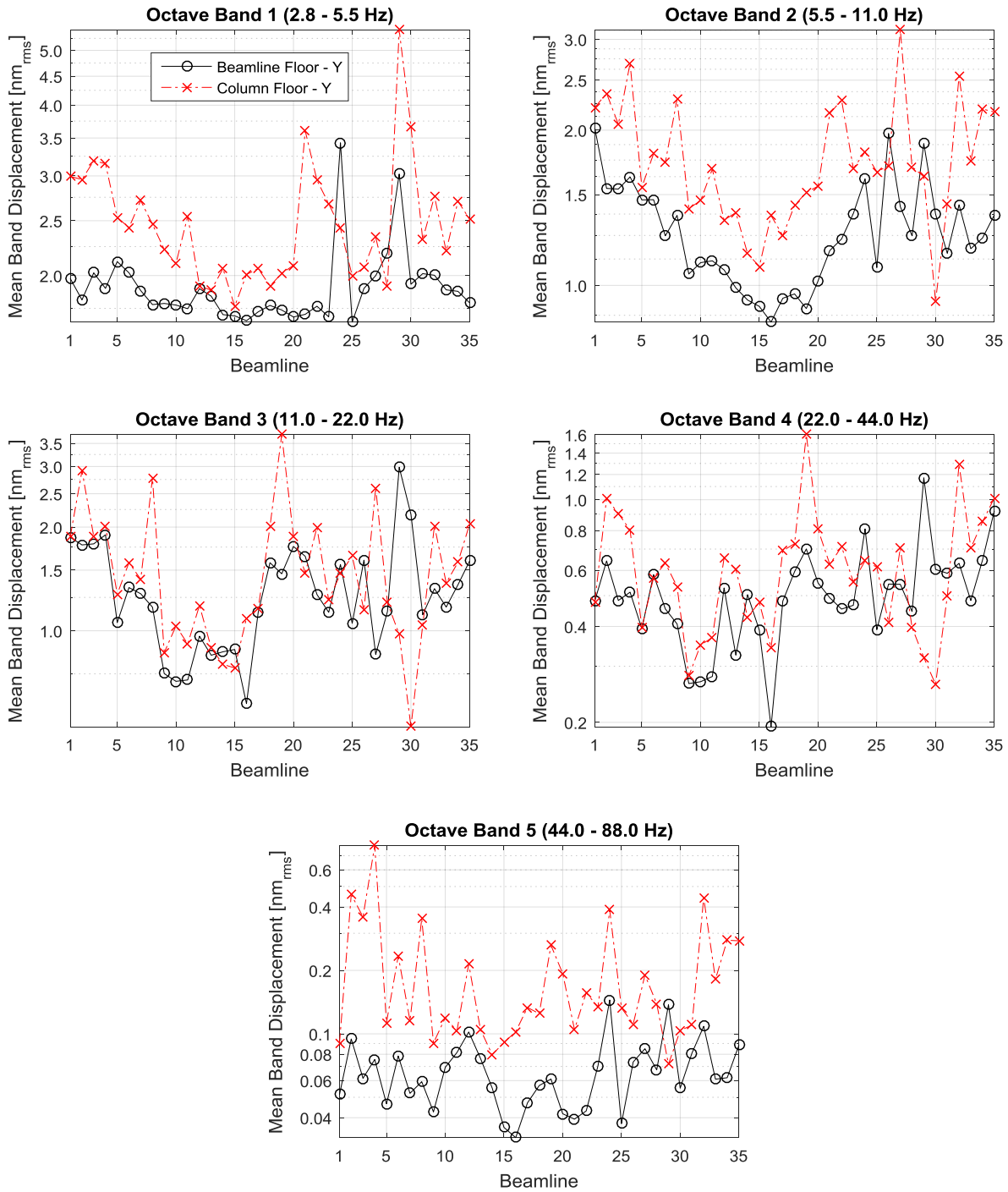


Figure 4. Mean displacement vibration for all beamlines in the Y direction for each octave band.

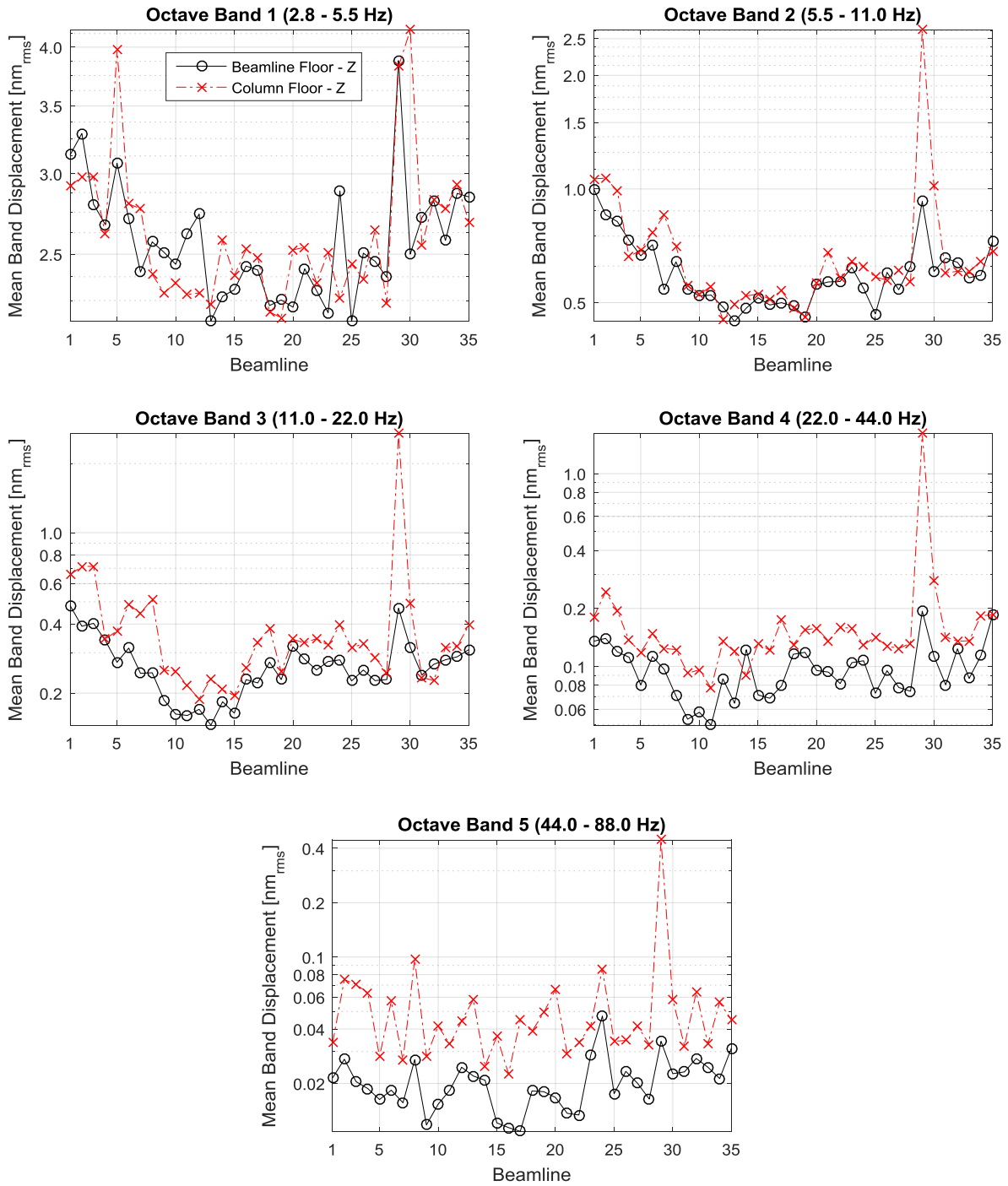


Figure 5. Mean displacement vibration for all beamlines in the Z direction for each octave band.

3.3 Contribution of Mechanical Equipment to Noise

In addition to the survey of floor vibrations a unique opportunity presented itself to measure the floor vibrations while the power to mechanical equipment was off. Vacuum pumps, DI pumps, and air handling equipment, all located on the mezzanine floor, were shut off for electrical maintenance in sectors 20-23. The same measurement points as when power was on during the initial survey was then measured again during the shutdown for beamline 21.

First, looking at the difference in column floor vibrations with power on and off, see Figure 6, we can see that there is a noticeable reduction in vibration magnitude throughout much of the spectrum. This is particularly evident in the X direction, and in the Y direction the reduction seems to be localized to the 10-60 Hz range. The 10-60 Hz range makes sense as this is the range in which the equipment normally produces vibration noise. There is almost no visible reduction in the Z direction, which suggests that the column is stiffer in that direction.

Now looking at 21-ID beamline floor vibrations, Figure 7, we can see similar reductions across the spectrum as was seen in the column. The reduction in the Y direction is, in this case throughout the entire spectrum, however the largest reduction is still in the 10-60 Hz range. In this case the 10-60 Hz reduction is seen in all three directions, which is likely from a combination of vibrations of multiple columns from varying angles to the measurement point contributing to the vibration noise. From this data it can be concluded that the columns represent a significant source, approximately a half order of magnitude increase of vibrations at various frequencies, and any reduction in vibration noise to mechanical equipment on the mezzanine floor should have a measured reduction in vibrations on the beamline floor.

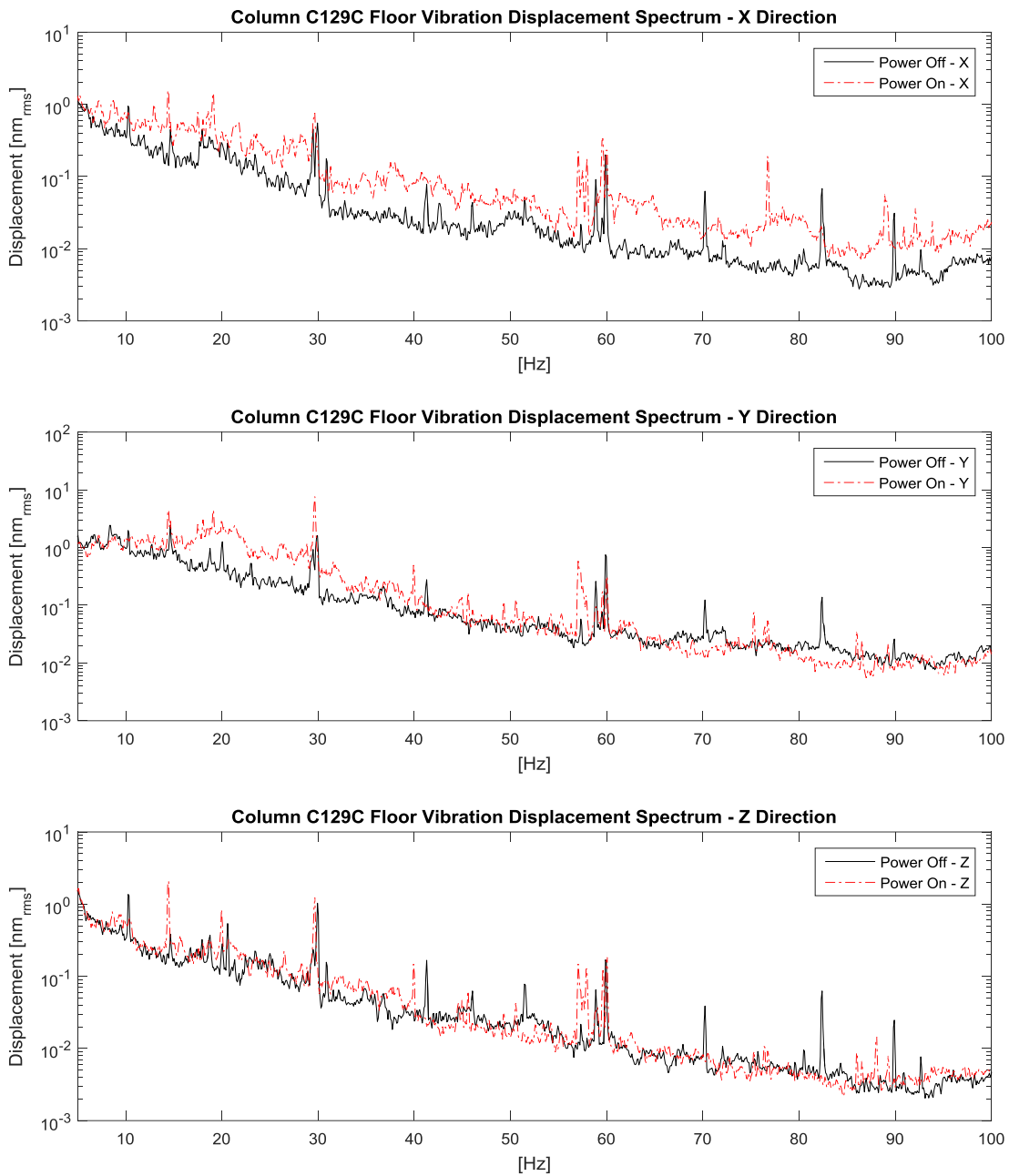


Figure 6. Comparison of column C129C floor vibration displacement spectrum with the power on and power off to the mechanical equipment on the mezzanine.

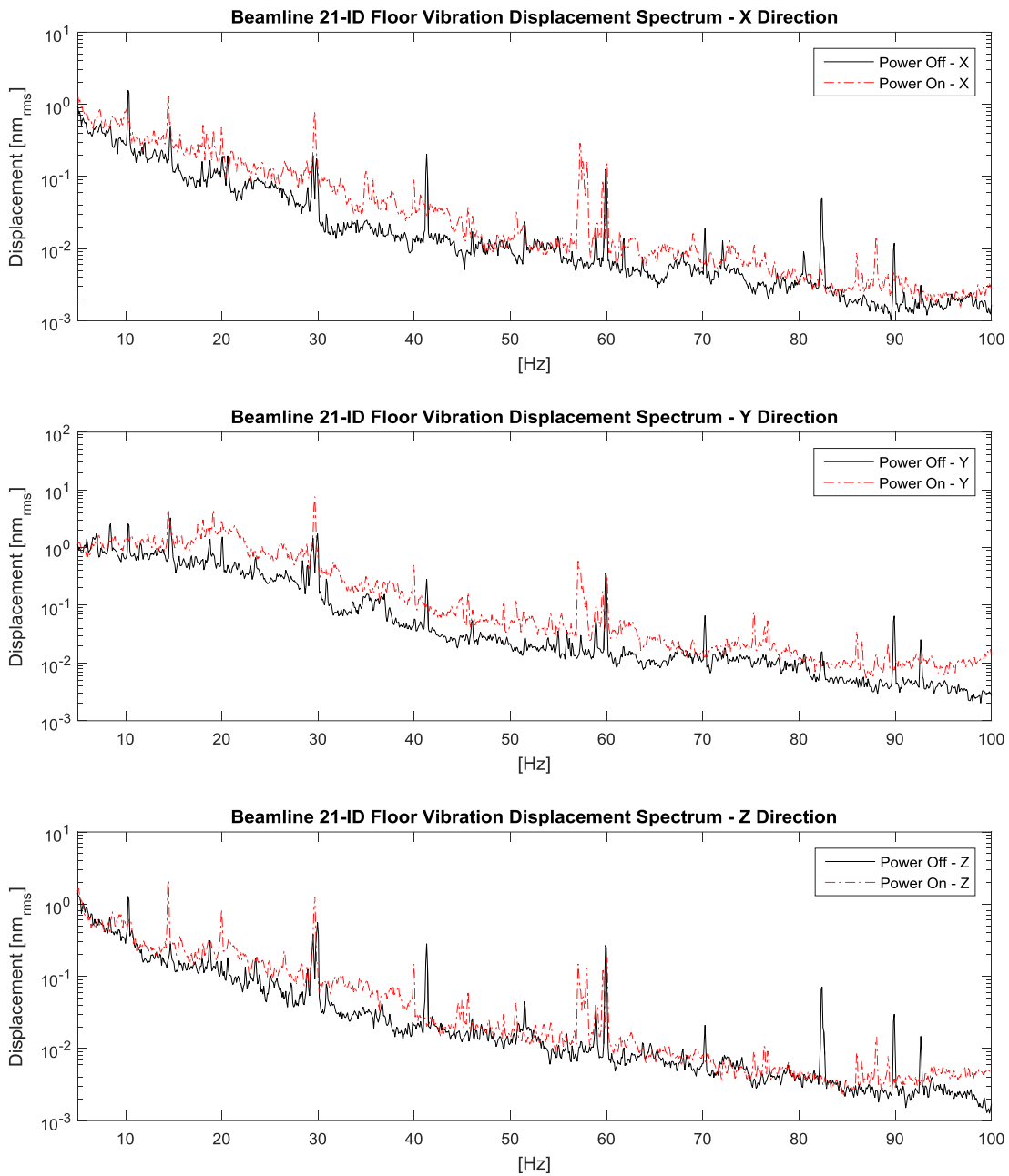


Figure 7. Comparison of the beamline floor vibration displacement spectrum with the power on and power off to the mechanical equipment on the mezzanine.

4 Conclusions

A survey of the experiment hall at the APS was conducted and several conclusions can be gained from this survey. It was found that the entire APS experiment hall is an extremely vibration quiet research facility when compared to the VC curves from NEST. Even though, it was found that some regions of the floor have even lower magnitude vibrations than others, particularly beamlines 10-20. In the lower frequency bands, up to 22 Hz, local similarity of vibration magnitudes could be seen, however above 22 Hz variation was seen from one beamline to the next. It was found that the column vibrations mirrored those of the nearby beamlines, and when the power was turned off to the mechanical equipment on the mezzanine the affected column and beamline floor had visible reductions in vibration magnitudes. This all points to the columns being a primary conveyor and source of vibration noise to the experiment hall floor. It is hoped that the results and conclusions of this survey will be used in support of the selection of future beamline construction areas, as a planning tool for future beamline designs, and to help identify sources of vibration noise.

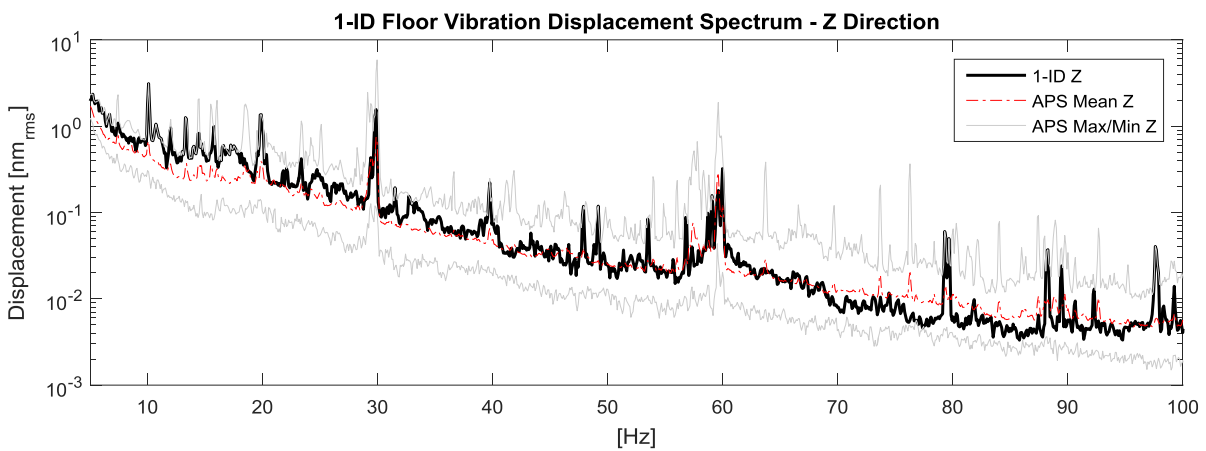
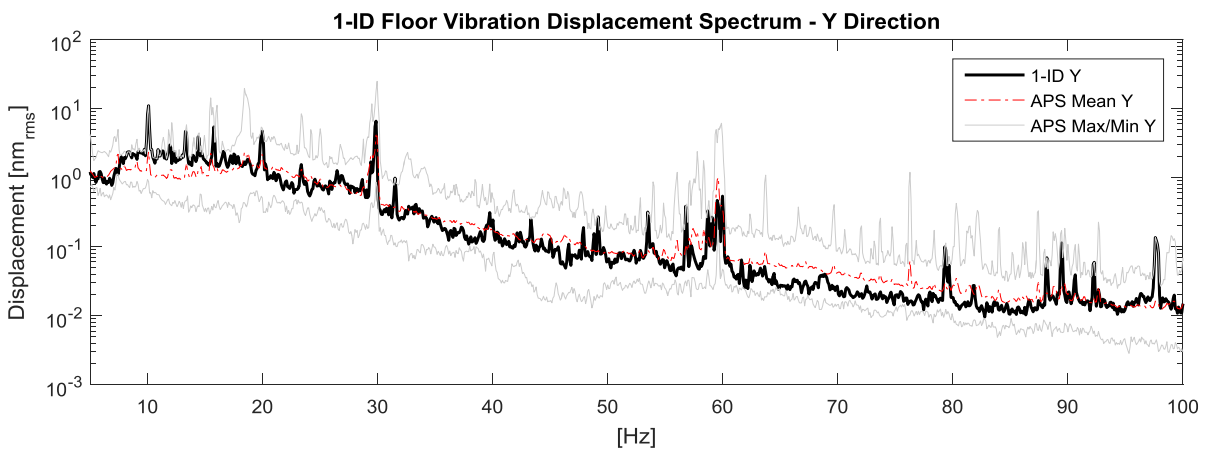
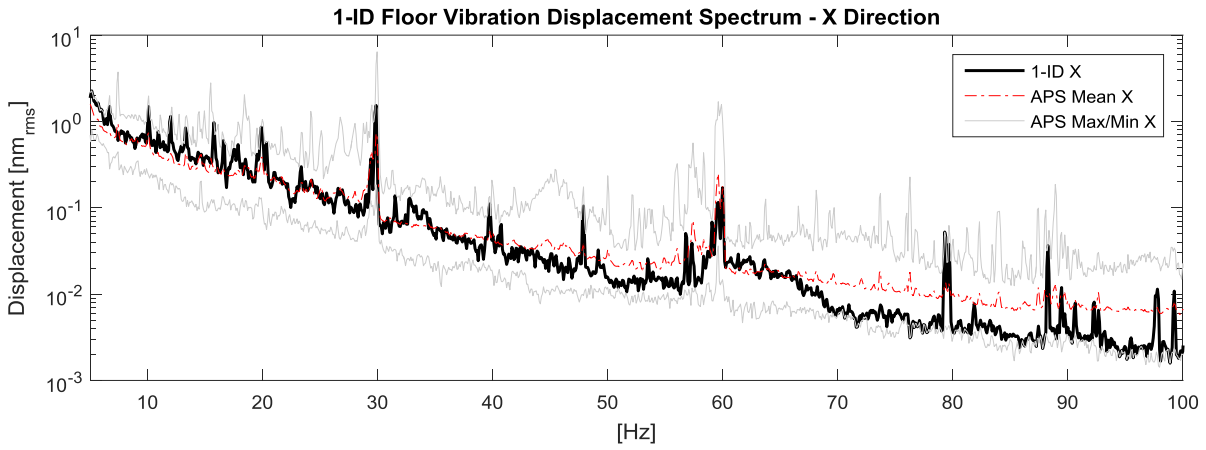
Acknowledgements

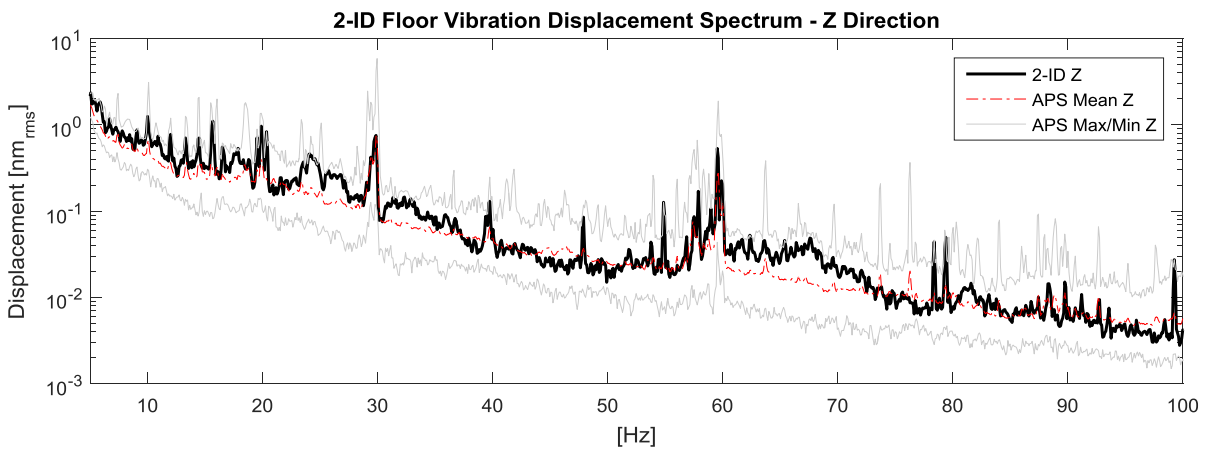
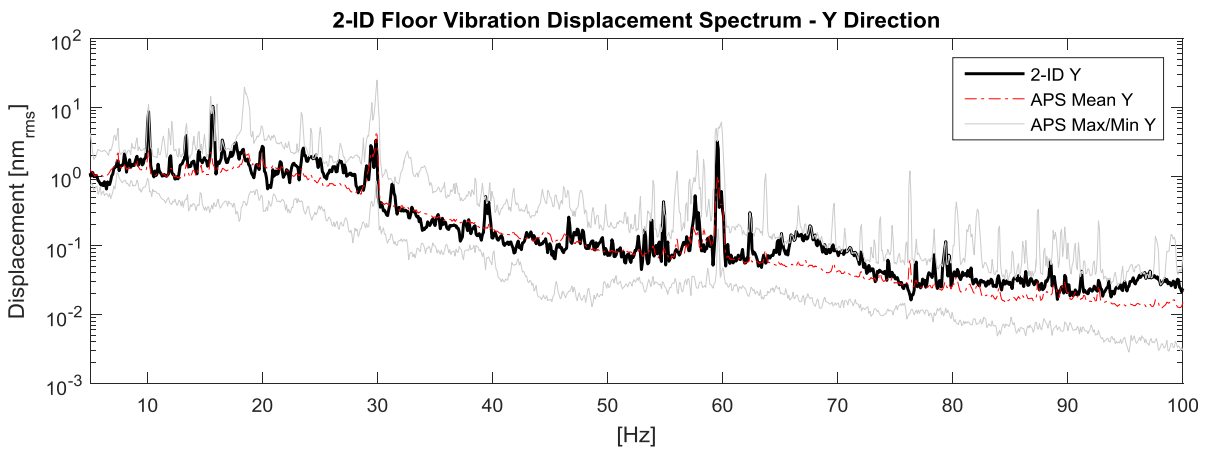
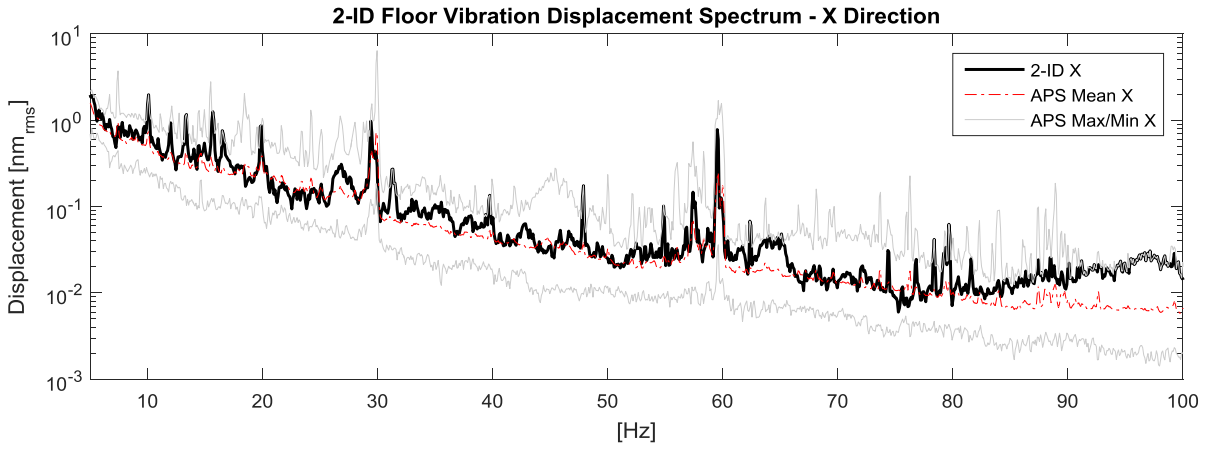
The authors would like to acknowledge Dean Haeffner and Patricia Fernandez for their management and support of this project, and also Curt Preissner for his advice and professional insight into the project. Work supported by the U.S. Department of Energy, Office of Science, under Contract No. DE-AC02-06CH11357.

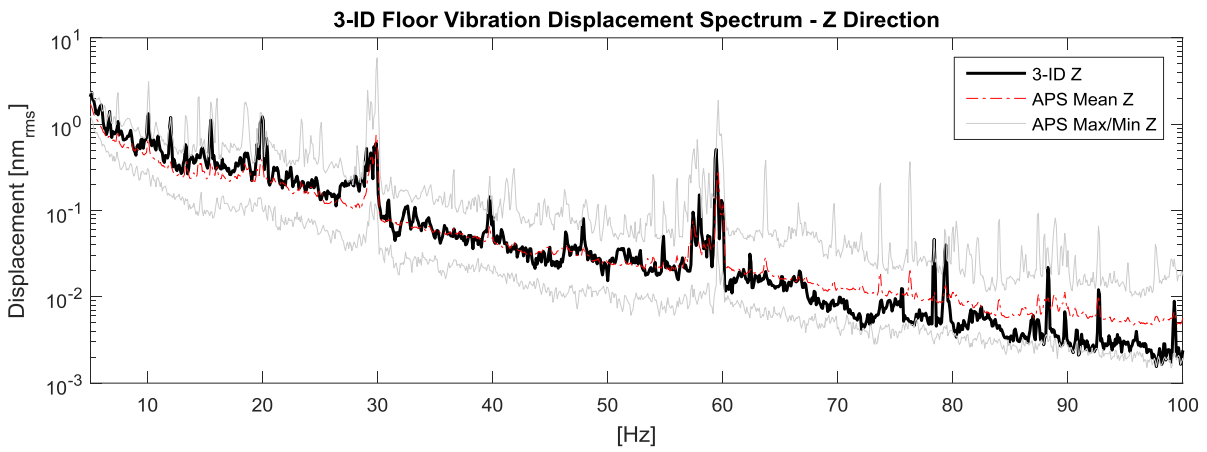
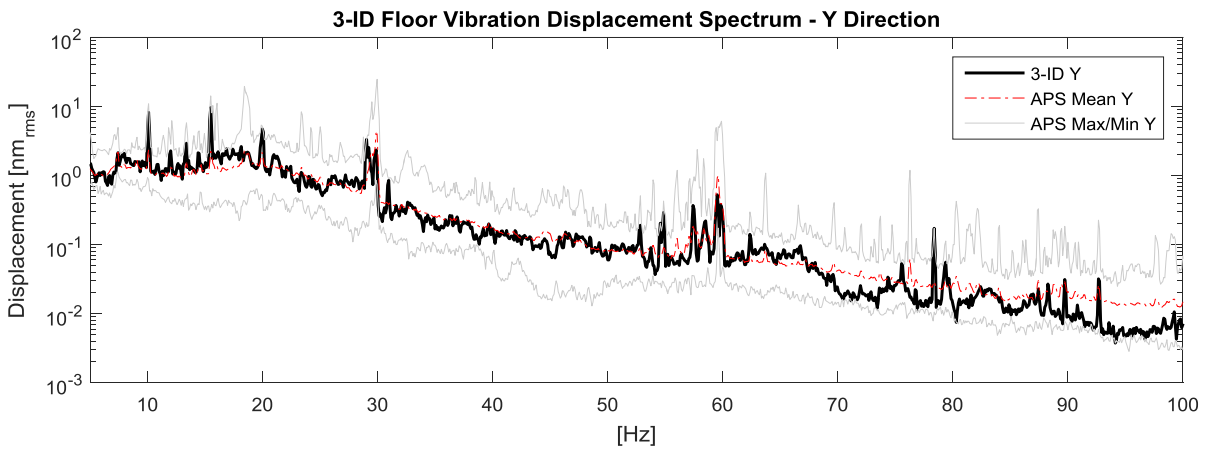
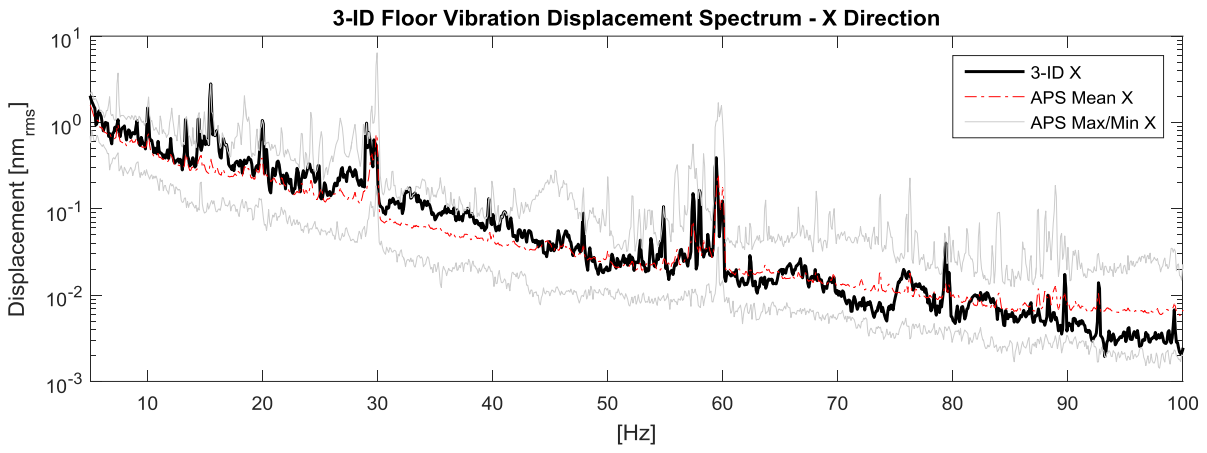
References

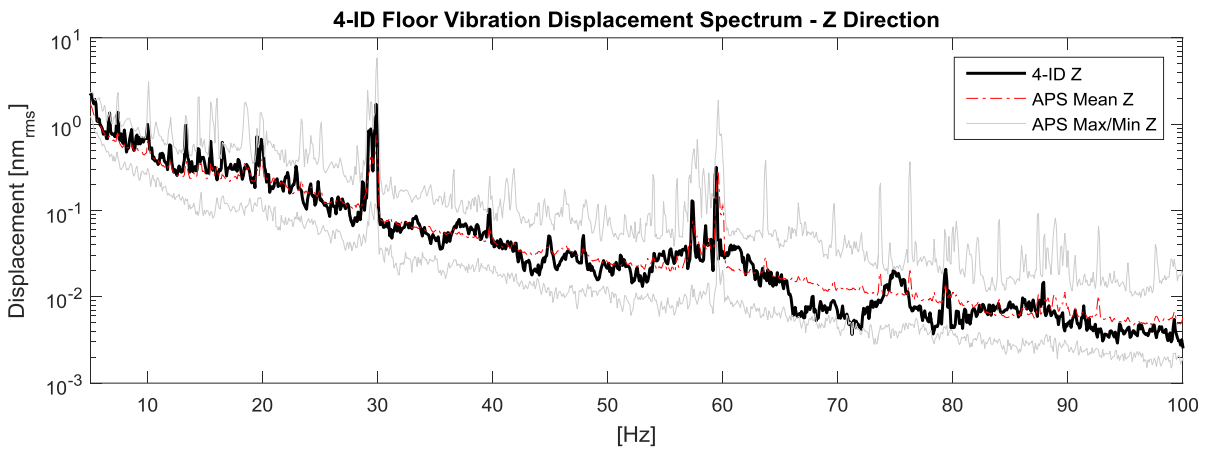
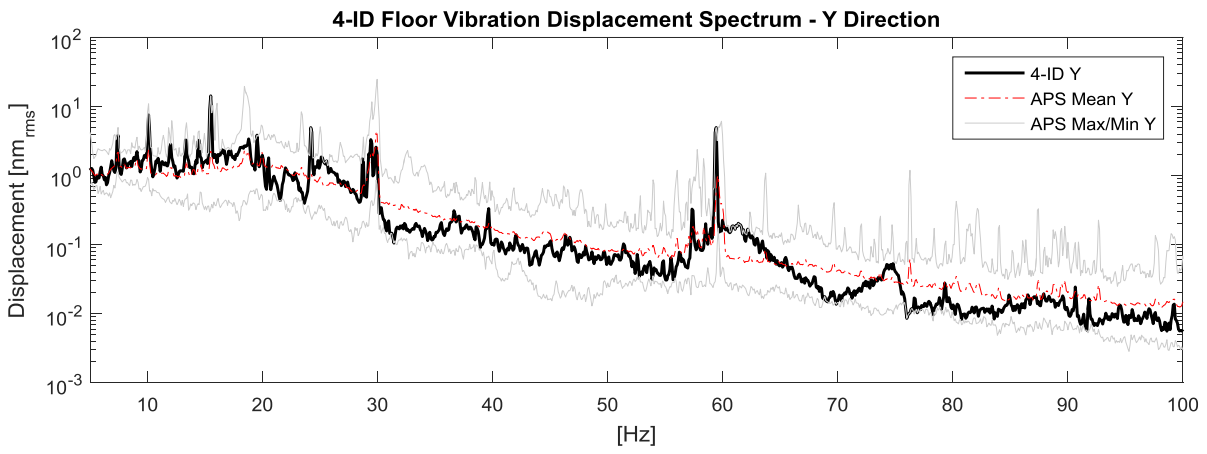
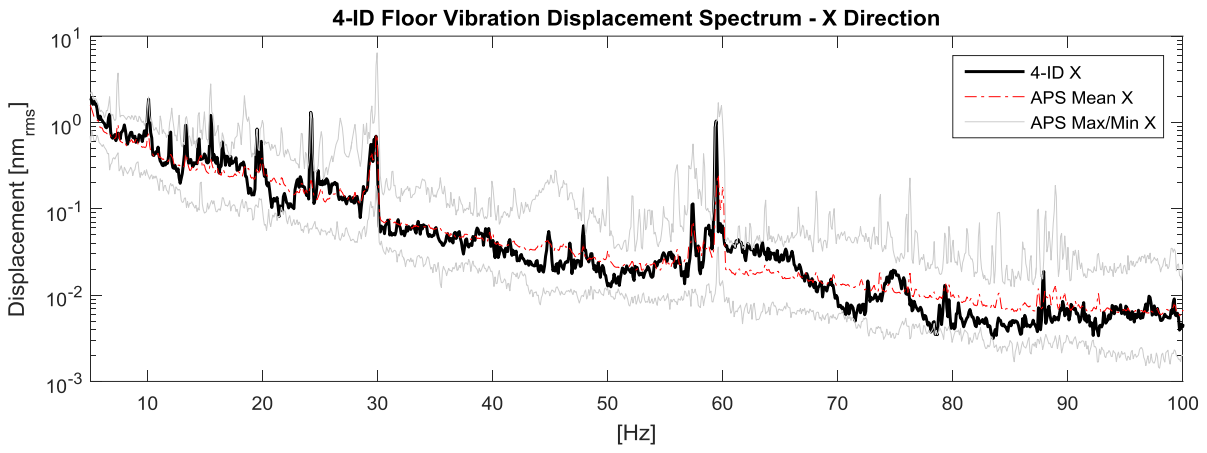
- Amick, Hal, Michael Gendreau, Todd Busch, and Colin Gordon. 2005. "Evolving criteria for research facilities: vibration." *Optics & Photonics* 2005.
- Rogers, Melissa JB, Kenneth Hrovat, Kevin McPherson, Milton E Moskowitz, and Timothy Reckart. 1997. "Accelerometer data analysis and presentation techniques."

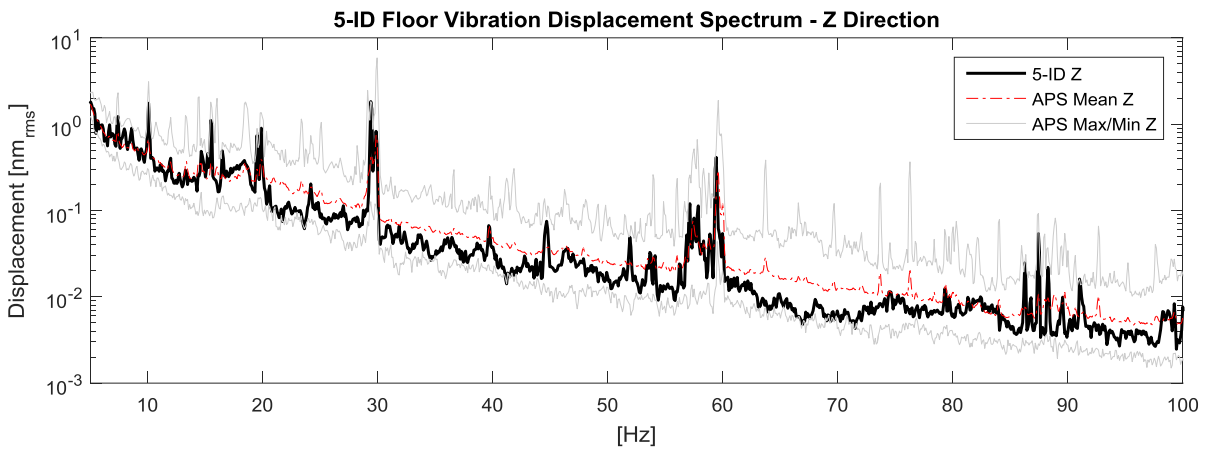
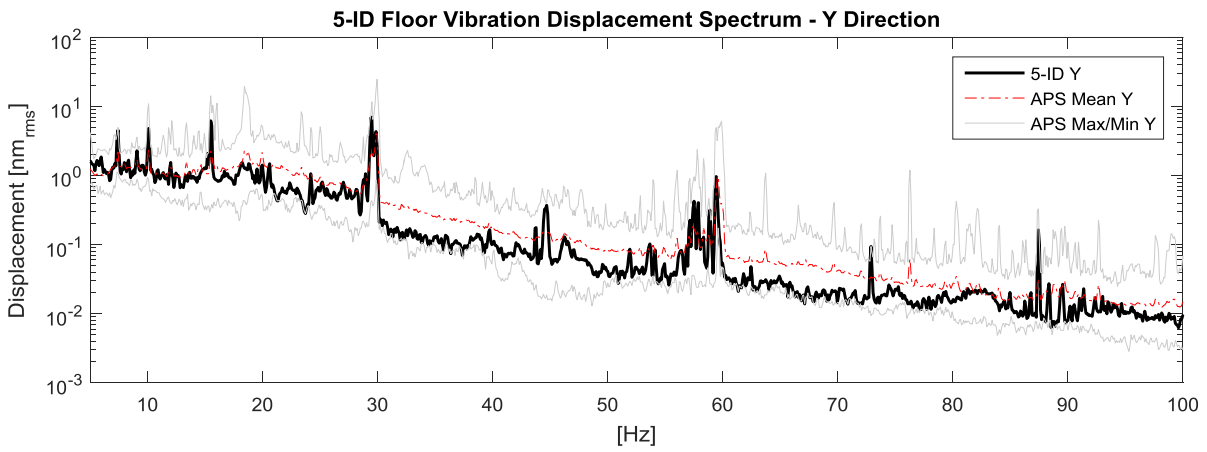
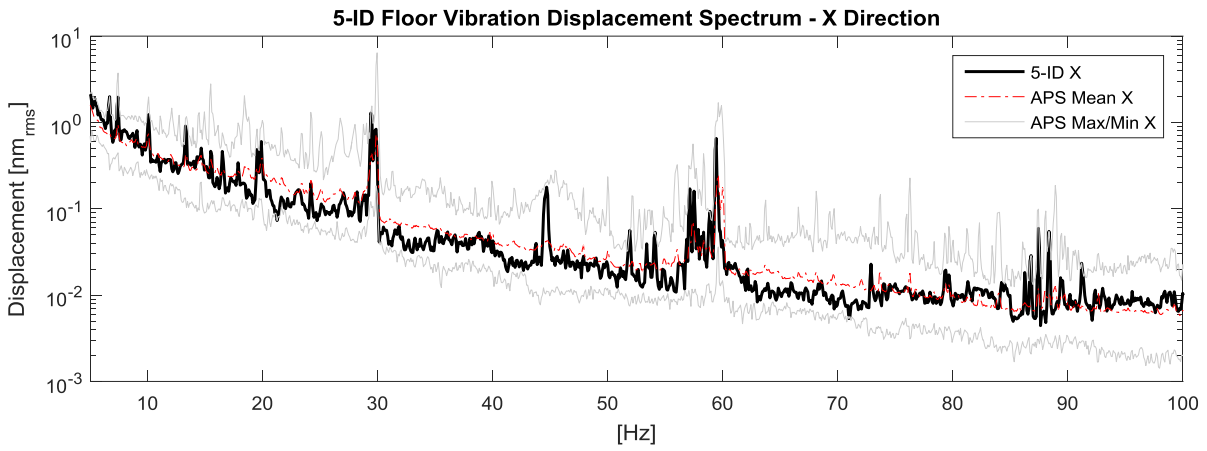
Appendix – Complete Beamline Floor Data Set

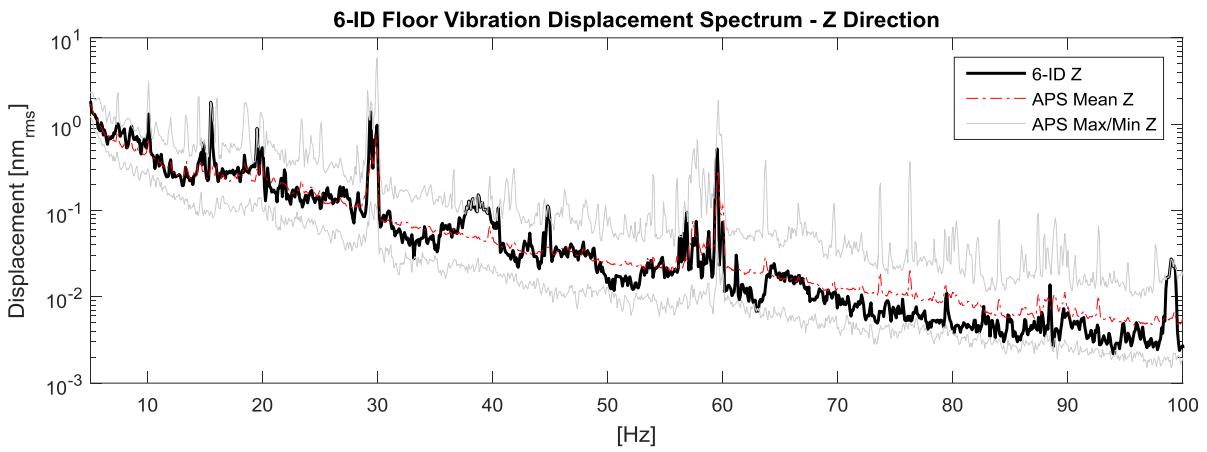
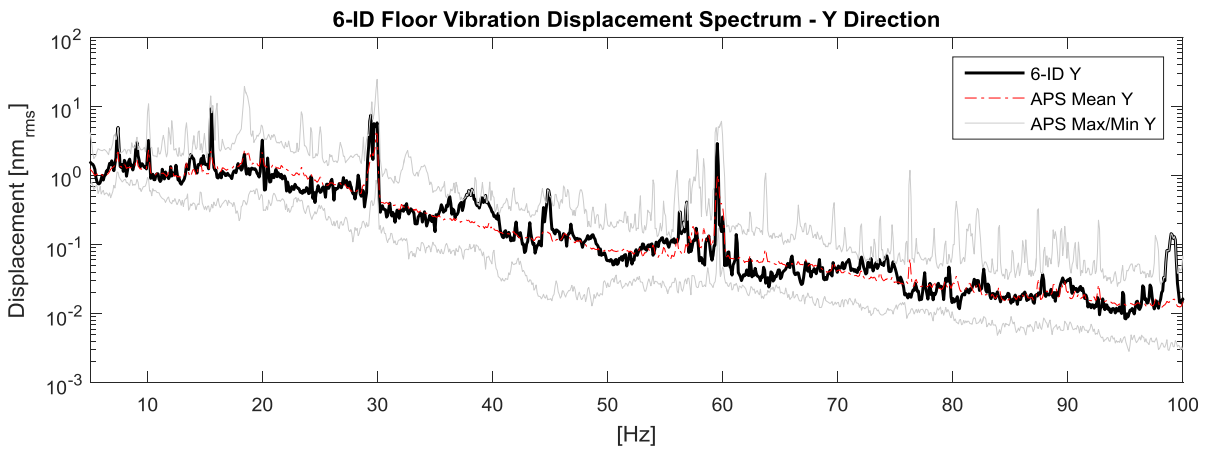
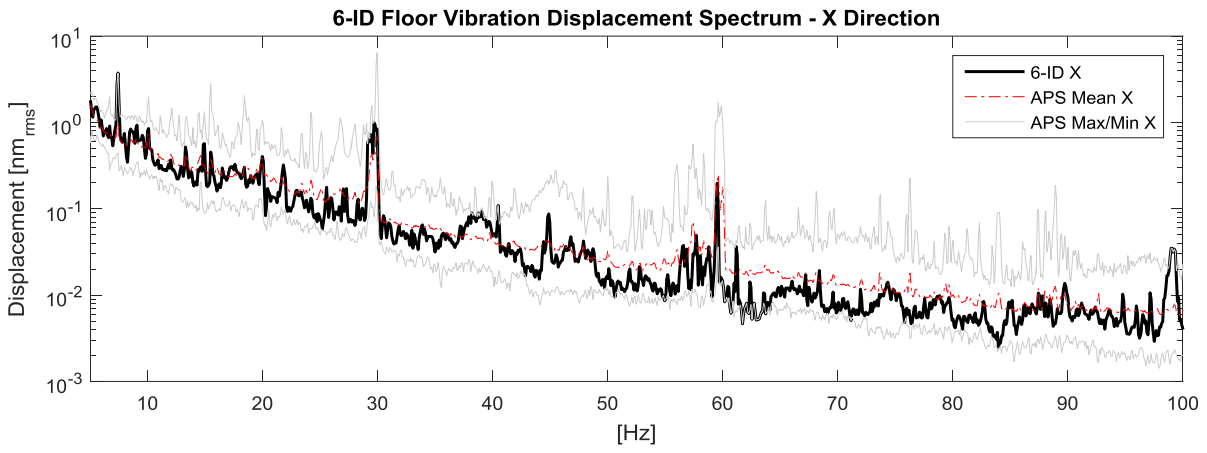


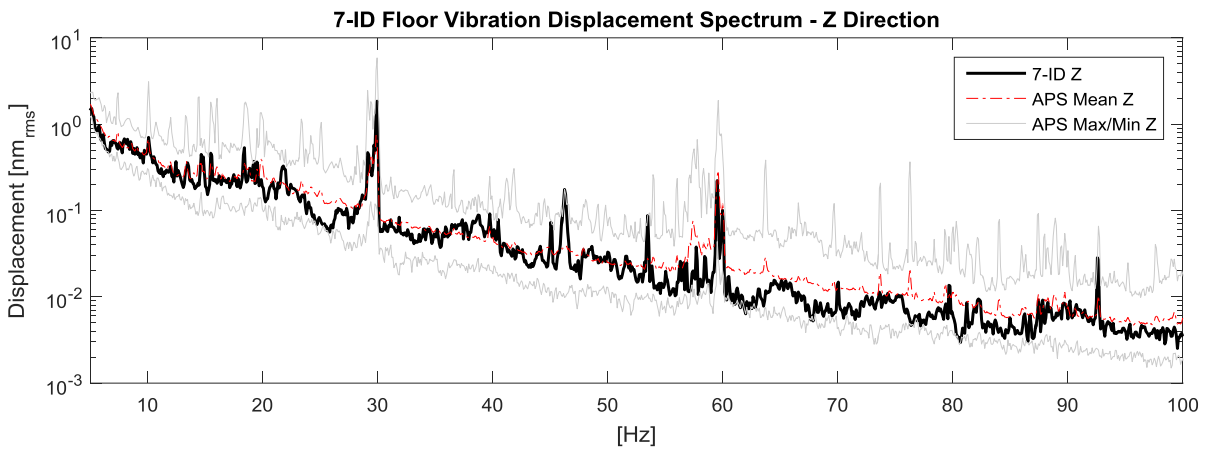
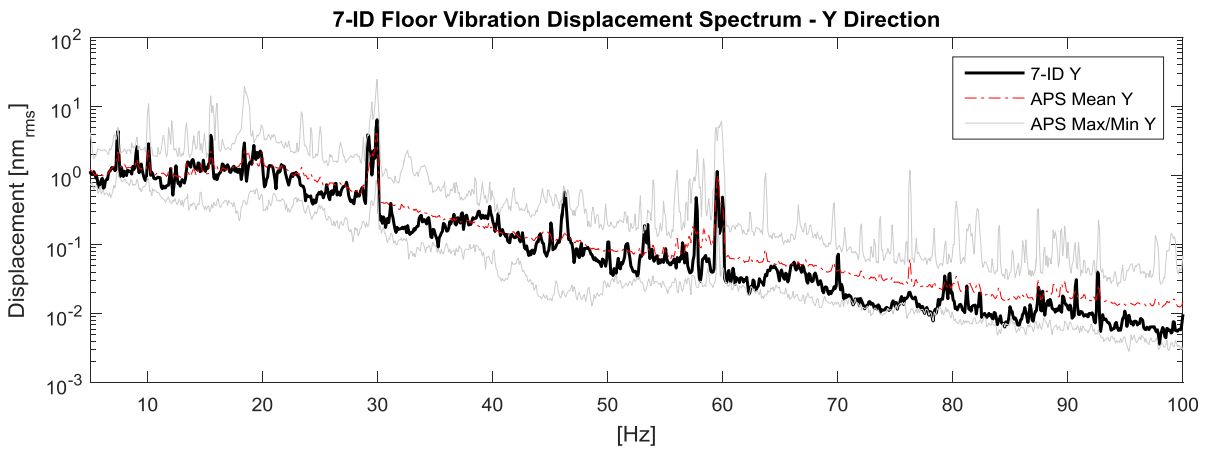
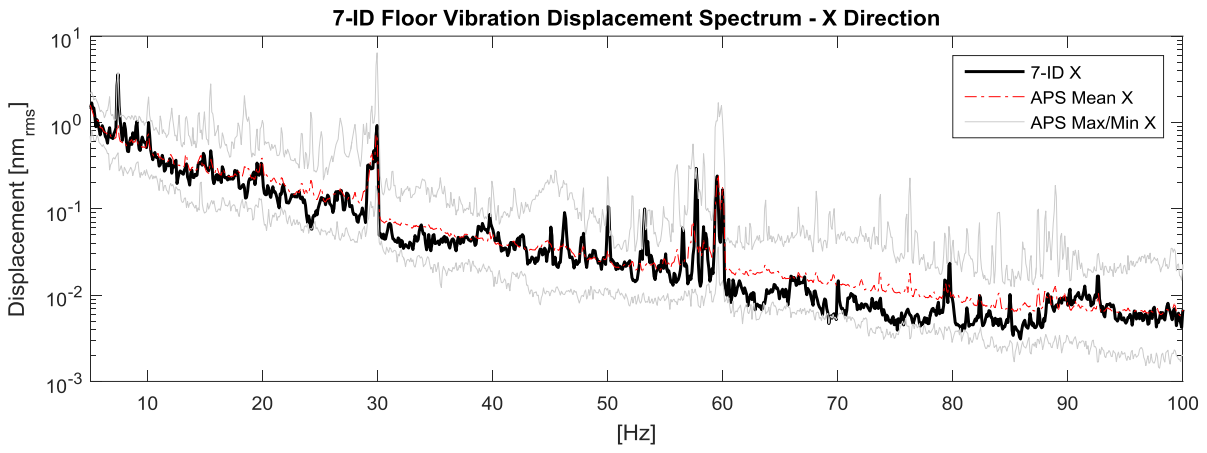


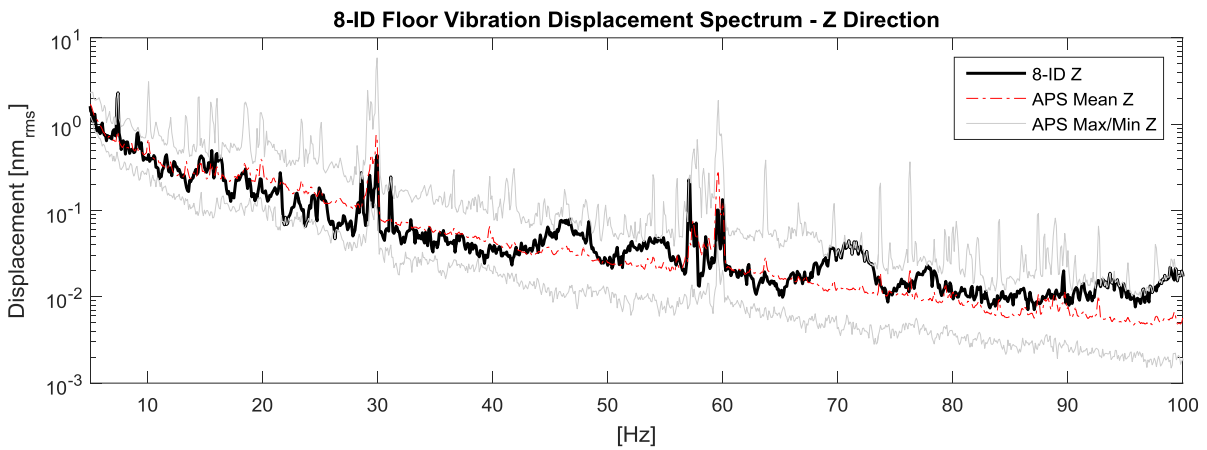
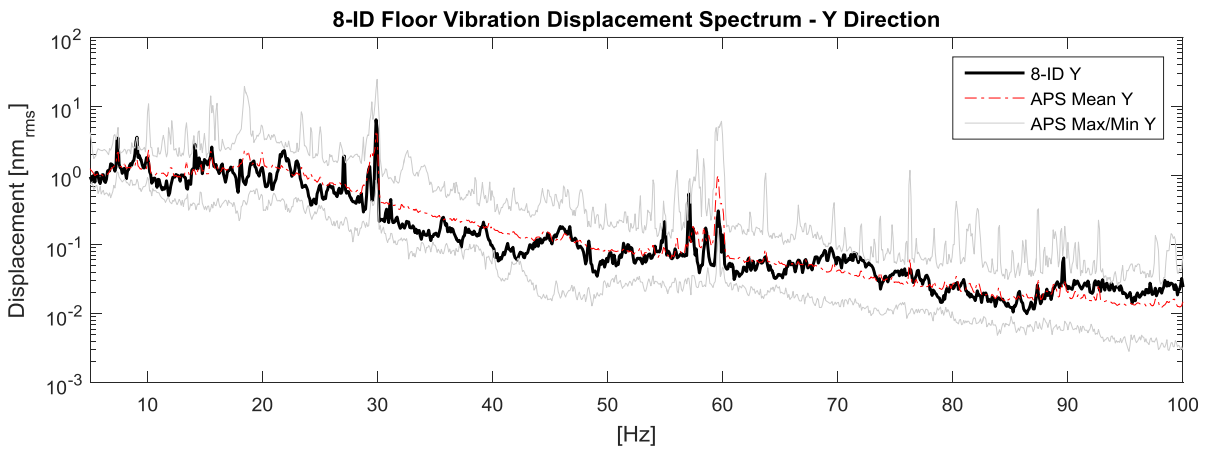
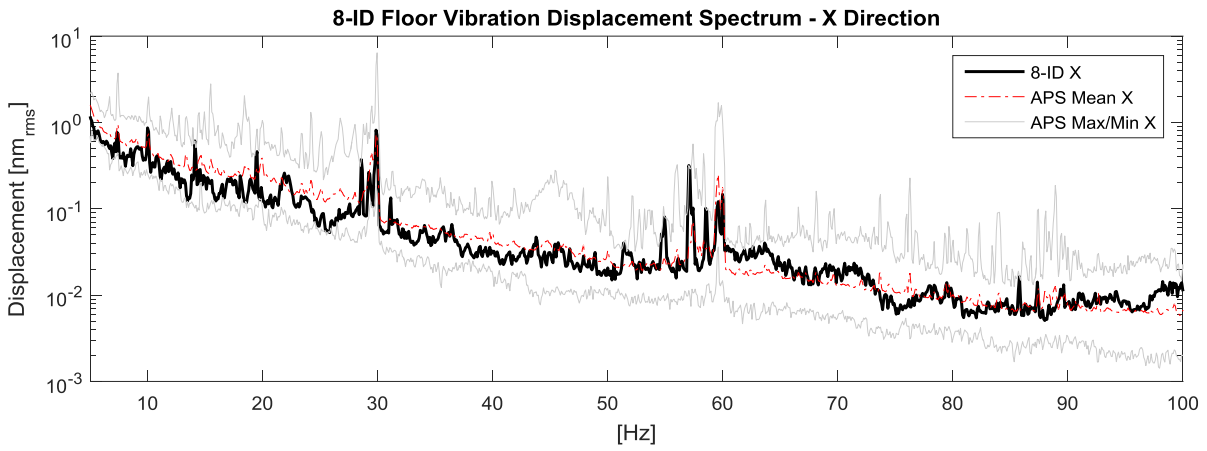


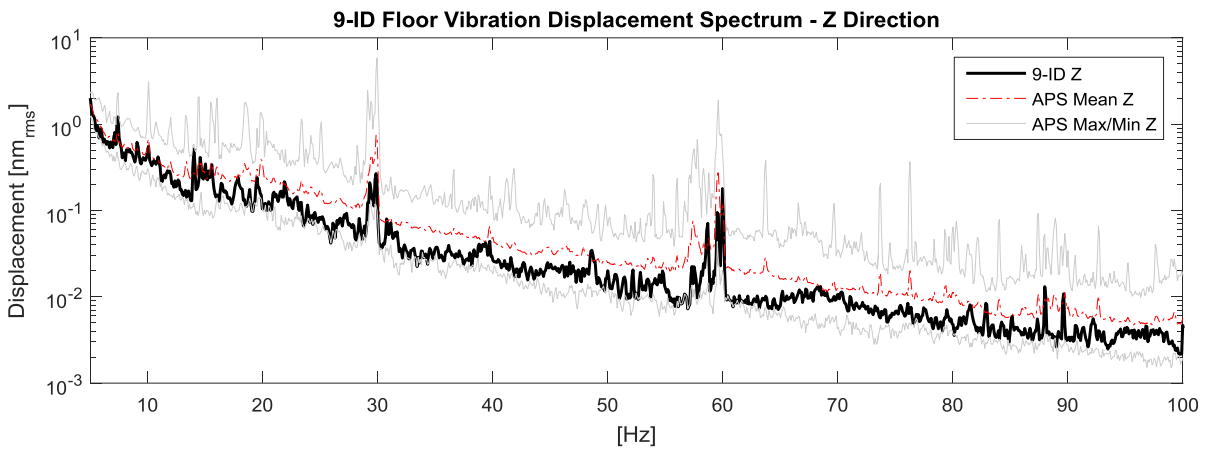
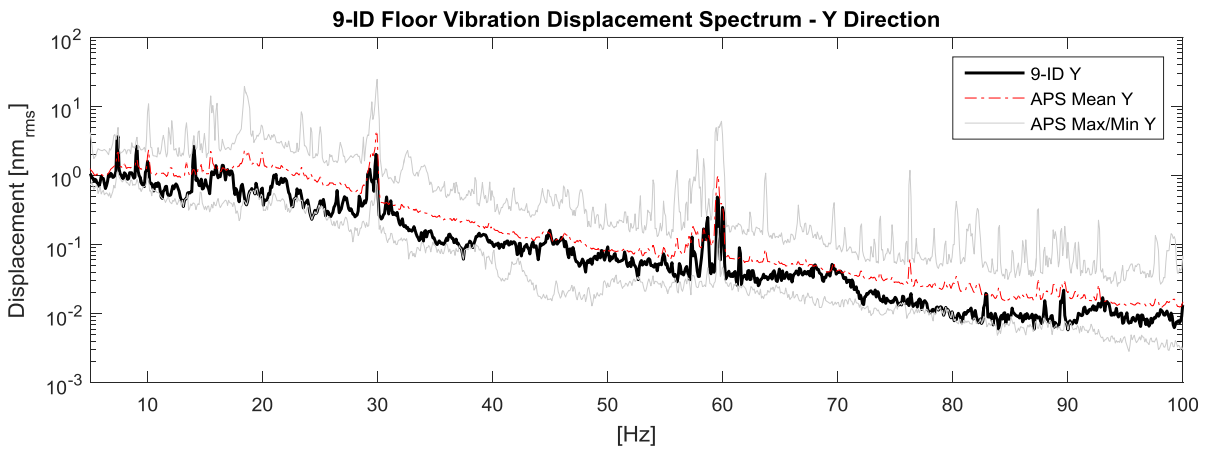
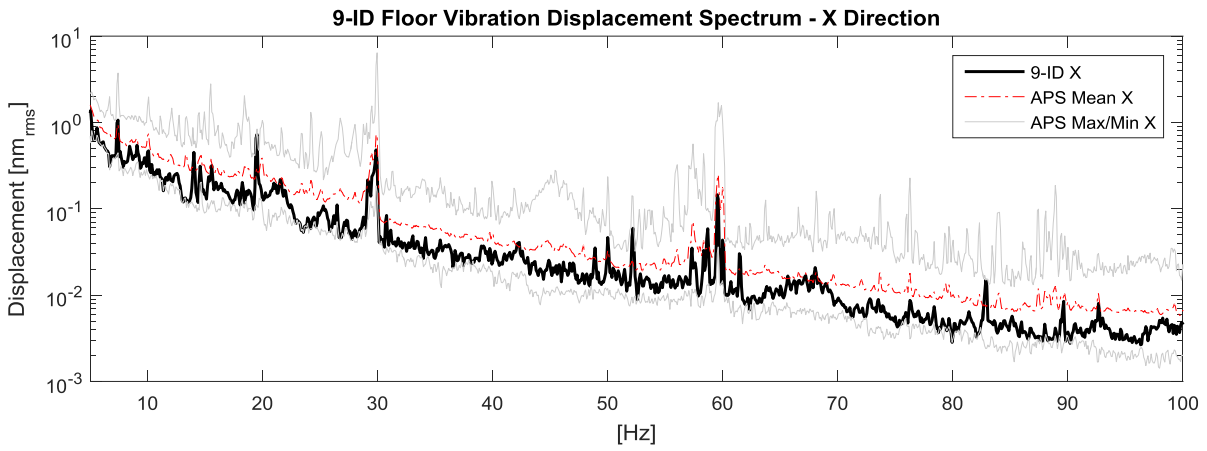


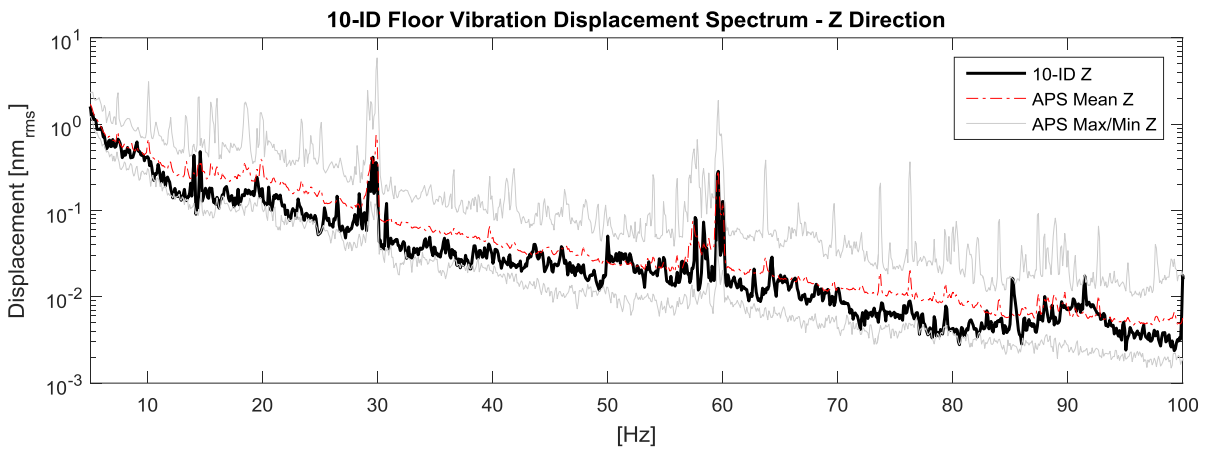
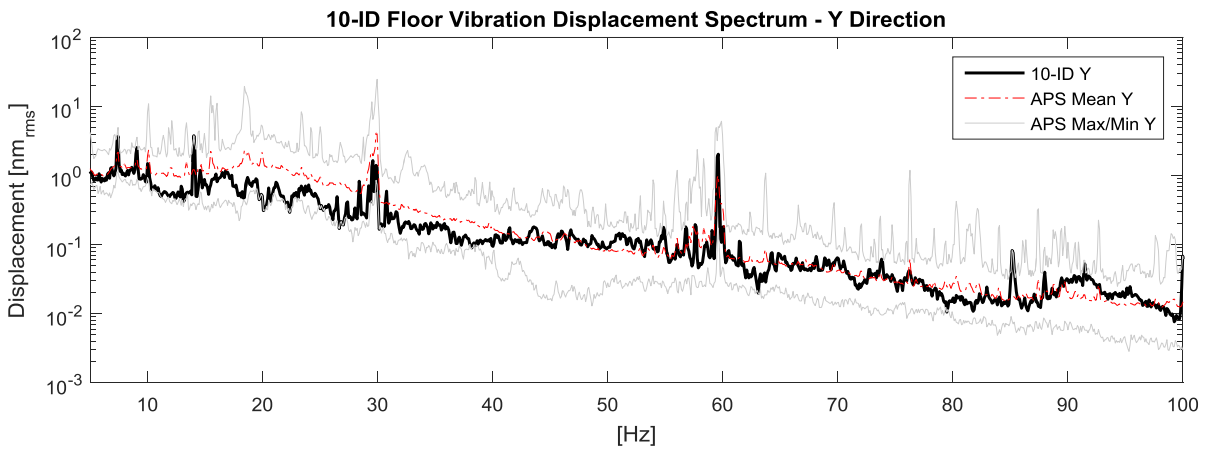
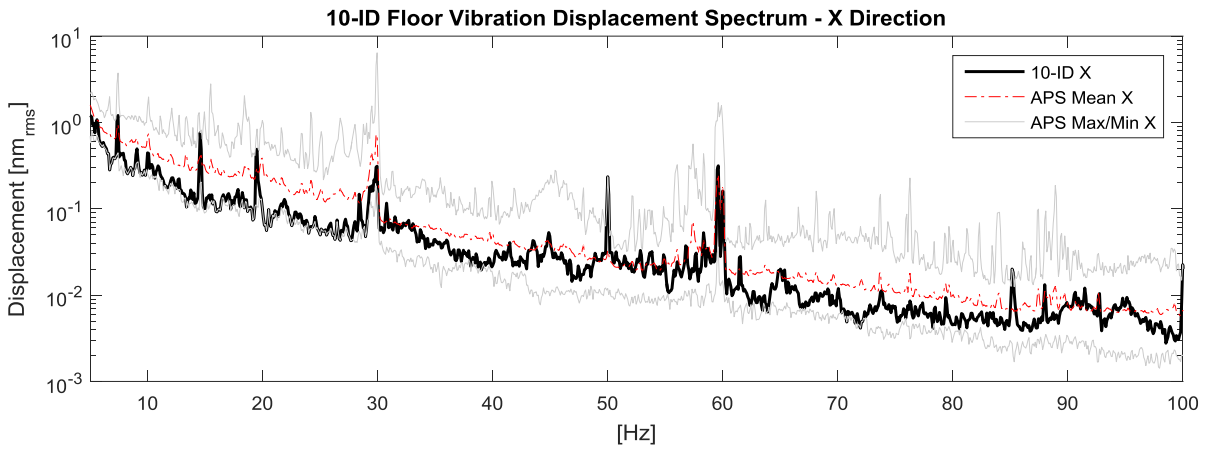


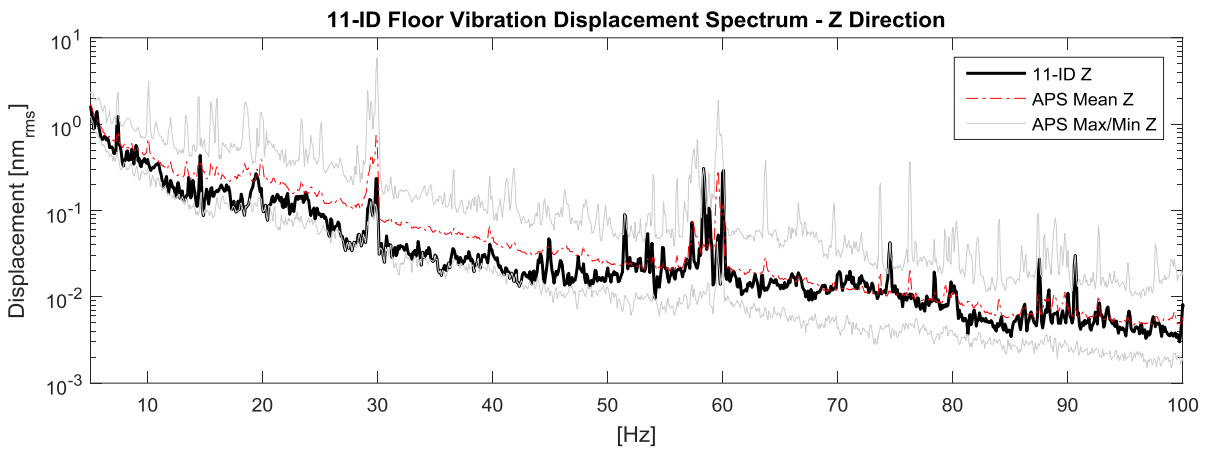
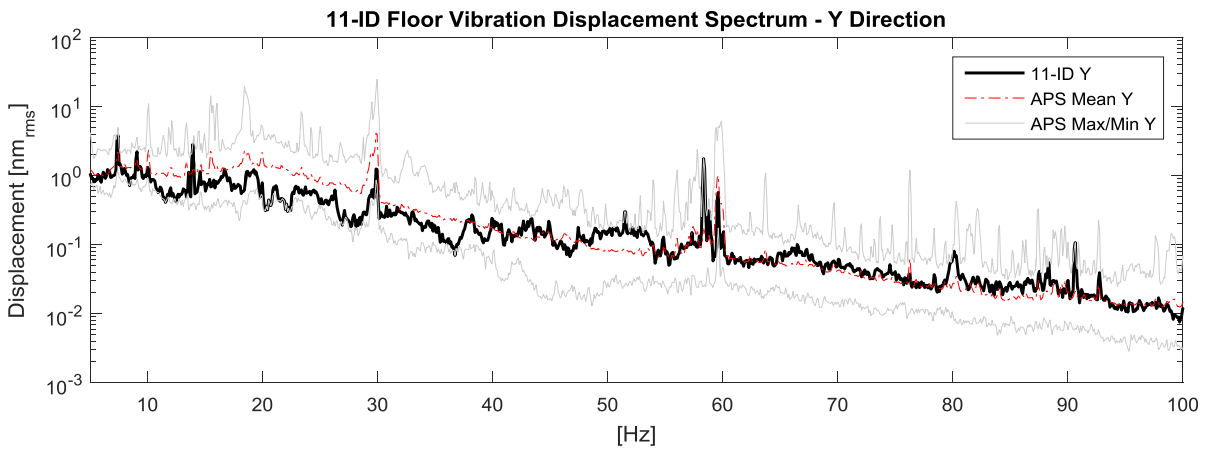
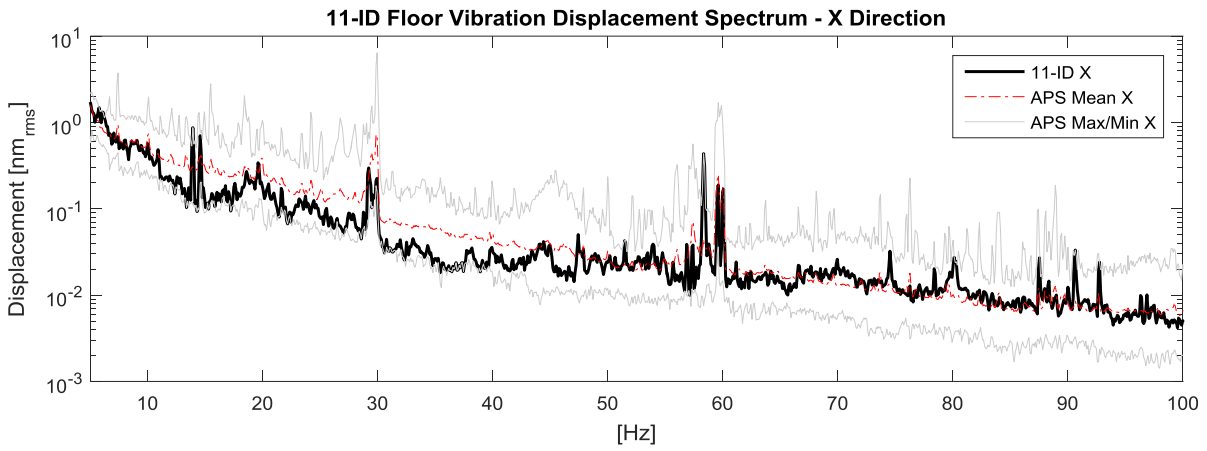


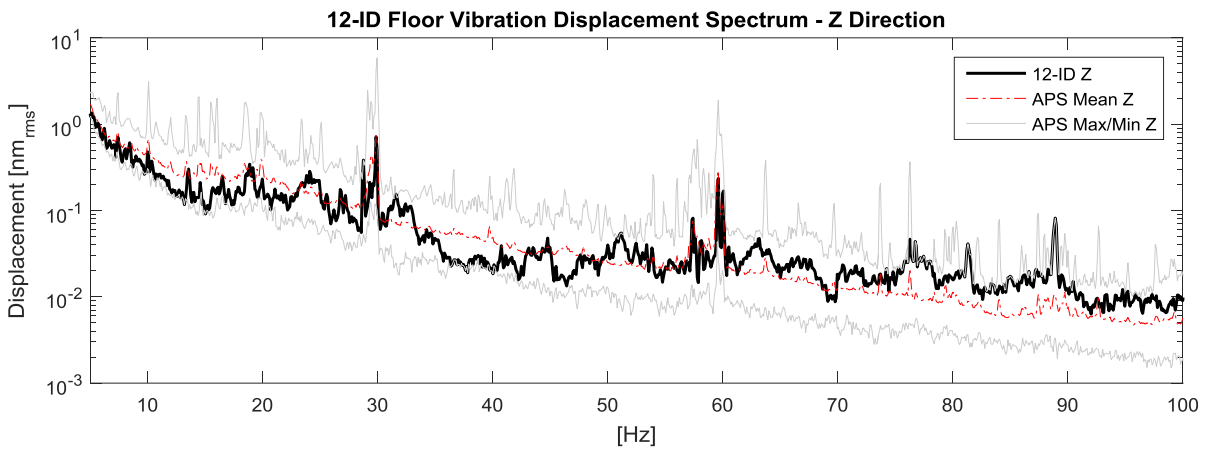
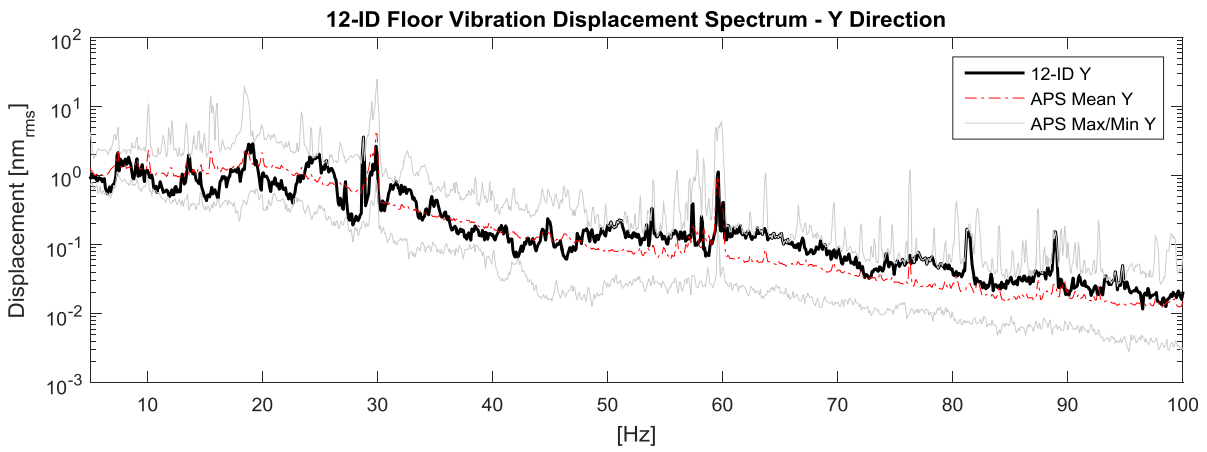
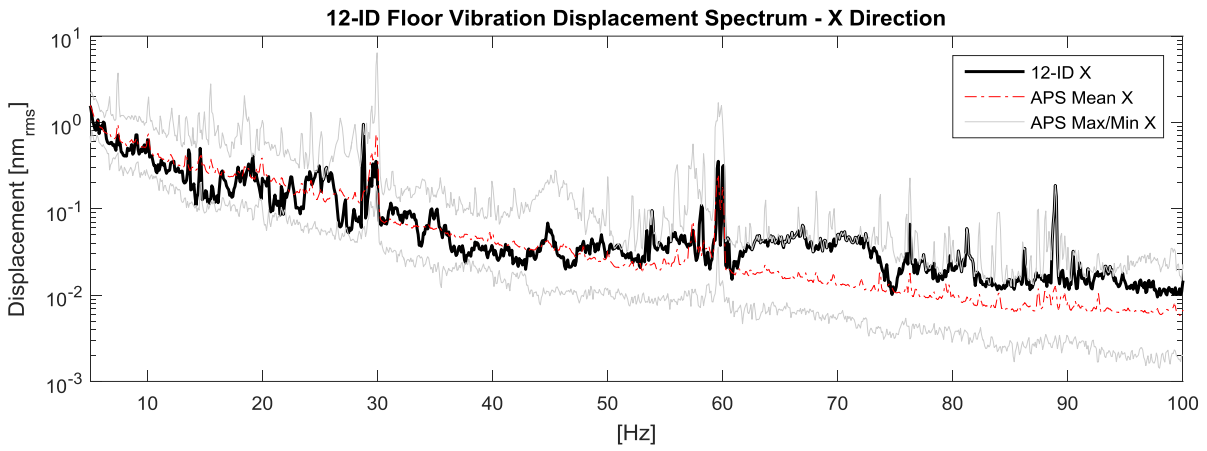


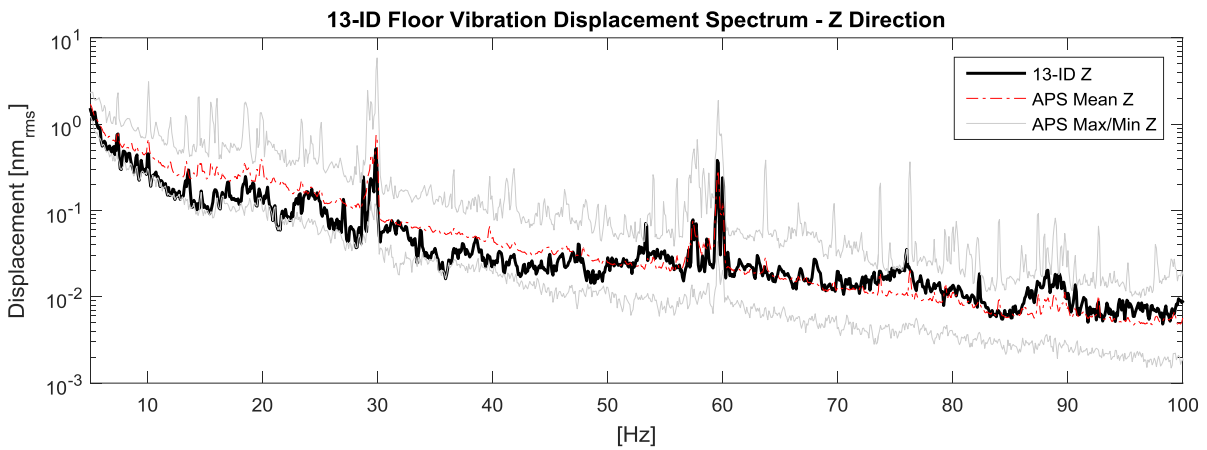
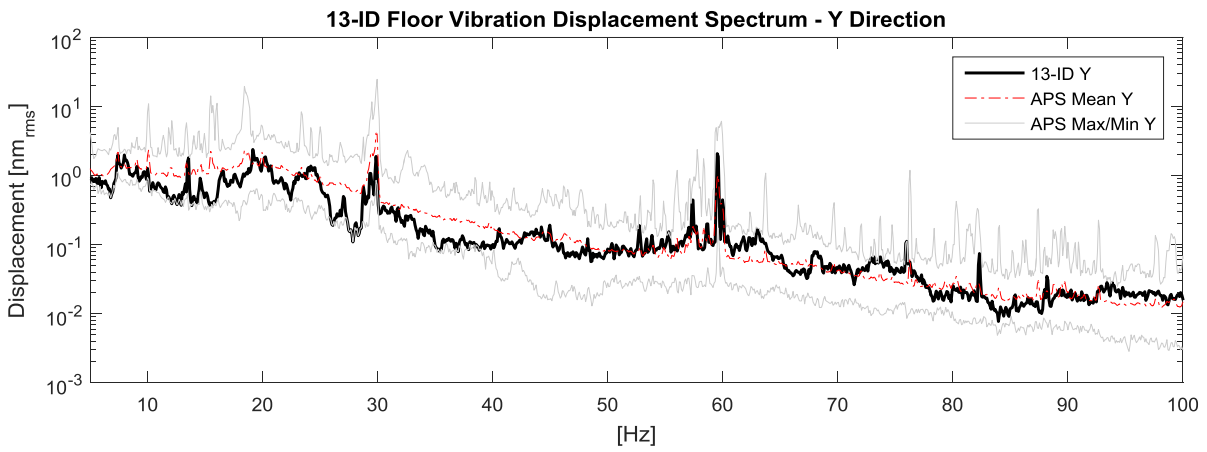
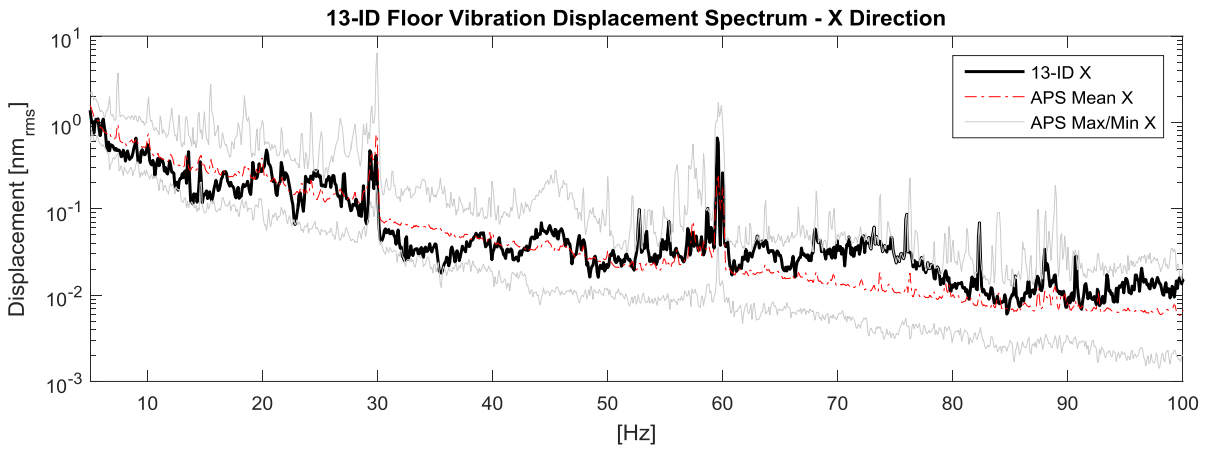


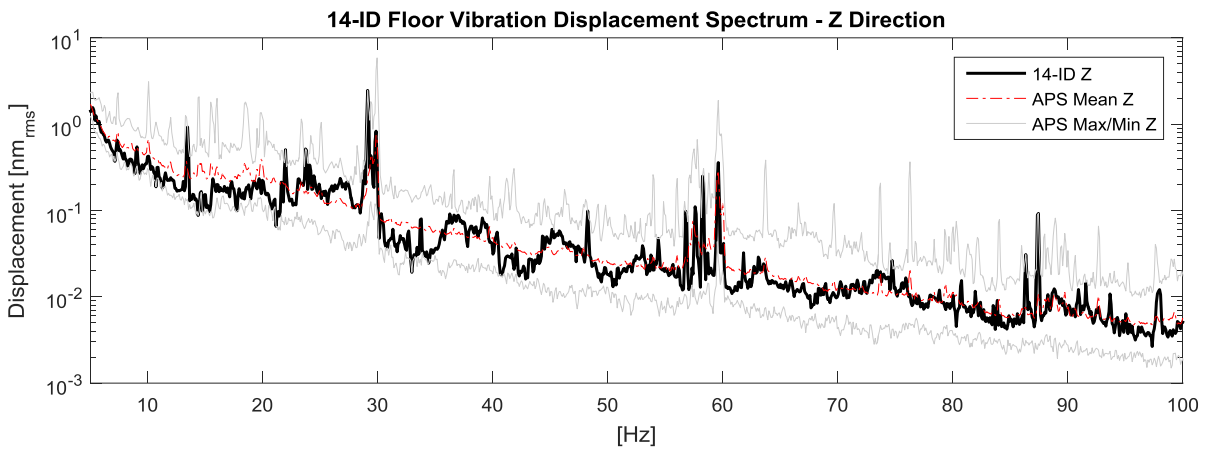
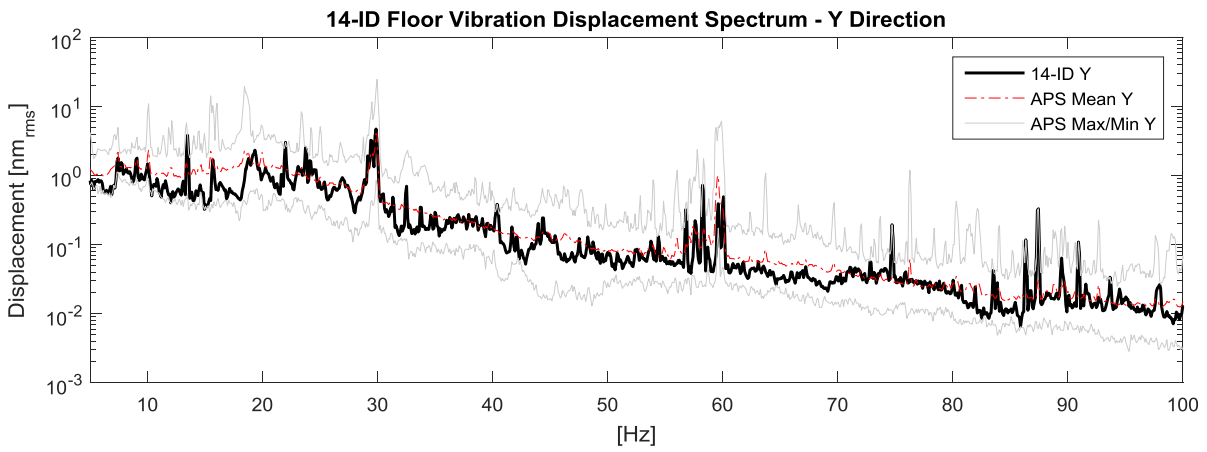
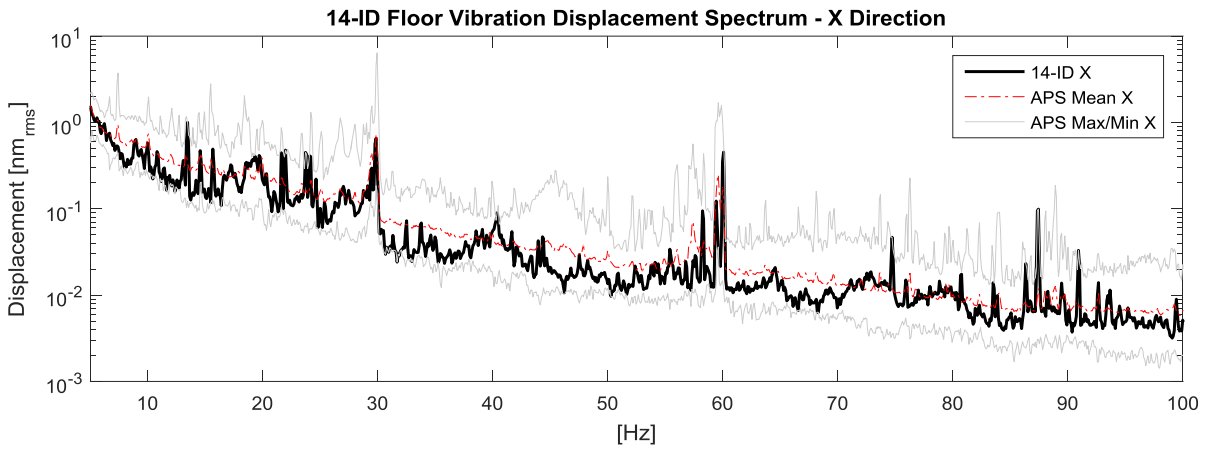


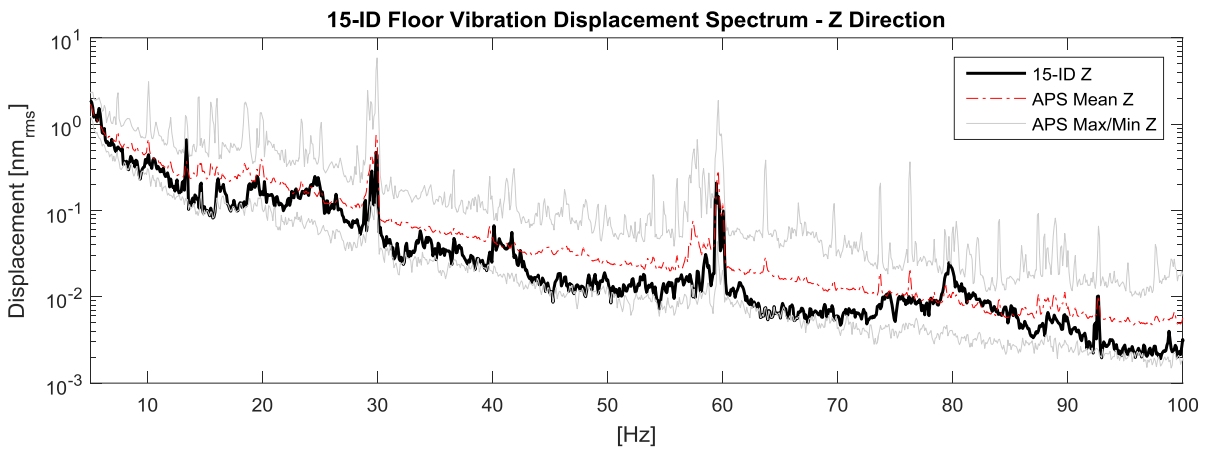
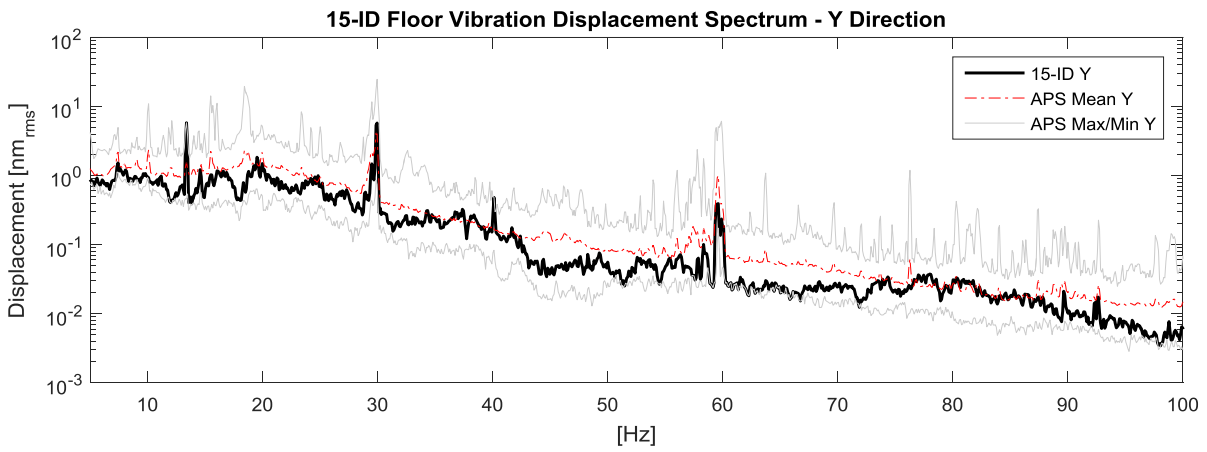
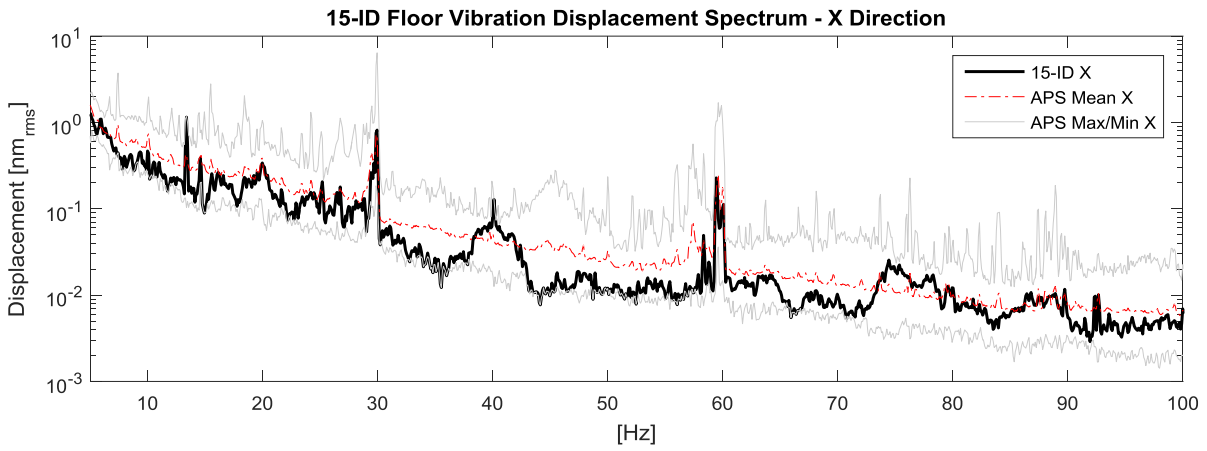


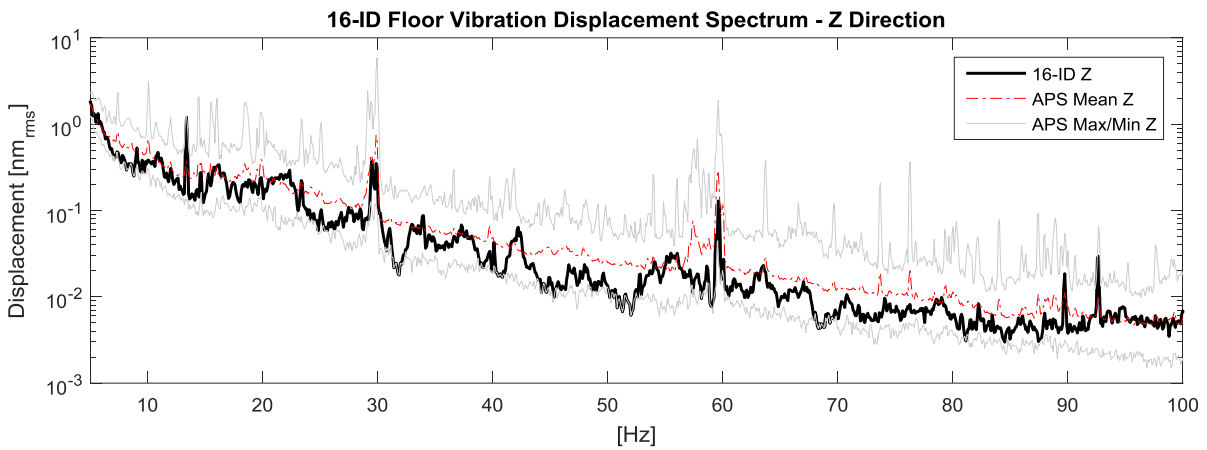
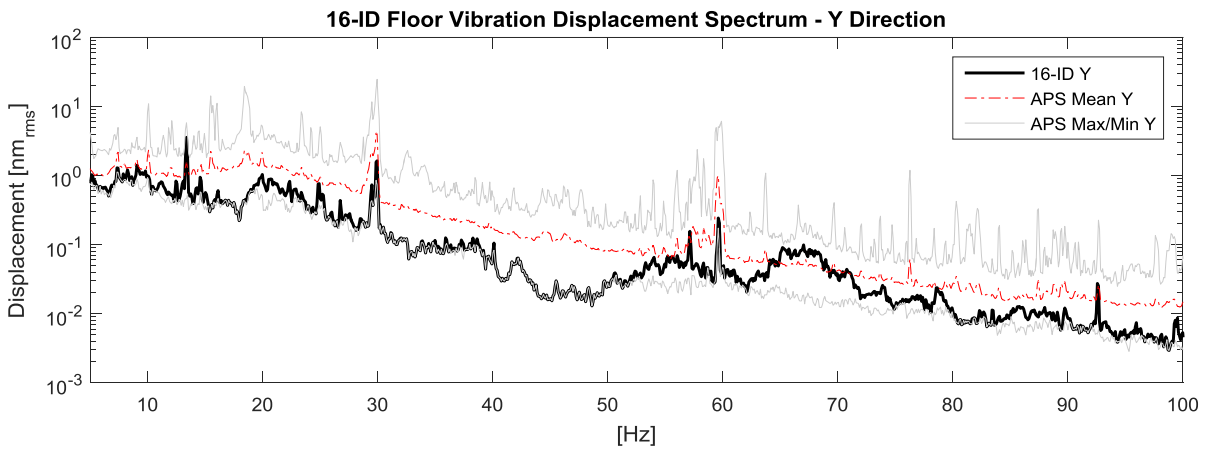
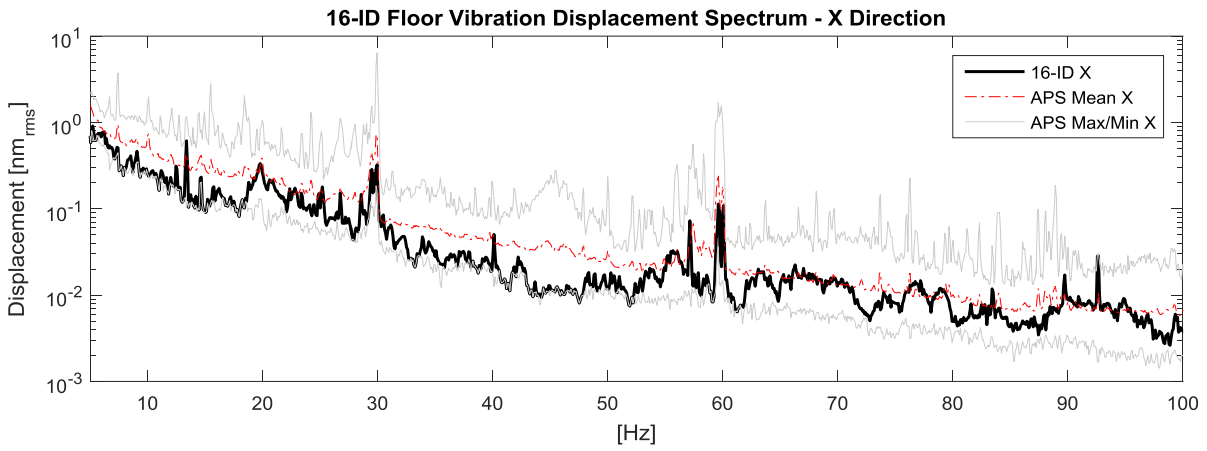


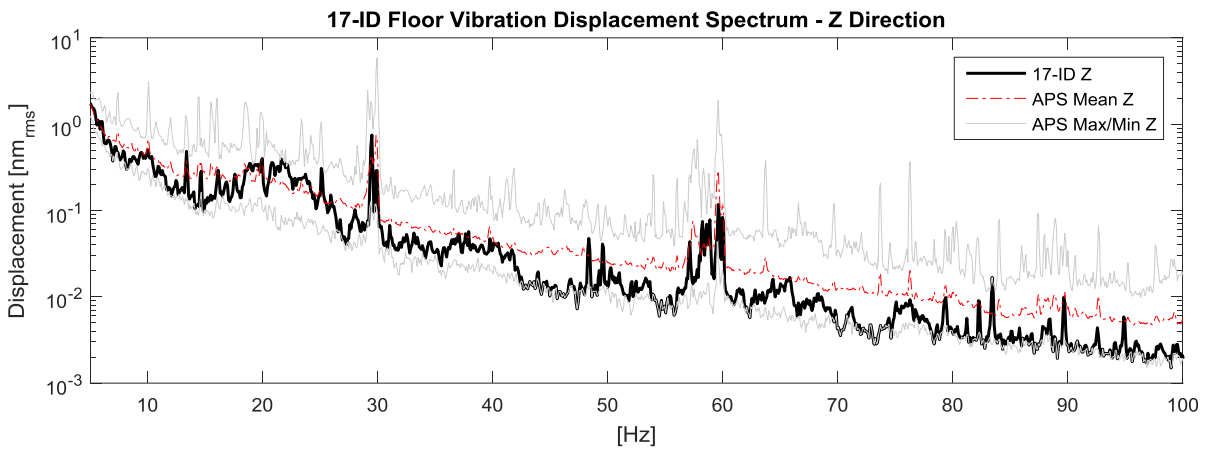
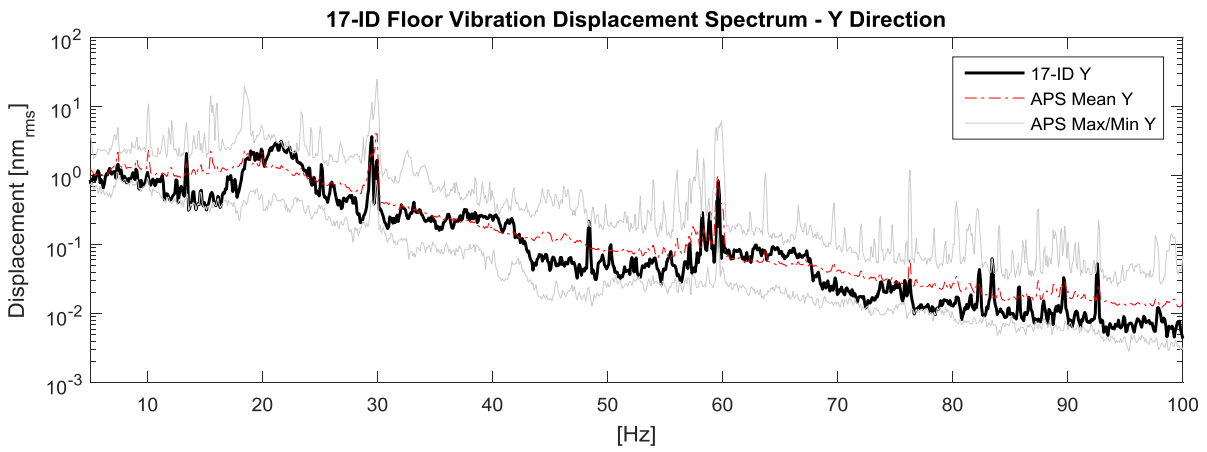
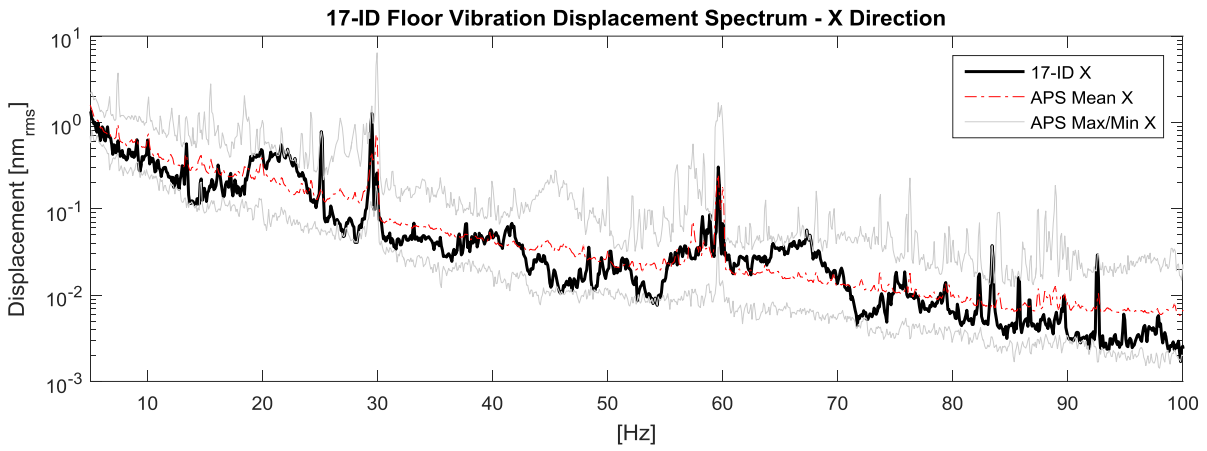


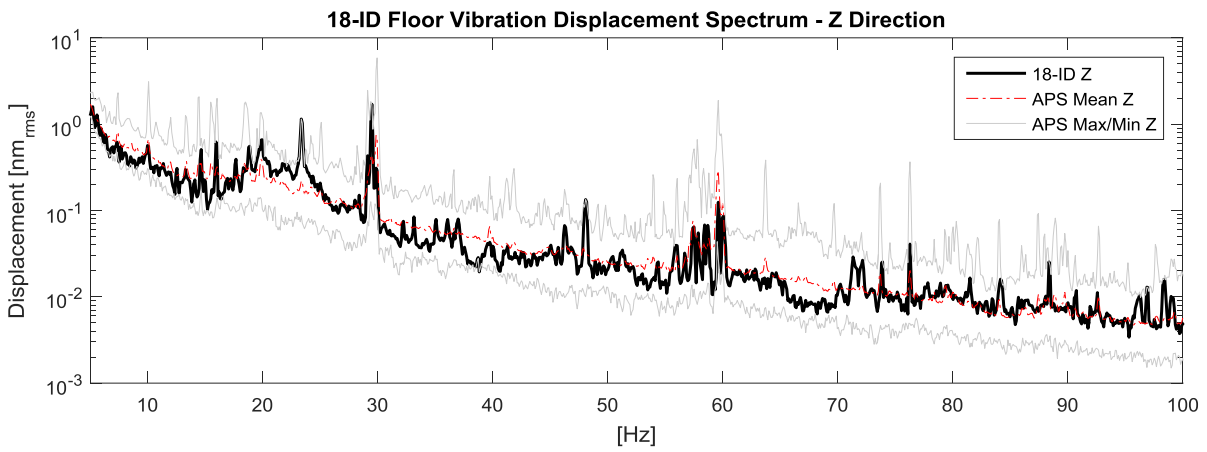
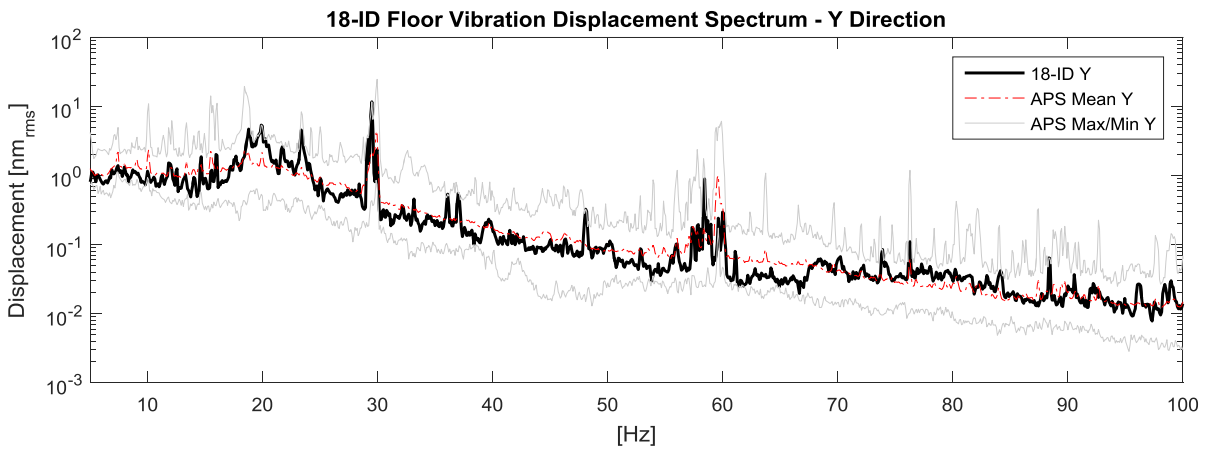
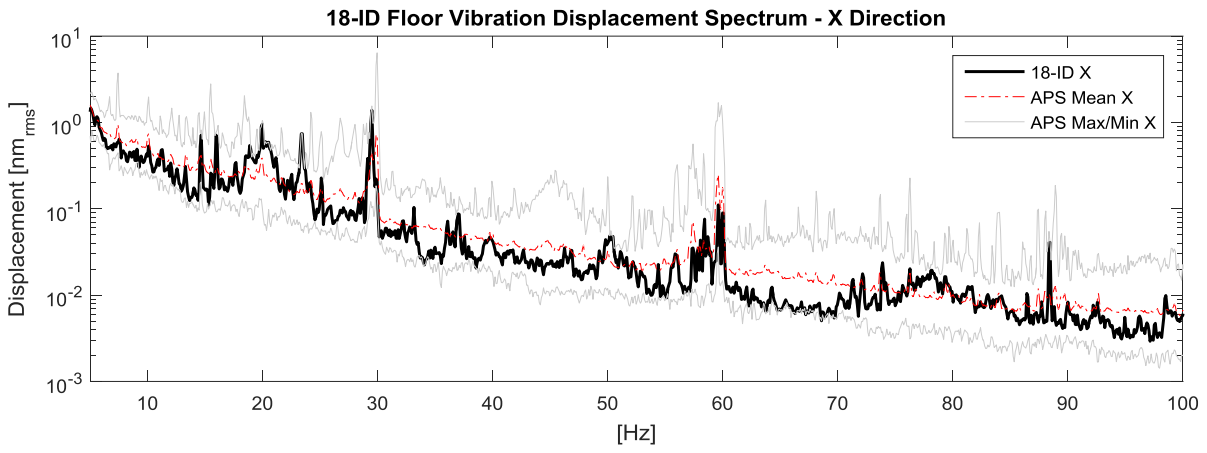


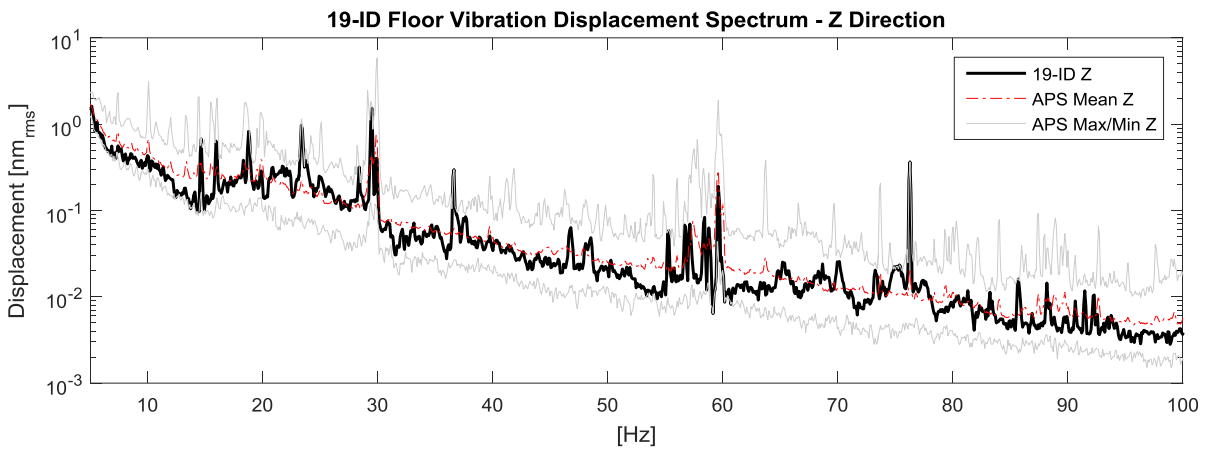
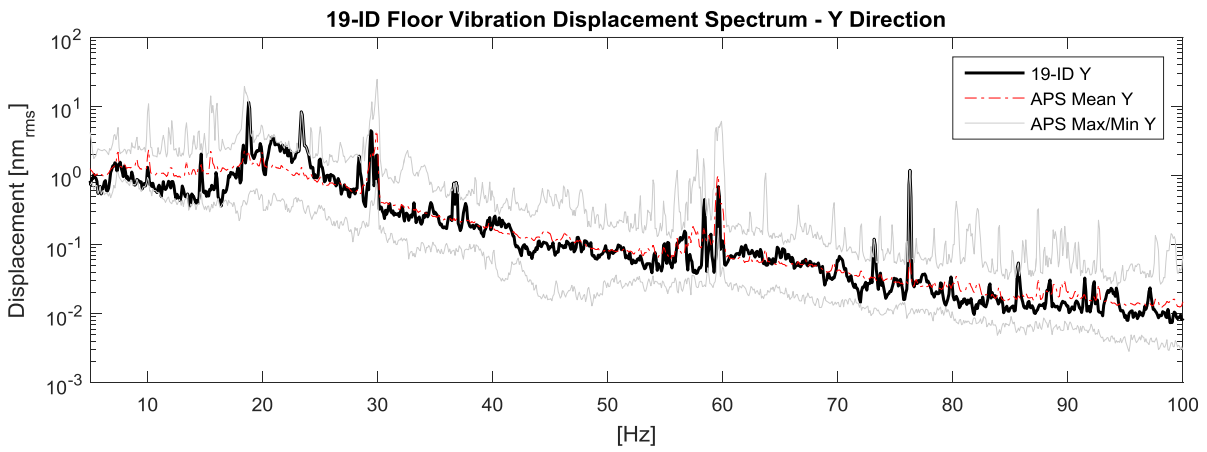
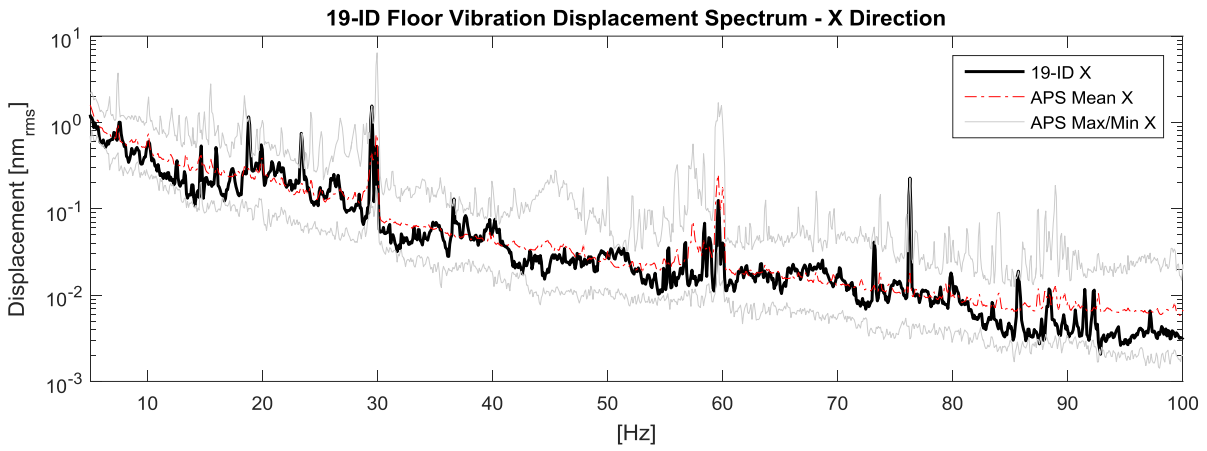


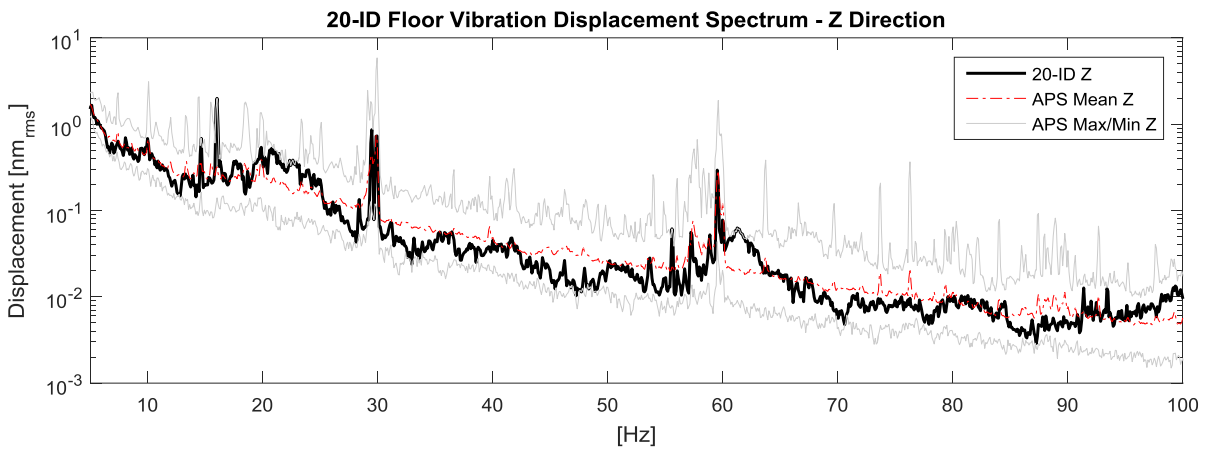
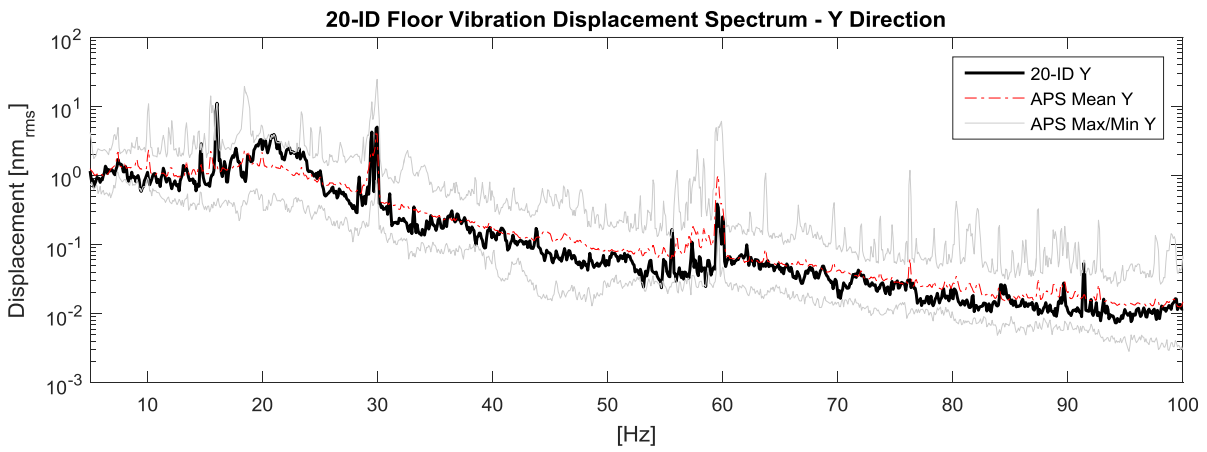
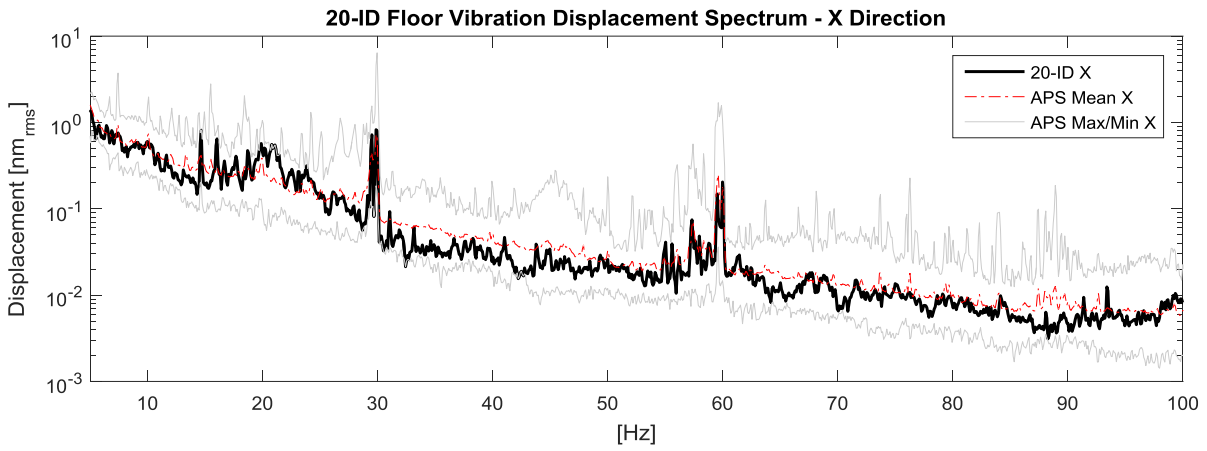


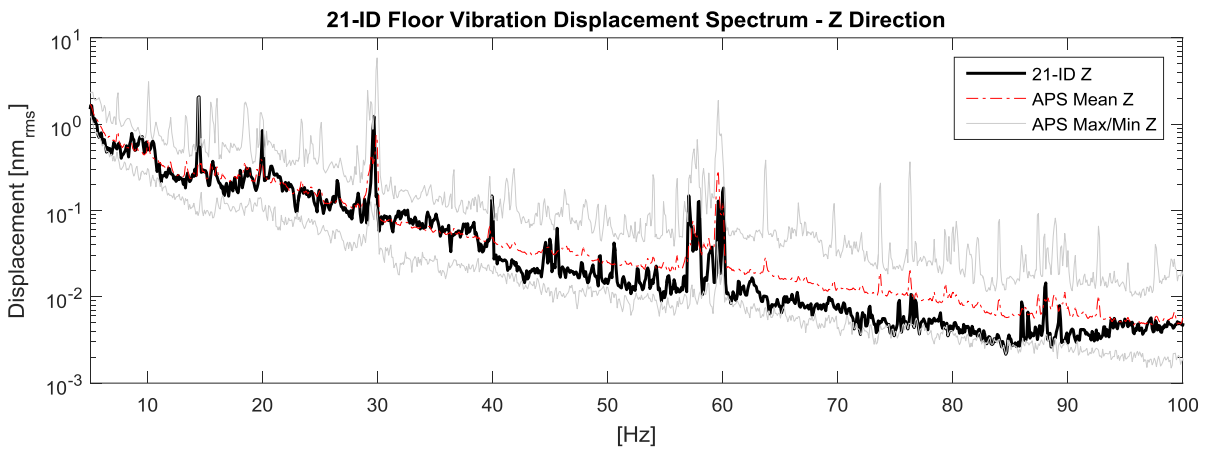
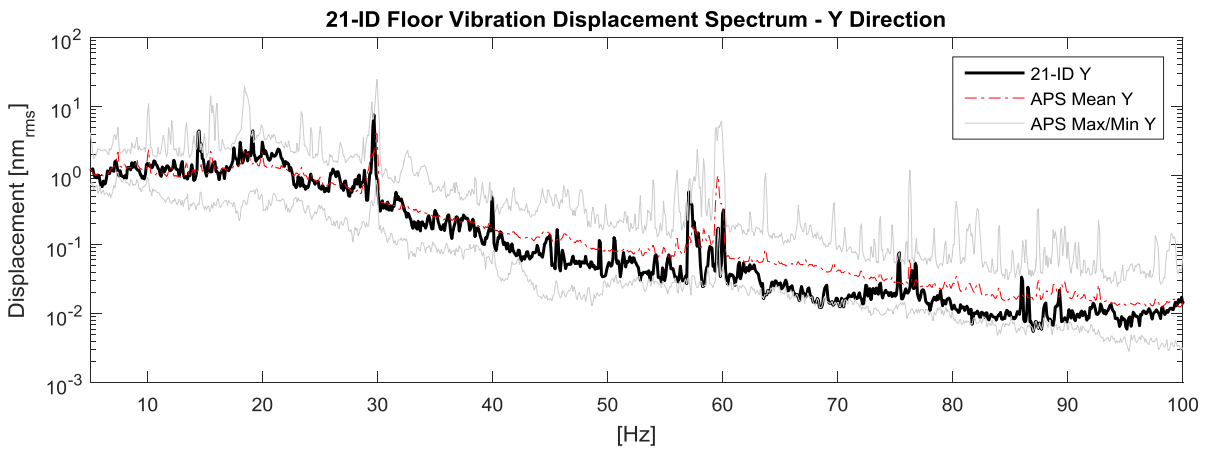
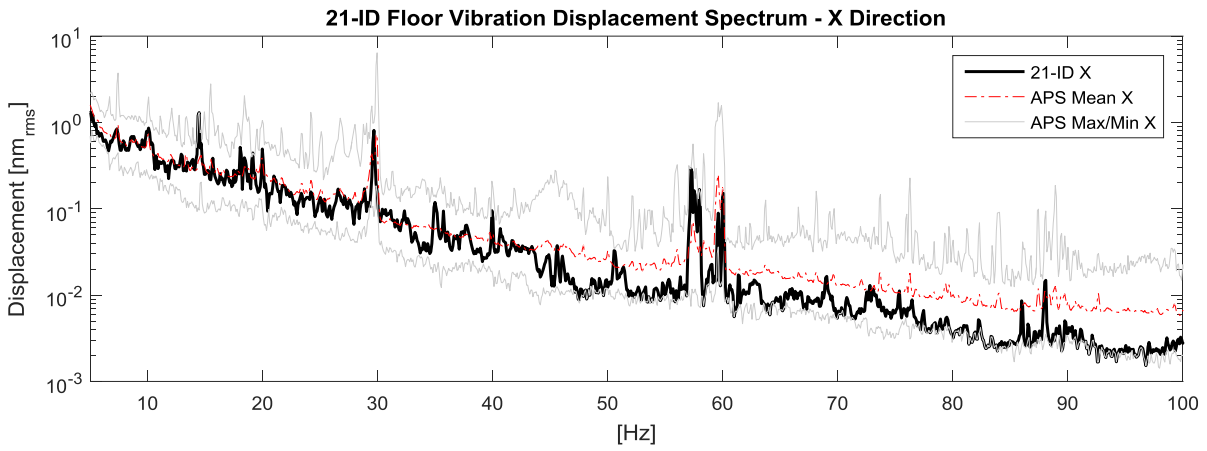


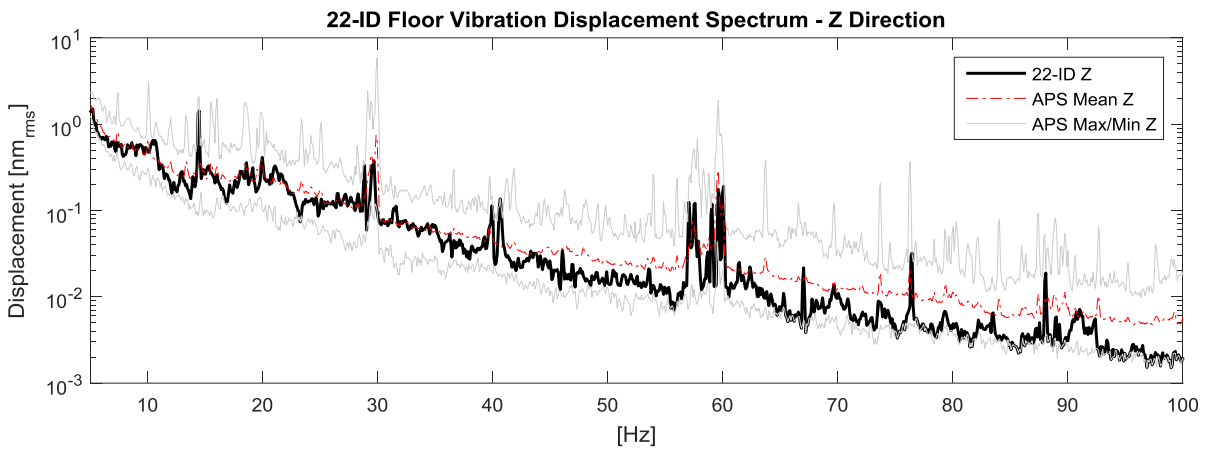
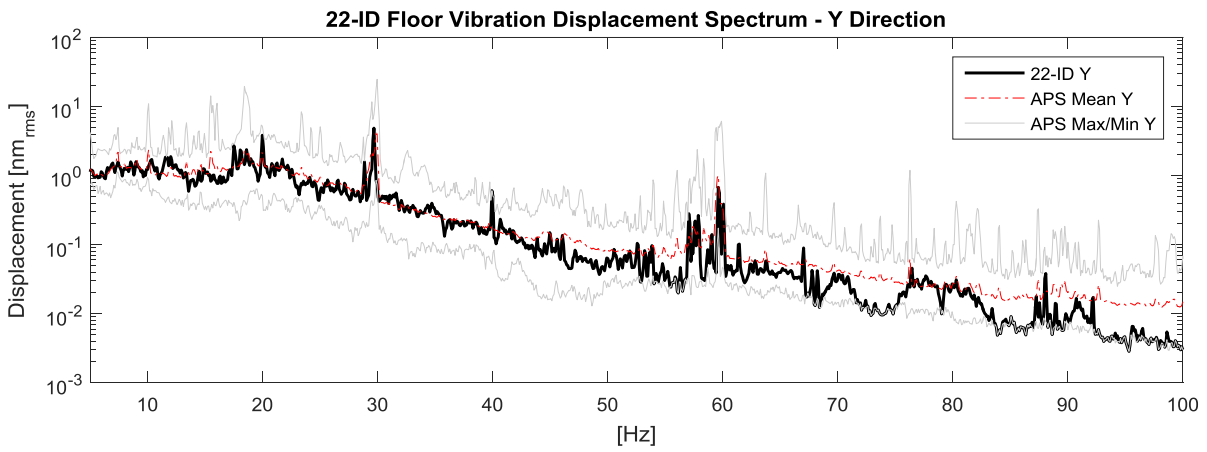
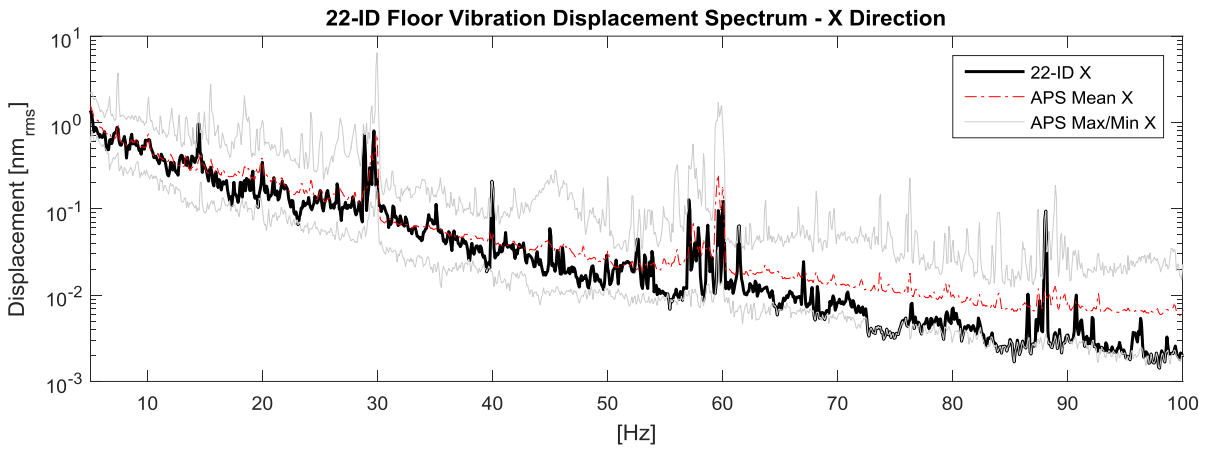


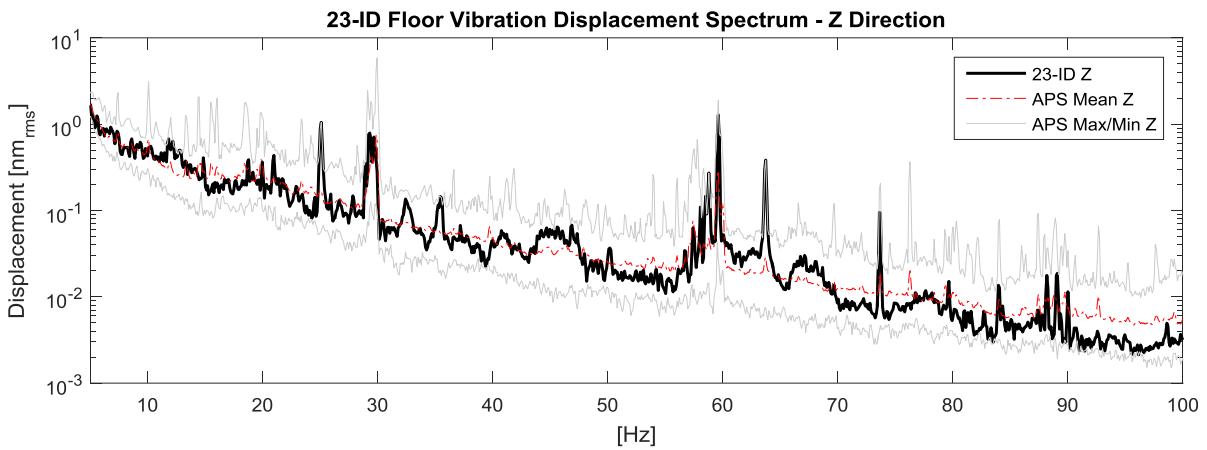
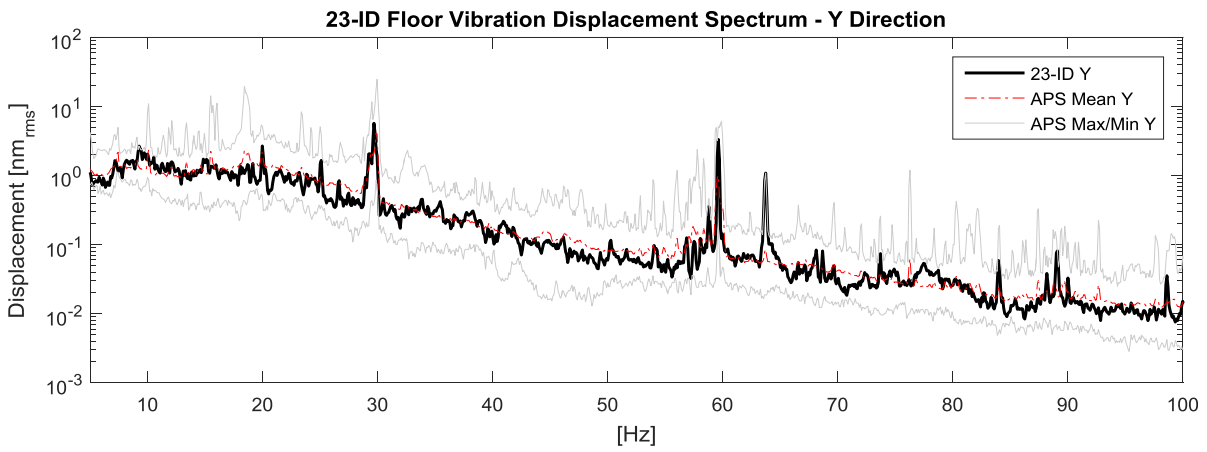
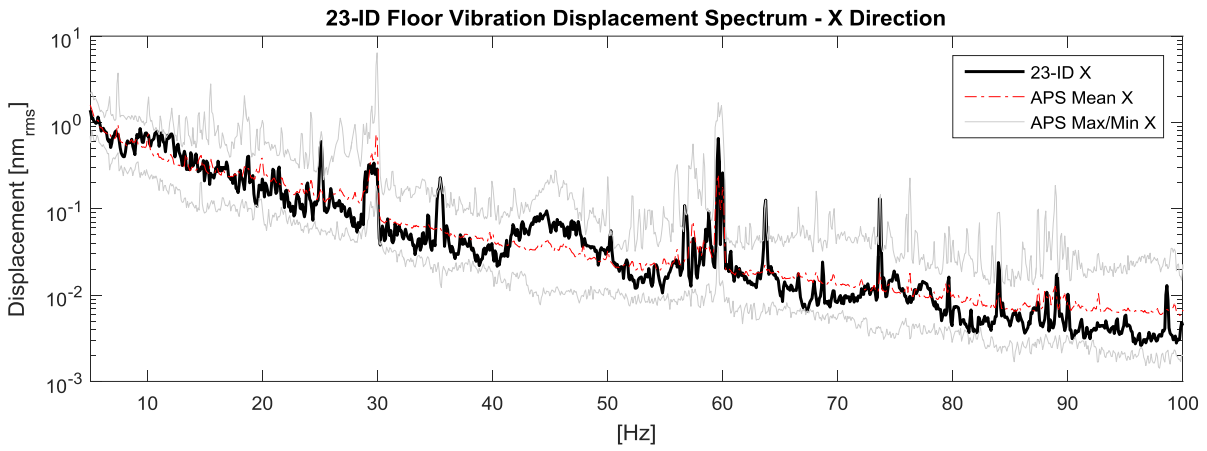


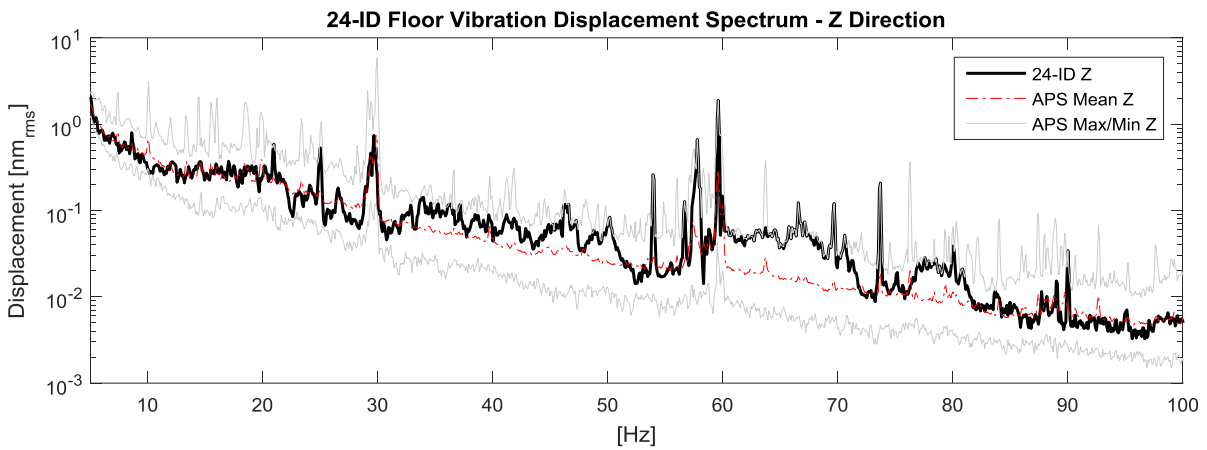
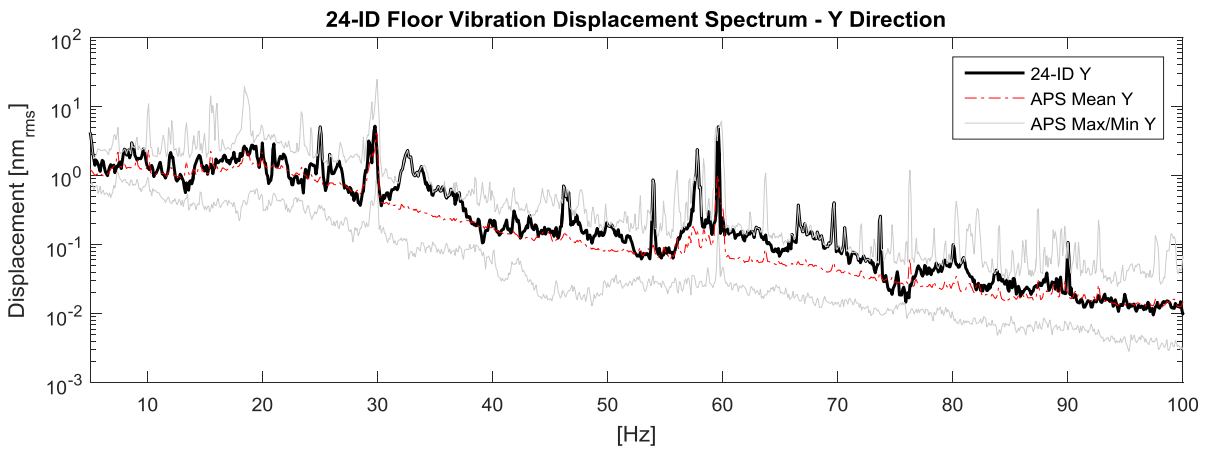
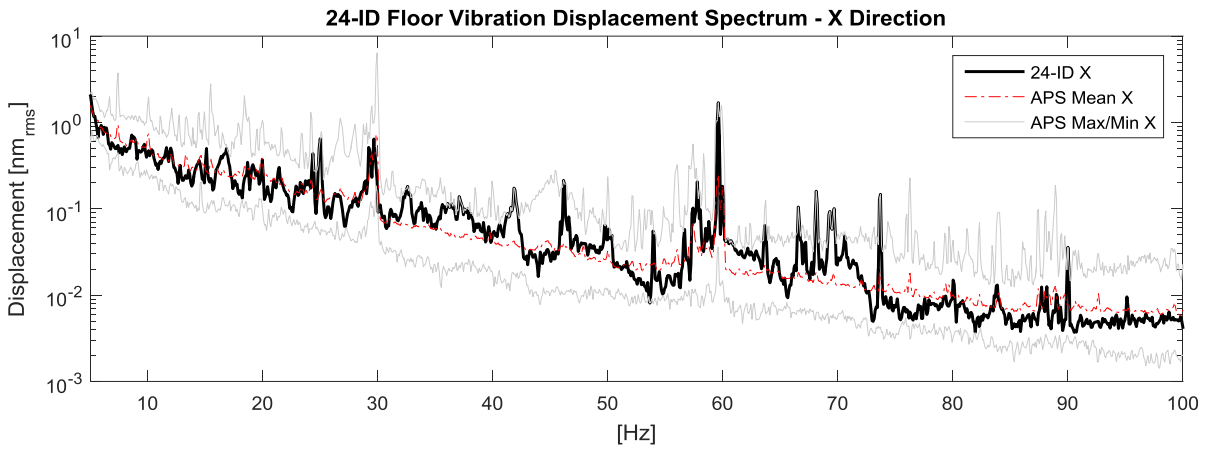


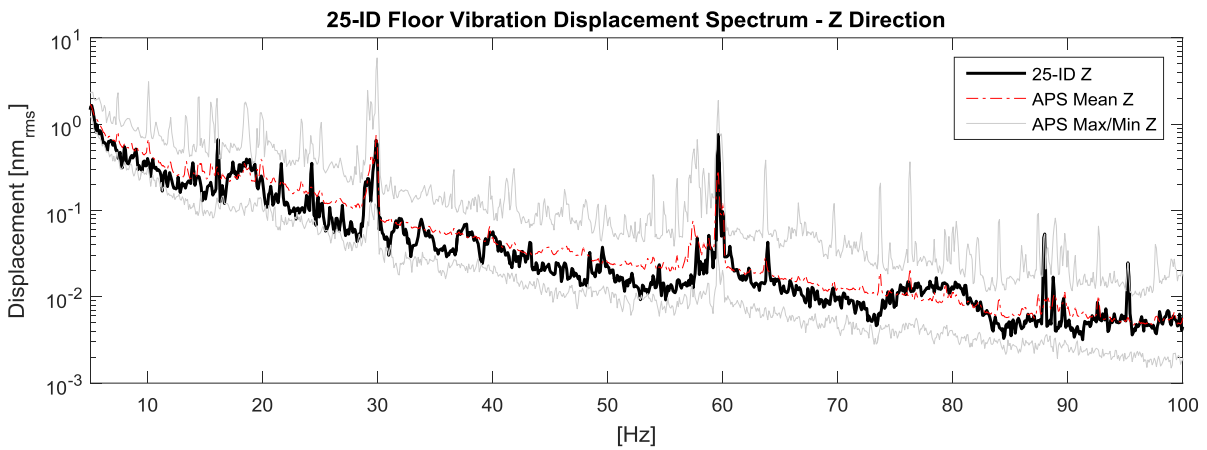
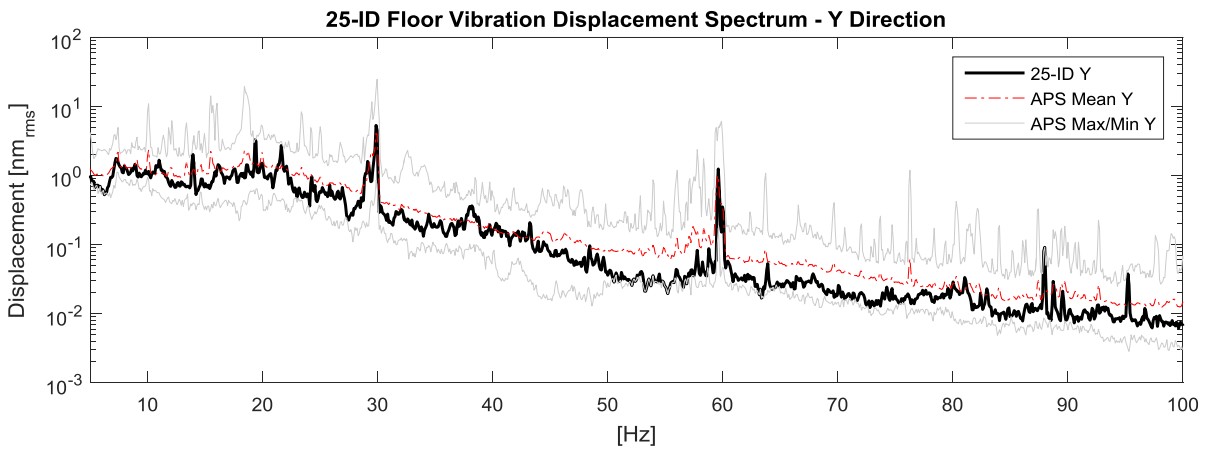
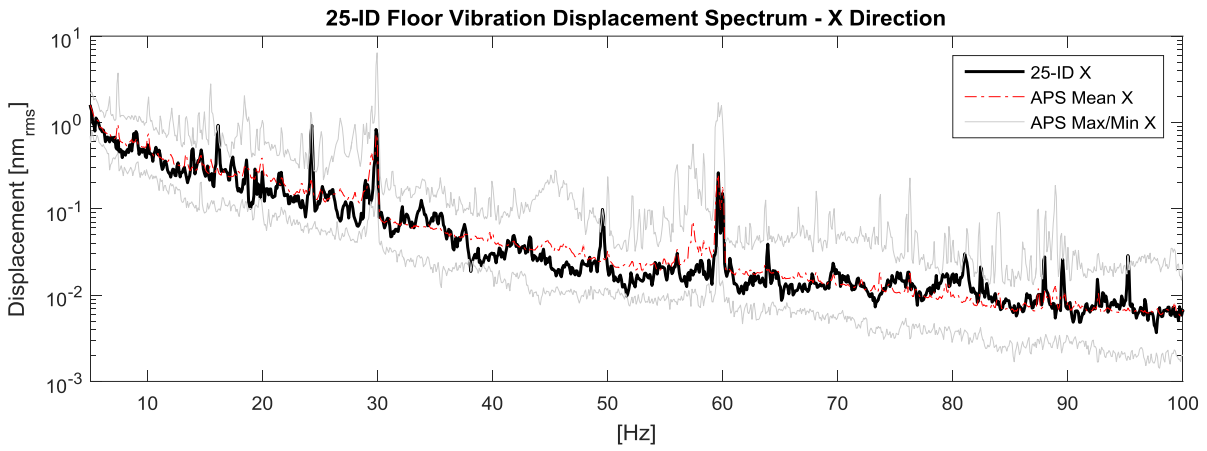


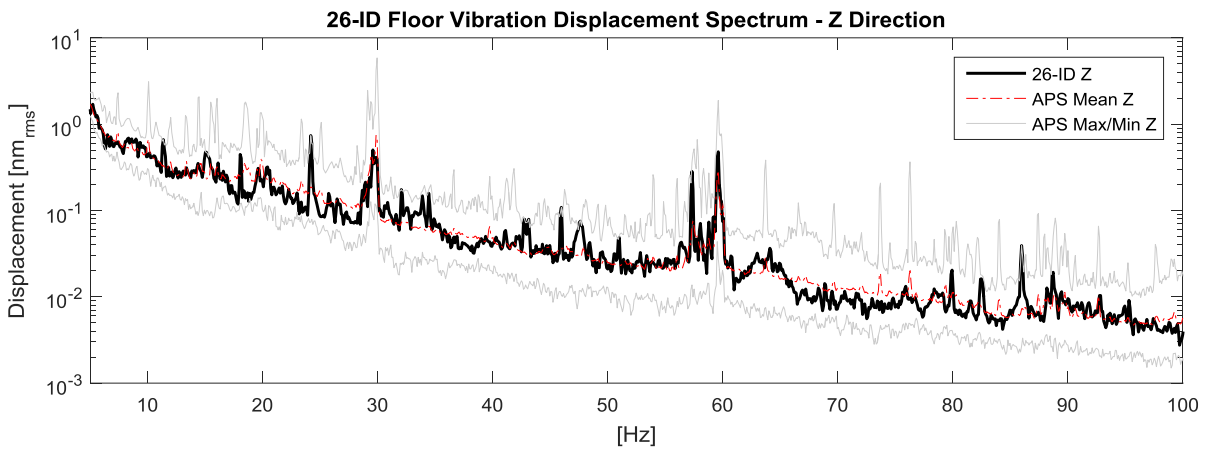
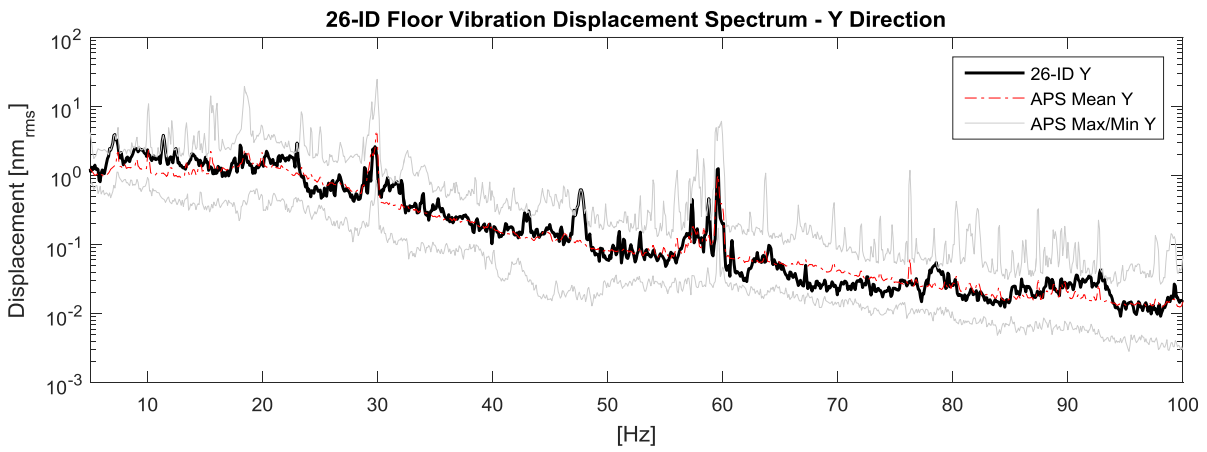
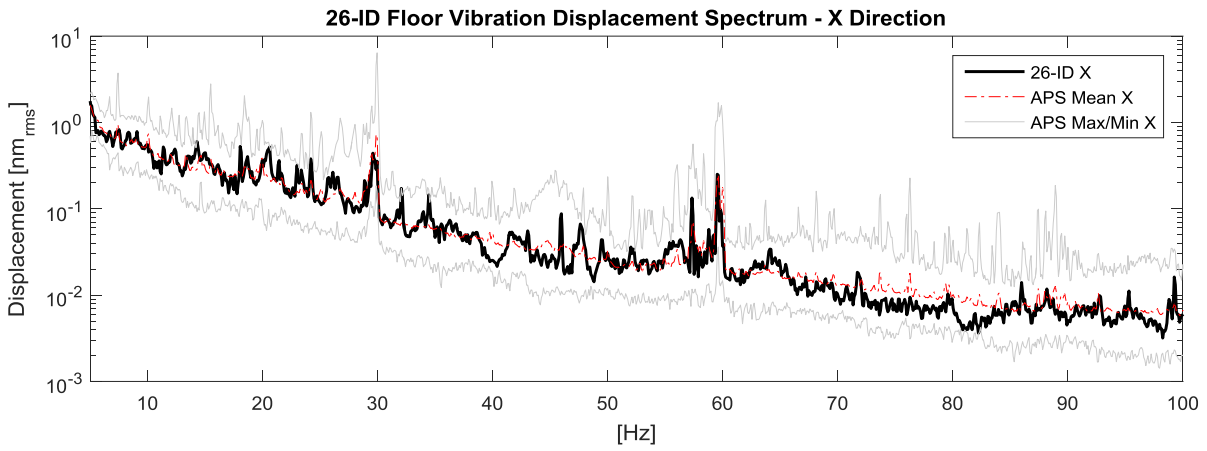


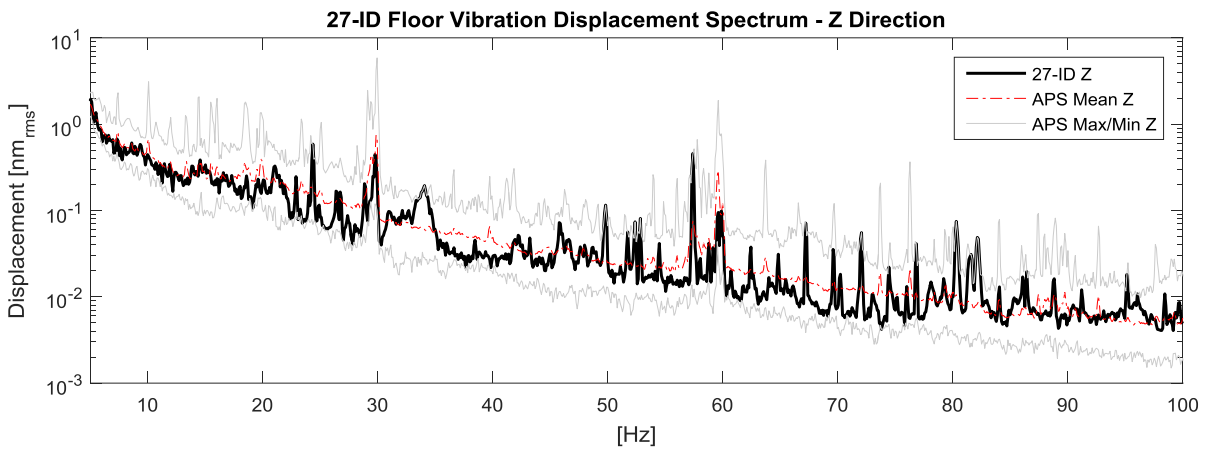
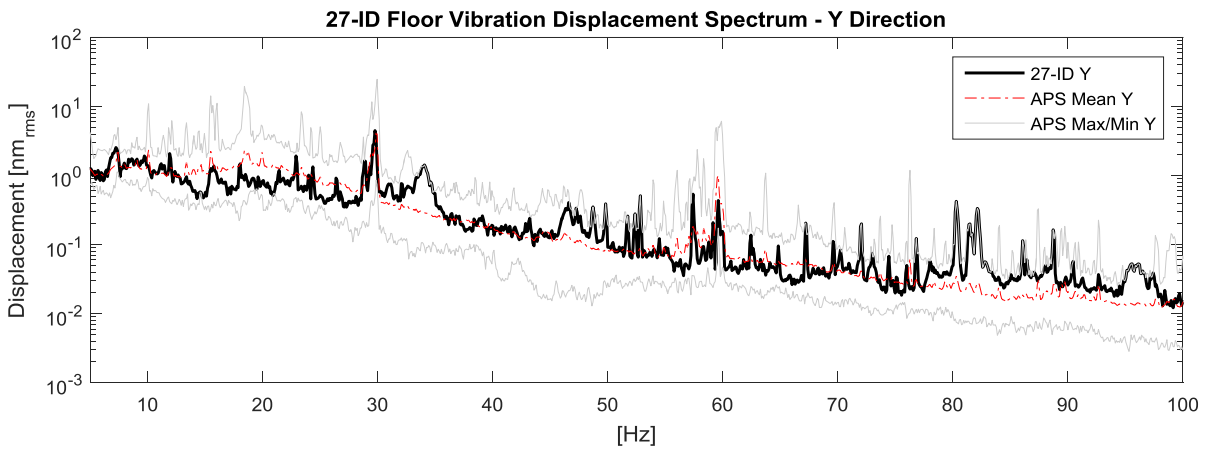
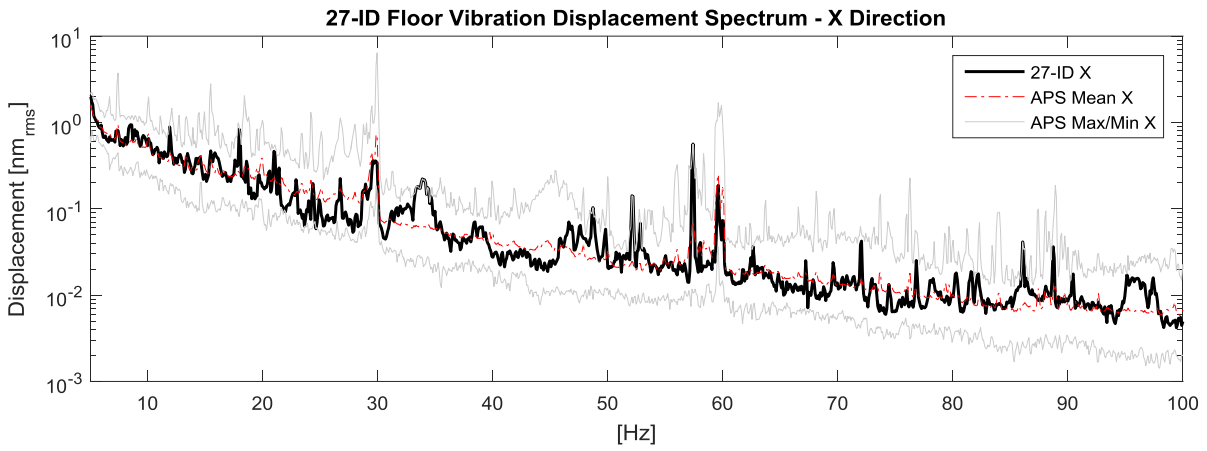


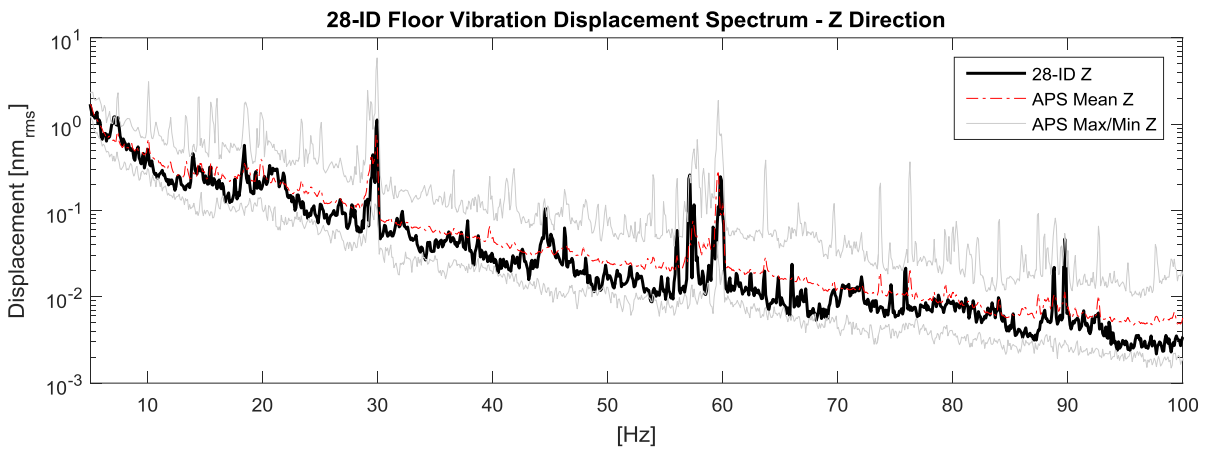
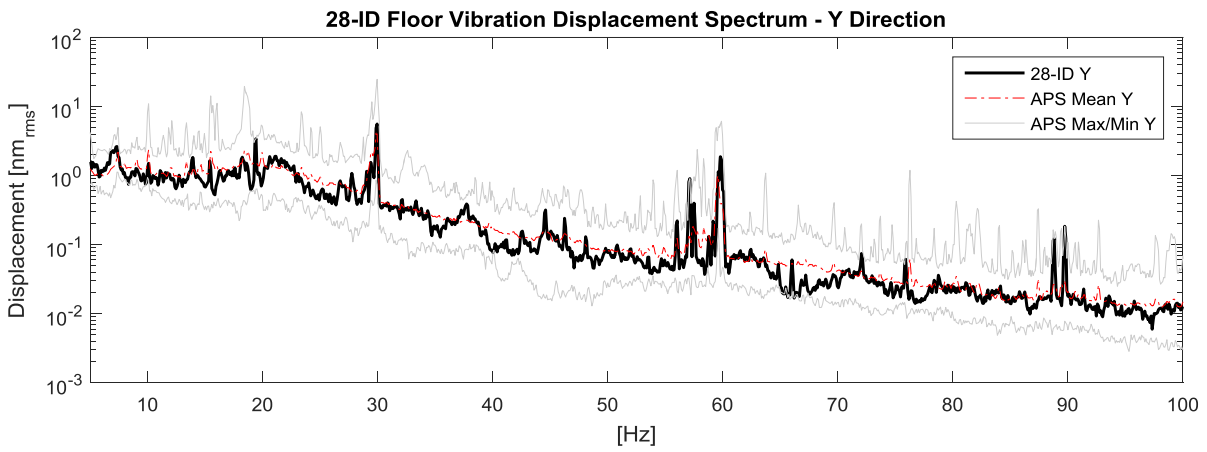
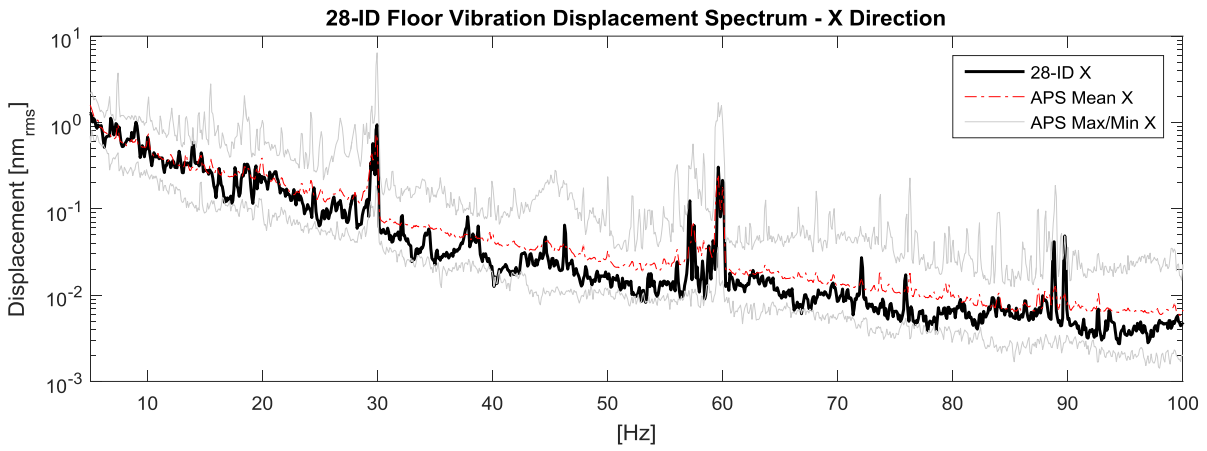


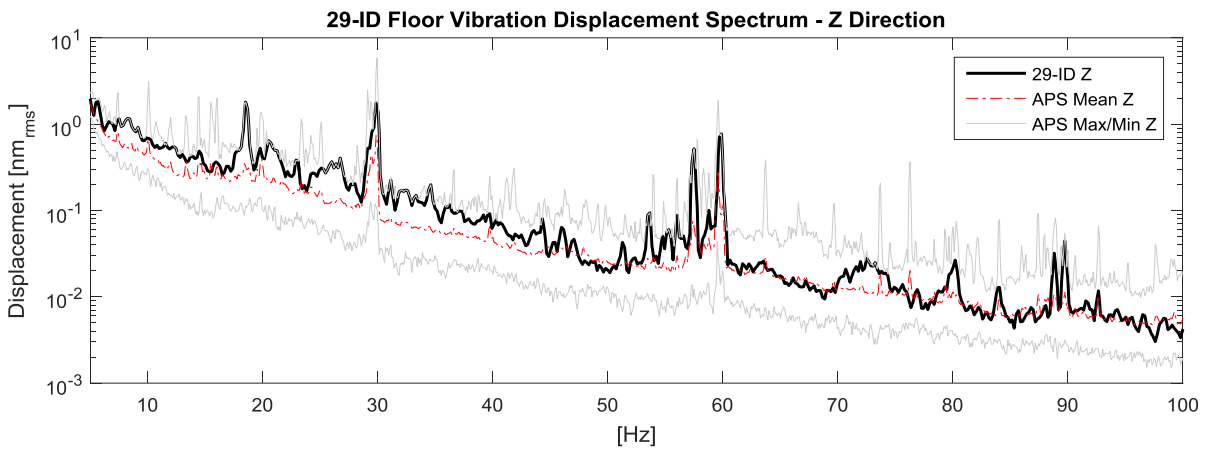
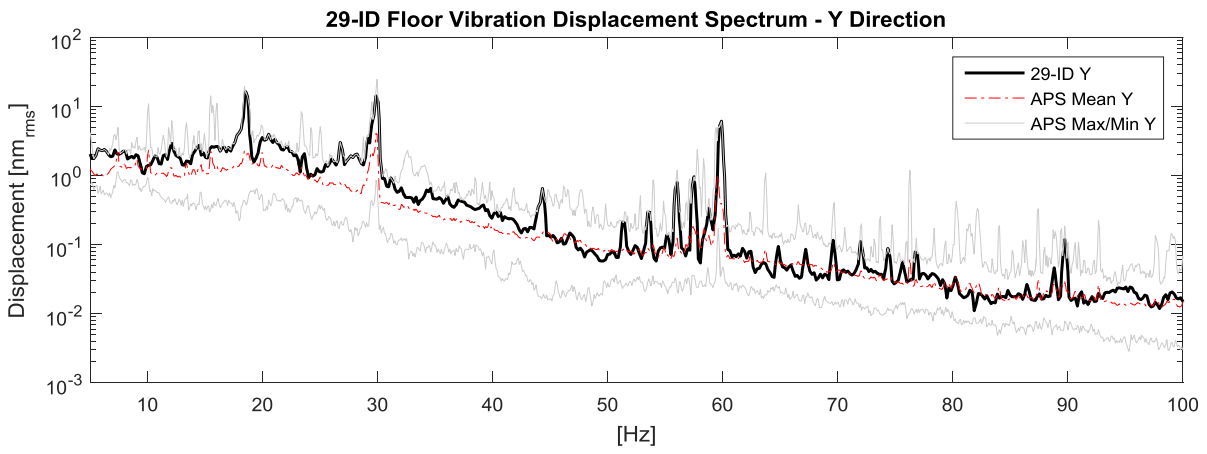
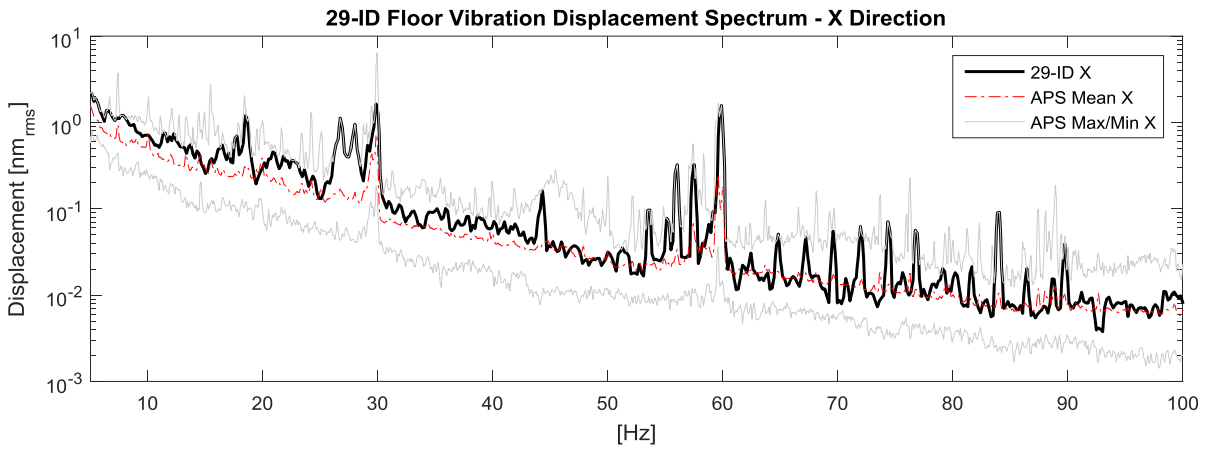


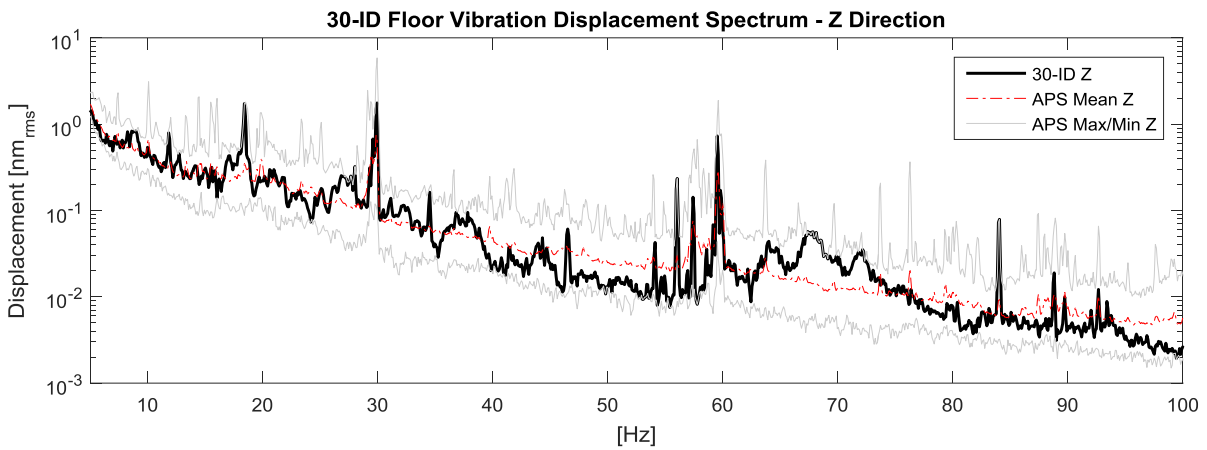
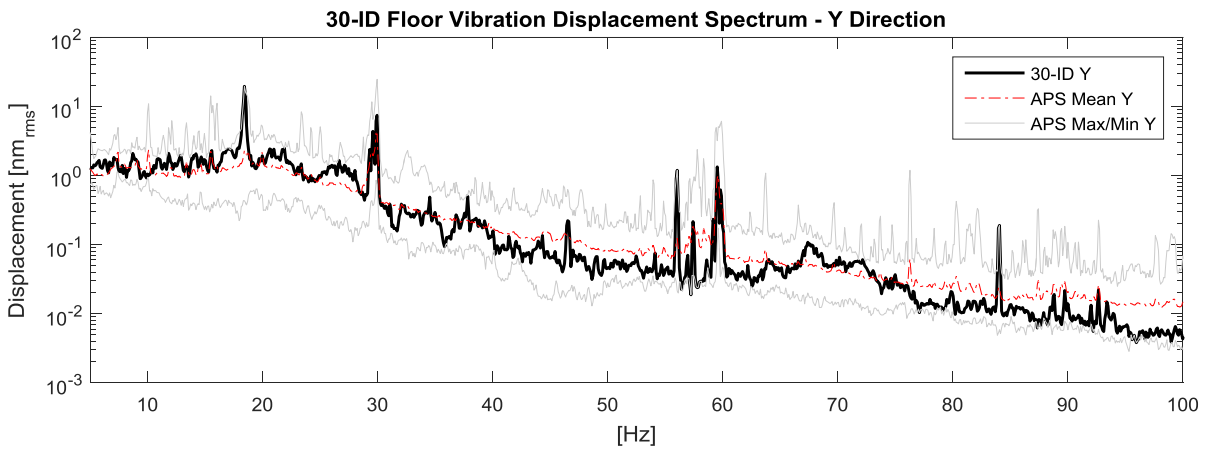
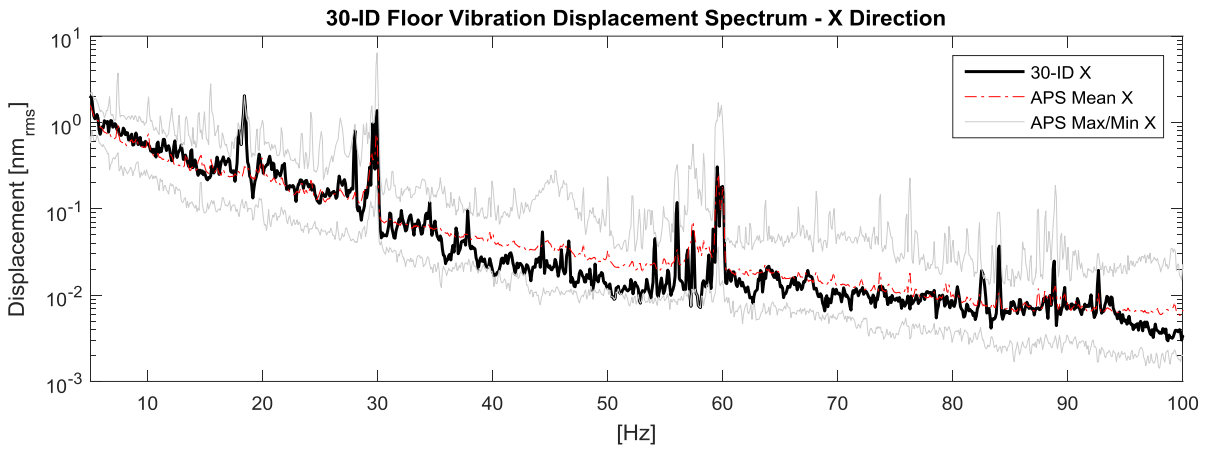


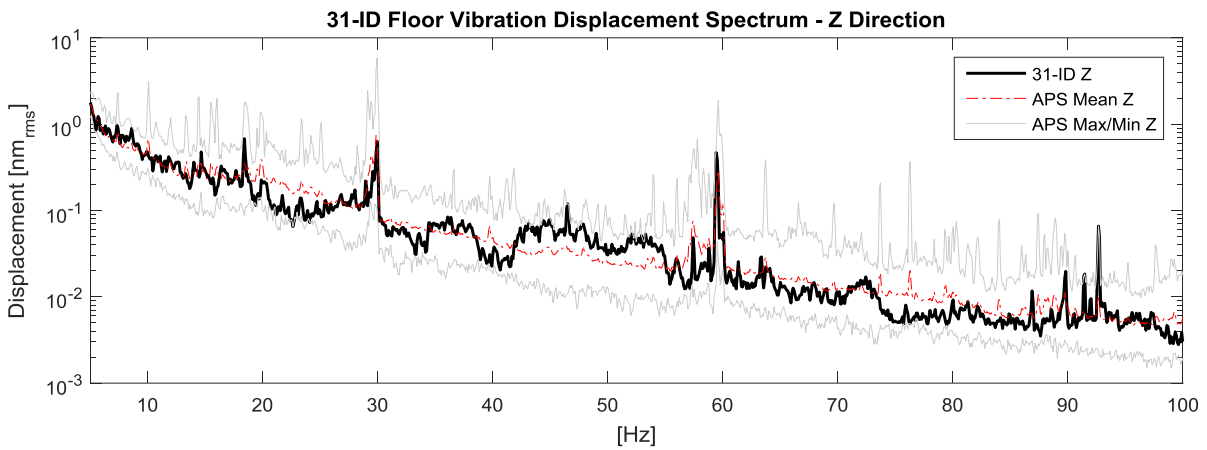
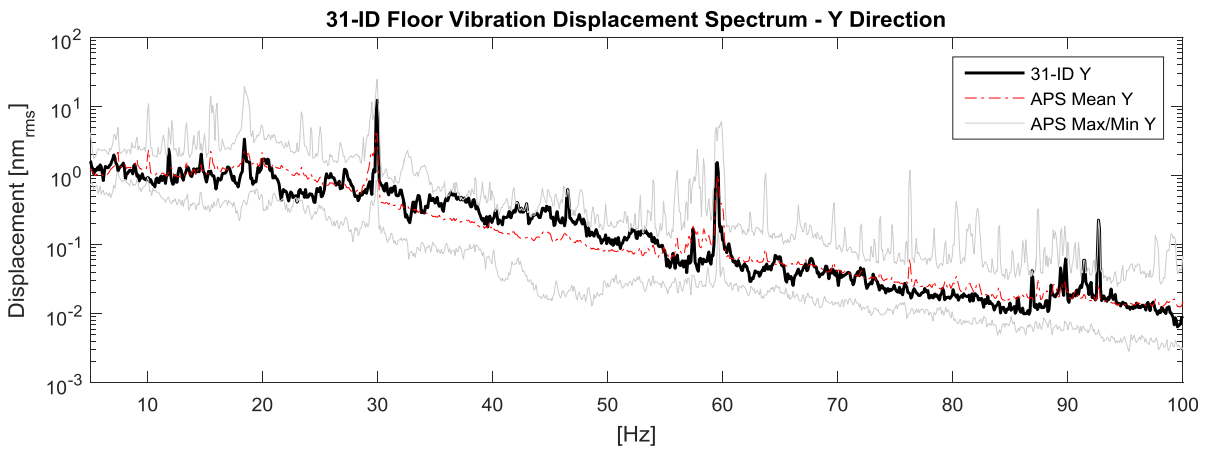
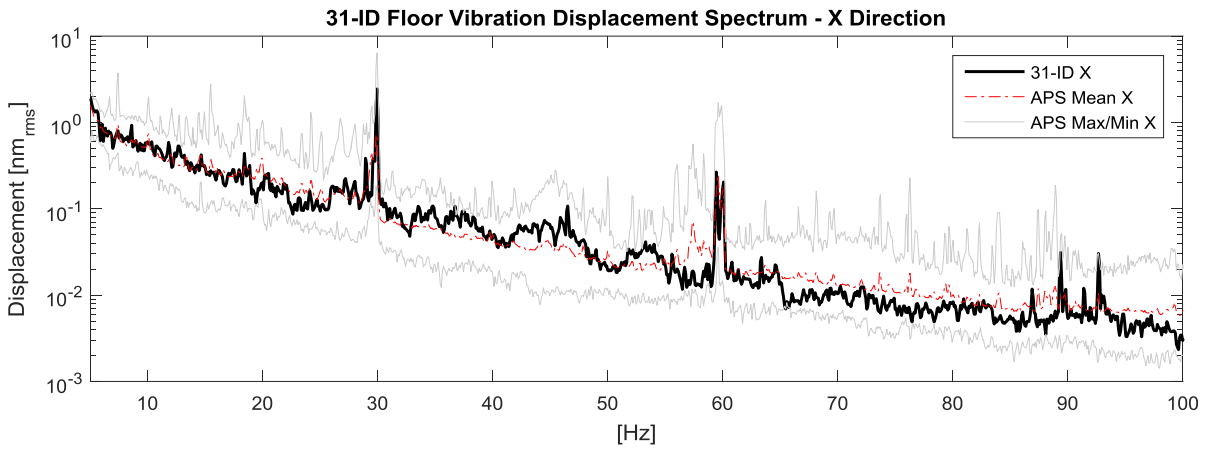


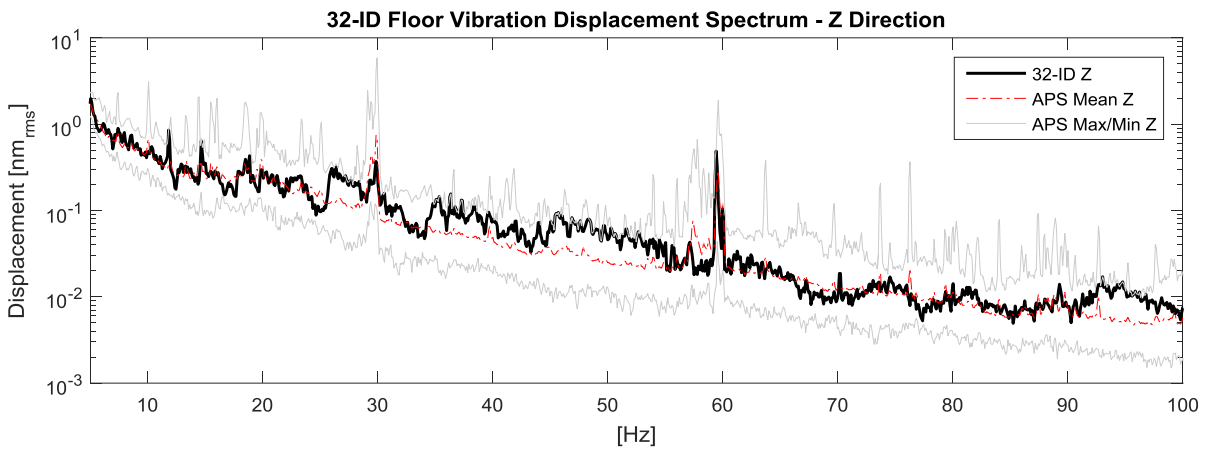
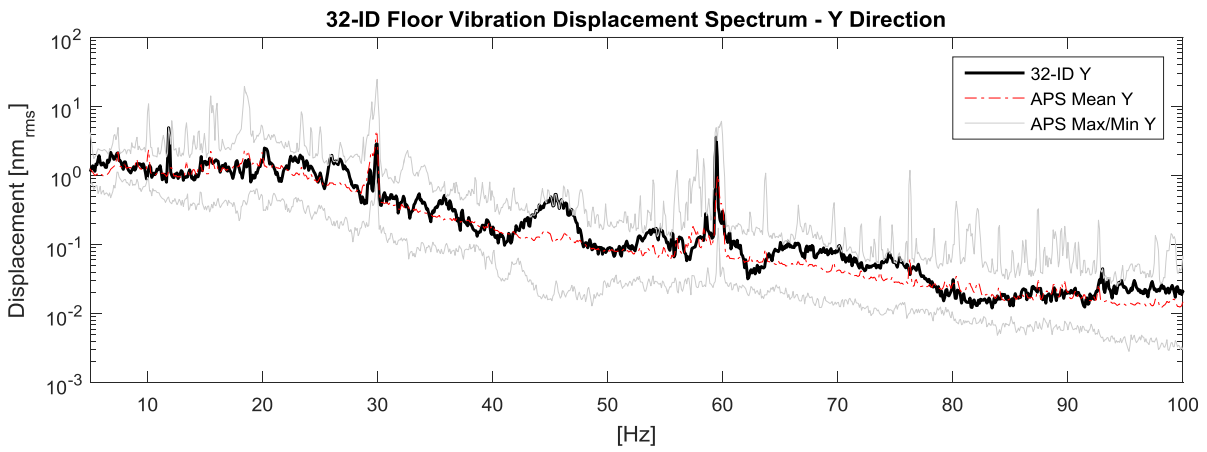
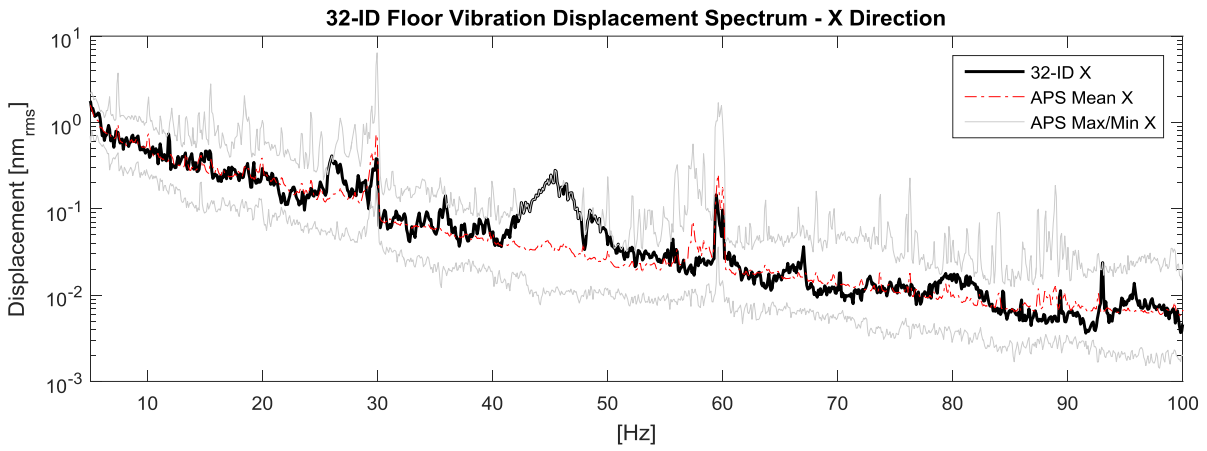


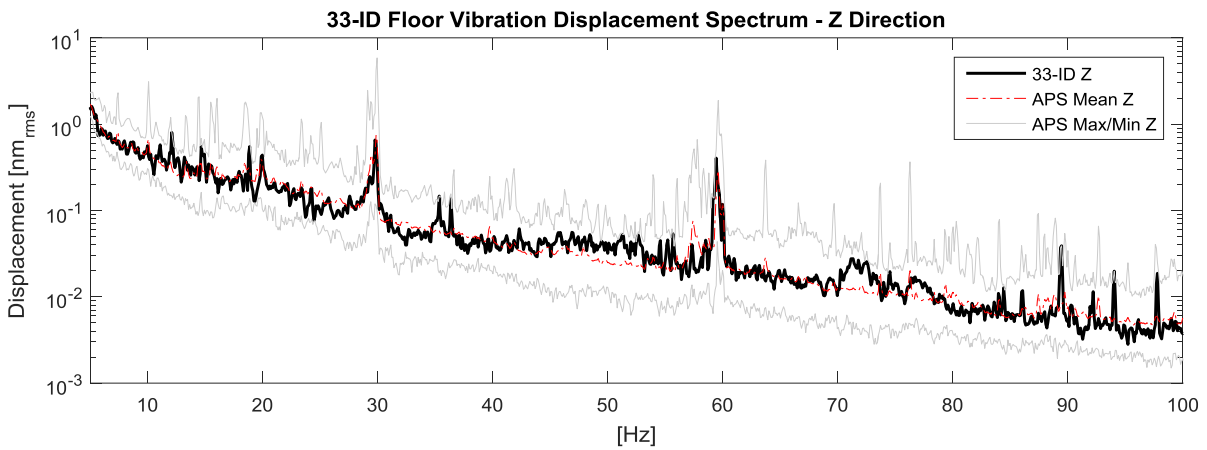
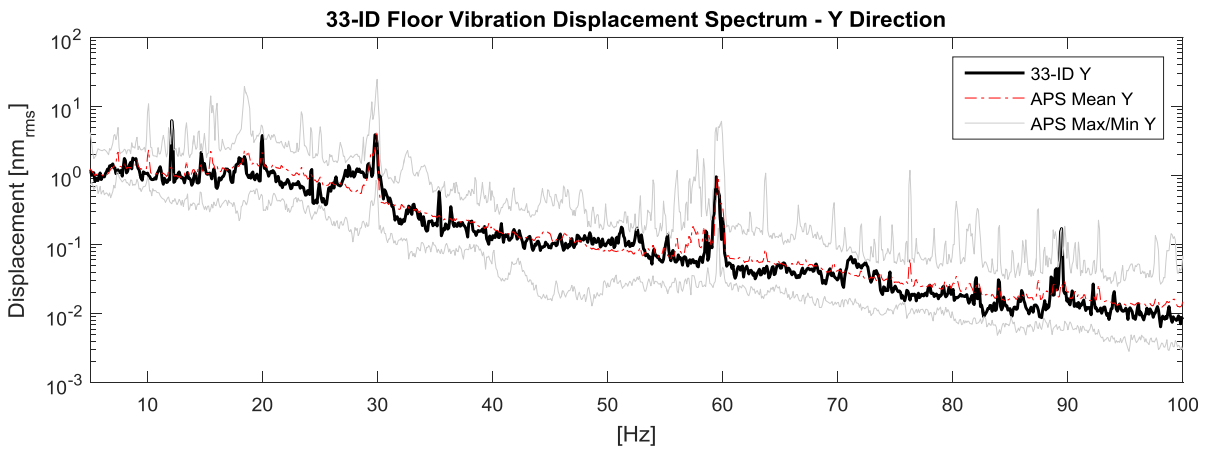
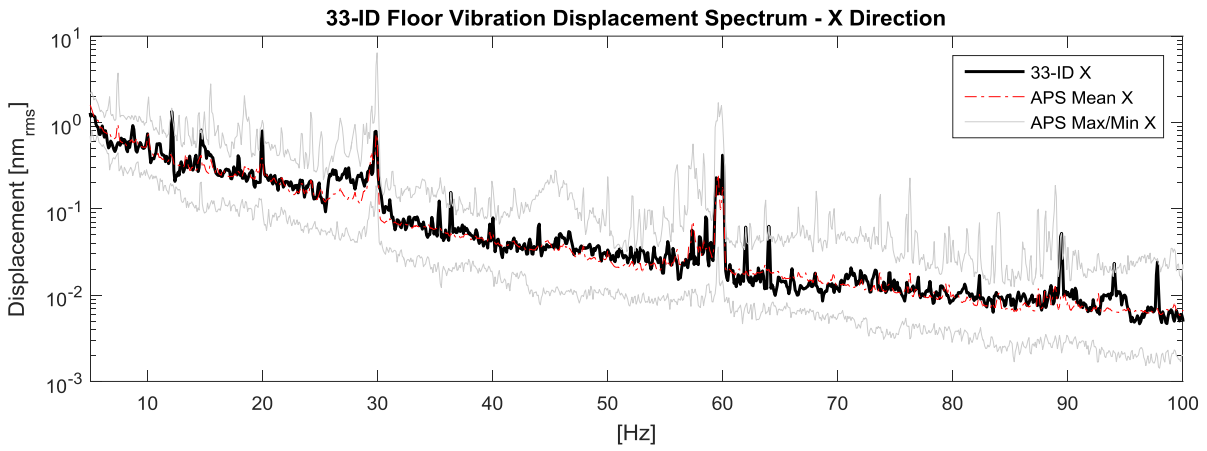


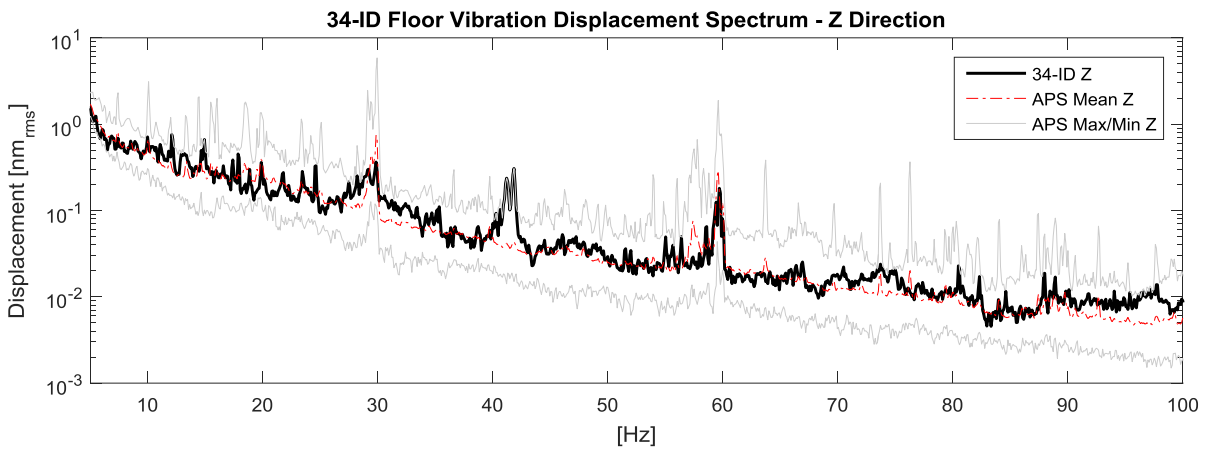
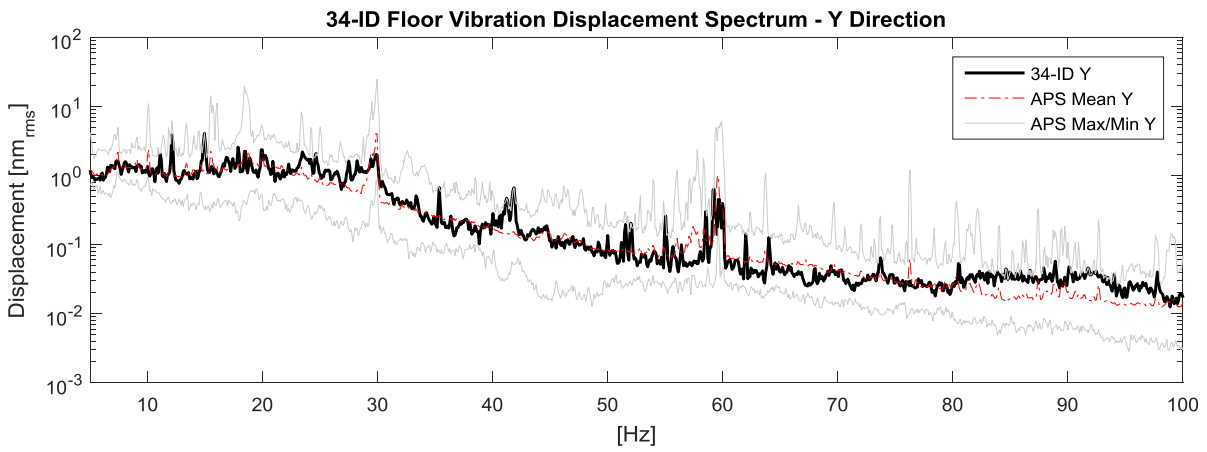
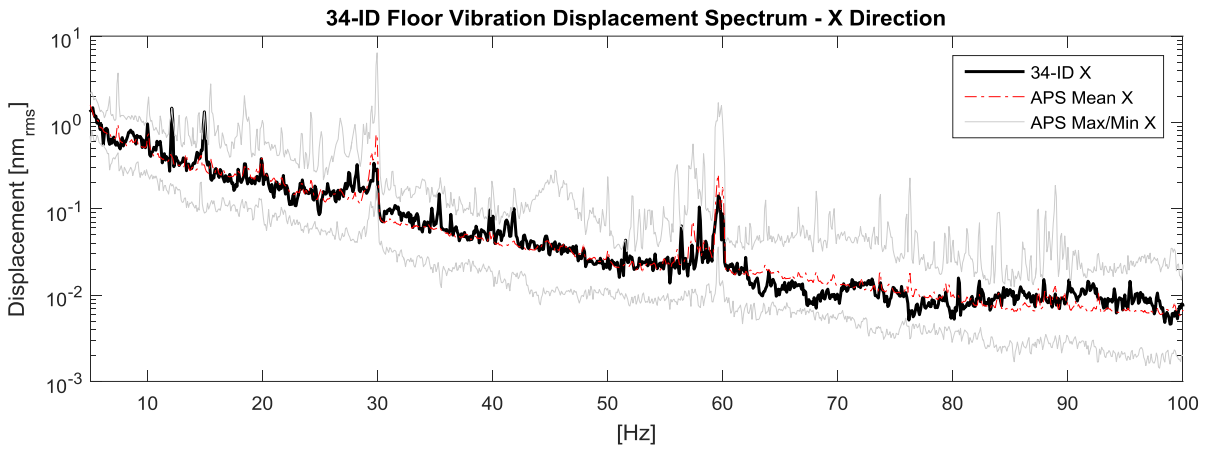


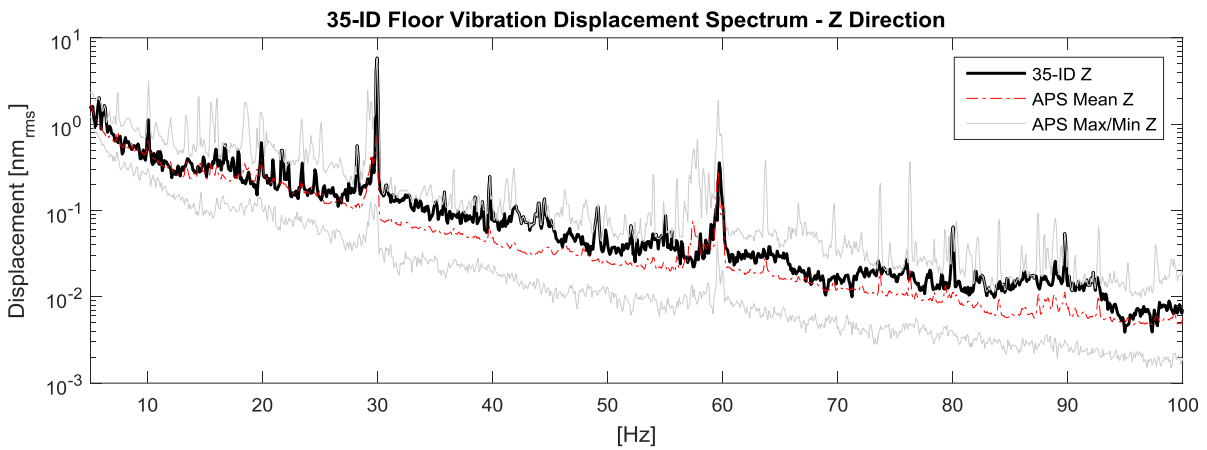
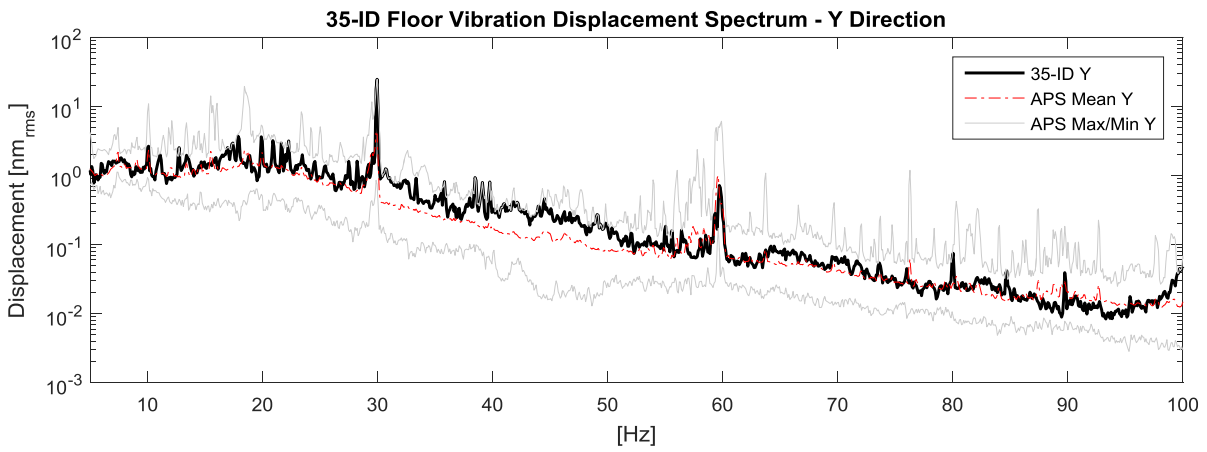
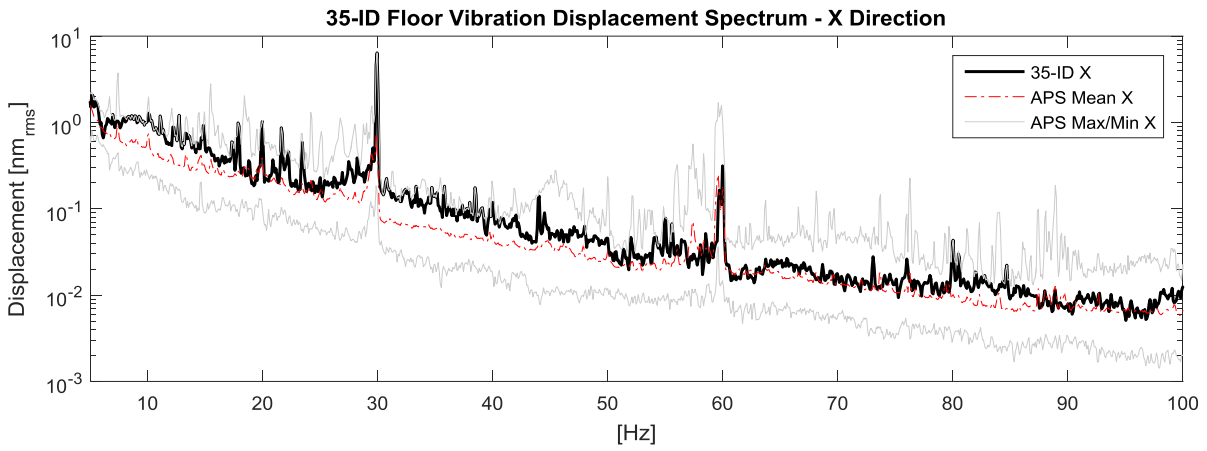












PROCEEDINGS OF SPIE

[SPIDigitalLibrary.org/conference-proceedings-of-spie](https://spiedigitallibrary.org/conference-proceedings-of-spie)

X-ray optics simulation and beamline design for the APS upgrade

Xianbo Shi
Ruben Reininger
Ross Harder
Dean Haeffner

SPIE.

X-ray optics simulation and beamline design for the APS upgrade

Xianbo Shi^a, Ruben Reininger^a, Ross Harder^a, and Dean Haeffner^a

^aAdvanced Photon Source, Argonne National Laboratory, Argonne, Illinois 60439, USA;

ABSTRACT

The upgrade of the Advanced Photon Source (APS) to a Multi-Bend Achromat (MBA) will increase the brightness of the APS by between two and three orders of magnitude. The APS upgrade (APS-U) project includes a list of feature beamlines that will take full advantage of the new machine. Many of the existing beamlines will be also upgraded to profit from this significant machine enhancement. Optics simulations are essential in the design and optimization of these new and existing beamlines. In this contribution, the simulation tools used and developed at APS, ranging from analytical to numerical methods, are summarized. Three general optical layouts are compared in terms of their coherence control and focusing capabilities. The concept of zoom optics, where two sets of focusing elements (e.g., CRLs and KB mirrors) are used to provide variable beam sizes at a fixed focal plane, is optimized analytically. The effects of figure errors on the vertical spot size and on the local coherence along the vertical direction of the optimized design are investigated.

Keywords: beamline design; X-ray optics simulation; beam coherence; zoom optics;

1. INTRODUCTION

Fourth-generation synchrotron radiation facilities with much lower emittance compared to their predecessors are being built worldwide. The Advanced Photon Source Upgrade (APS-U) project is working to replace the existing storage ring with a Multi-Bend Achromat (MBA) lattice that will increase the brightness and consequently, the coherent flux, by more than two orders of magnitude. To take full advantage of the new MBA lattice, the APS-U project includes eight feature beamlines focusing on coherence related techniques (e.g., coherence diffraction imaging, ptychography, and X-ray photon correlation spectroscopy) and high-energy applications. In addition, several existing beamlines will be upgraded to utilize the improved brightness of the APS-U source and significantly extend their experimental capabilities. Evidently, the optical design of the new and to be upgraded beamlines needs to be carefully simulated to optimize their performance with the new lattice and at the same time specify the requirements of the optical and mechanical components.

Beamline simulation normally starts with the conceptual design by applying simple analytical formulas. With the help of modern technical computing tools, such as Mathematica,¹ the analytical calculation can take into account a Gaussian beam profile, the optics acceptance (e.g., slits, mirror aperture, CRL transmission), as well as the focusing condition using geometric magnification and diffraction formulas.

In order to include a more accurate source profile, take into account optical aberrations, and the effect of non-ideal optics (e.g., mirror roughness and figure errors), dedicated ray-tracing tools, such as *SHADOW*,^{2,3} Ray,^{4,5} McXtrace,⁶ and xrt⁷ need to be used. *HYBRID*⁸ was developed at the APS to combine ray tracing and wavefront propagation. It was implemented into *SHADOWVUI*⁹ and recently in *ShadowOvi*¹⁰ in the OASYS environment.¹¹ *HYBRID* is added when the beam is clipped and/or figure errors on mirrors and gratings are present. Mirror figure errors can be included from either real metrology data or profiles that are constructed by combining cosine components with different weight and spacial frequencies.¹² One suggested software is the DABAM module¹³ in OASYS, which can provide mirror surface profiles from metrology data or scaled profiles with similar manufacture signatures. These ray-tracing tools can provide statistical information on beam intensity, spot size, divergence and energy spectra at any given position along the beamline. Furthermore, they are useful tools to specify the required finish and mechanical stability of the optical components.

Further author information: (Send correspondence to Xianbo Shi)
E-mail: xshi@aps.anl.gov, Telephone: 1-630-252-9676

The experimental techniques based on coherence rely not only on the phase-space information but also on the full knowledge of the mutual coherence of the beam. The mutual coherence function represents the correlation between electromagnetic fields at different positions and time. The propagation of the mutual coherence function is under intensive studies using different approaches. Existing tools and models include the SRW code,^{14,15} the coherent mode decomposition method,¹⁶ comsyl,¹⁷ and the Mutual Optical Intensity (MOI) model.^{18,19} These methods can provide very accurate results, but the computation cost is normally high. The MOI model was originally developed at the Shanghai Synchrotron Radiation Facility (SSRF).¹⁸ The APS and the SSRF recently extended the model to include non-ideal mirrors.¹⁹ The MOI model can provide not only the beam intensity but also the wavefront and the local coherence function at any position along the beamline in a single calculation.

In this contribution, section 2 summarizes the analytical method used in this work. Section 3 compares three optical layouts in terms of their coherence control and focusing capabilities. In section 4, the concept of zoom optics is demonstrated by using different levels of simulation.

2. THE ANALYTICAL METHOD

The analytical method is mainly useful in the conceptual and preliminary design phase of a beamline where we assume ideal optics. It can provide very fast optimization of the beamline layout with reasonable accuracy when optical aberrations (e.g., large demagnification with a spherical mirror) are not present. In this section, we summarize the basic equations and approximations used in the analytical method.

The undulator radiation from a single electron is normally approximated as a 2D symmetric Gaussian beam with the size σ_p and the divergence σ'_p given by²⁰

$$\sigma_p = \frac{\sqrt{2\lambda L_u}}{2\pi}, \quad \sigma'_p = \sqrt{\frac{\lambda}{2L_u}}, \quad (1)$$

where λ is the photon wavelength, L_u is the undulator length. Strictly speaking, the undulator beam is fully coherent transversely but not Gaussian. The emittance of the single-electron undulator radiation is $\sigma_p \sigma'_p \approx \lambda/2\pi$, instead of $\lambda/4\pi$ for a Gaussian laser beam. The electron beam is normally assumed to be Gaussian with the size of $\sigma_{e,x}$ and $\sigma_{e,y}$ and the divergence of $\sigma'_{e,x}$ and $\sigma'_{e,y}$ in the horizontal (x) and vertical (y) directions, respectively. Therefore, the total beam sizes (Σ_x , Σ_y) and divergences (Σ'_x , Σ'_y) are the convolution of the photon and the electron contributions, given by

$$\Sigma_x = \sqrt{\sigma_{e,x}^2 + \sigma_p^2}, \quad \Sigma_y = \sqrt{\sigma_{e,y}^2 + \sigma_p^2}, \quad \Sigma'_x = \sqrt{\sigma'_{e,x}{}^2 + \sigma_p'^2}, \quad \Sigma'_y = \sqrt{\sigma'_{e,y}{}^2 + \sigma_p'^2}, \quad (2)$$

If the undulator center has an offset δ_u from the electron beam waist (defined as 0), the beam sizes at a given position d are

$$\Sigma_x(d) = \sqrt{\sigma_{e,x}^2 + \sigma_p^2 + (d\sigma'_{e,x})^2 + [(d - \delta_u)\sigma'_p]^2}, \quad \Sigma_y(d) = \sqrt{\sigma_{e,y}^2 + \sigma_p^2 + (d\sigma'_{e,y})^2 + [(d - \delta_u)\sigma'_p]^2}. \quad (3)$$

The beam waists are at $d_{w,x}$ and $d_{w,y}$ where $\Sigma_x(d)$ and $\Sigma_y(d)$ in Eq. 3 achieve their minimum values in the horizontal and the vertical directions, respectively. From Eq. 3 one realizes that the beam waists could not overlap and could shift as a function of the photon energy when the insertion device is not located at the center of the straight section. In Eqs. (2) and (3), the effect of the electron beam energy spread is not considered. Apart from the numerical simulation tools (e.g., SRW and *SPECTRA*²¹), an analytical expression can be also used as a universal function to evaluate the angular and spatial distribution of the undulator radiation, which includes effects of the electron emittance and the energy spread.²²

Considering a single optics focusing system, the RMS focal size (S) and divergence (S') in each direction at the focal plane can be estimated by

$$S = \sqrt{S_{geo}^2 + S_{dif}^2 + S_{err}^2}, \quad S_{geo} = \frac{d_{oi}\Sigma_s}{d_{so}}, \quad S_{dif} = \frac{\alpha\lambda d_{oi}}{2.35\Delta}, \quad (4)$$

$$S' = \sqrt{S'_{geo}{}^2 + S'_{dif}{}^2 + S'_{err}{}^2}, \quad S'_{geo} = \frac{d_{so}\Sigma'_s}{d_{oi}}, \quad S'_{dif} = \frac{\alpha\lambda}{2.35\Delta},$$

where Σ_s and Σ'_s are the sigma size and divergence of the source in either the x or y direction as given by Eq. (2), d_{so} and d_{oi} are the source-to-optics and optics-to-image distances, the subscripts *geo*, *dif*, and *err* stand for geometric demagnification, diffraction, and errors, respectively. Δ is the aperture size defined by the optics acceptance with $\alpha=0.88$ for a rectangular aperture and $\alpha=1.22$ for a circular aperture. For a reflective mirror of length L with a grazing angle of θ , the aperture size is

$$\Delta \approx L \sin \theta. \quad (5)$$

One should note that Eq. (4) tends to overestimate the focal spot size. Normally, the diffraction terms S_{dif} and S'_{dif} are only included when the aperture size Δ is smaller than the beam size at the optics position, or the optics is cutting the beam.

The size (S_{err}) and divergence (S'_{err}) broadening due to figure errors and mechanical vibrations need to be considered separately for different types of optics. For a mirror, the surface error effects and its specification need to be discussed in terms of the power spectral density (PSD) function.¹² Ray-tracing and wavefront propagation codes are needed to accurately study mirror figure errors. When the spot size is not diffraction limited the effect of slope errors can be evaluated analytically and are given by

$$S_{err} = 2\sigma_{se}d_{oi}, \quad S'_{err} = 2\sigma_{se}, \quad (6)$$

with σ_{se} is the RMS slope error of the mirror. For the angular vibration of a mirror, σ_{se} needs to be replaced in Eq. (6) by the RMS angular vibration σ_{vib} .

The selection of a single coherent mode is usually achieved by slitting down the beam to the size of the transverse coherence length. Here we define the coherence length based on a phase-space area method. For a Gaussian laser mode with RMS size and angle width of σ and σ' , we have $\sigma\sigma' = \lambda/4\pi$. A rectangular profile of width $\delta = \sqrt{2\pi}\sigma$ has the same area as a Gaussian profile with the same amplitude. Similarly, for the divergence, $\delta' = \sqrt{2\pi}\sigma'$. Therefore, at any beam position, the coherence phase space area is given by $\delta\delta' = \lambda/2$ for the beam with rectangular size and angular profiles. Based on the van Cittert-Zernike theorem,²³ the coherence length at a distance D from an incoherent source is given by

$$L_c = \frac{\lambda}{2\Omega}, \quad (7)$$

where Ω is the angle of the source viewed from that position, $\Omega = \sqrt{2\pi}\Sigma/D$ for a Gaussian source with RMS size Σ and $\Omega = \delta/D$ for a rectangular source profile with width δ .

The transmission (T_{aper}) of a Gaussian beam with a RMS size of σ through an aperture of size Δ is given by the error function,

$$T_{aper} = \text{erf} \left(\frac{\Delta}{2\sqrt{2}\sigma} \right). \quad (8)$$

Δ can be either the aperture size or the mirror acceptance defined by Eq. (5). The mirror reflectivity R can be assumed constant along the mirror length, which can be calculated using the Fresnel formula with the Nevot-Croce factor to include the surface roughness effects.²⁴ For compound refractive lenses (CRL), the absorption of the material needs to be considered. There is no simple analytical formula, but one can use the mathematical integration directly. The transmission of a 1D CRL focusing in the x direction is given by

$$T_{lens} = \frac{1}{\sqrt{2\pi}\sigma} \int_{-\min(D_0, \Delta)/2}^{\min(D_0, \Delta)/2} \exp \left[-\frac{x^2}{2\sigma^2} - N\mu \left(\frac{x^2}{r_0} + d \right) \right] dx, \quad (9)$$

where N is the number of lenses, μ is the attenuation coefficient, r_0 is the apex radius of the parabolic lens, d is the minimum thickness between two interfaces, and D_0 is the lens diameter or the aperture in front of the lens in the x direction.

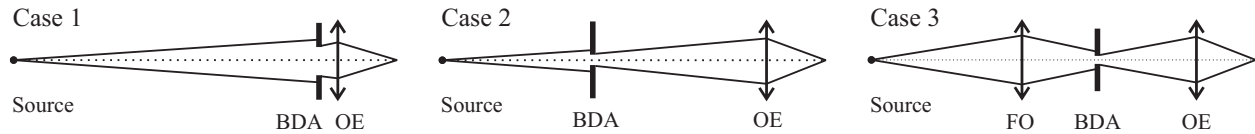


Figure 1. Schematics of three general beamline layouts for beam coherence control and focusing. BDA: beam defining aperture; OE: optical element for focusing; FO: first optics for focusing.

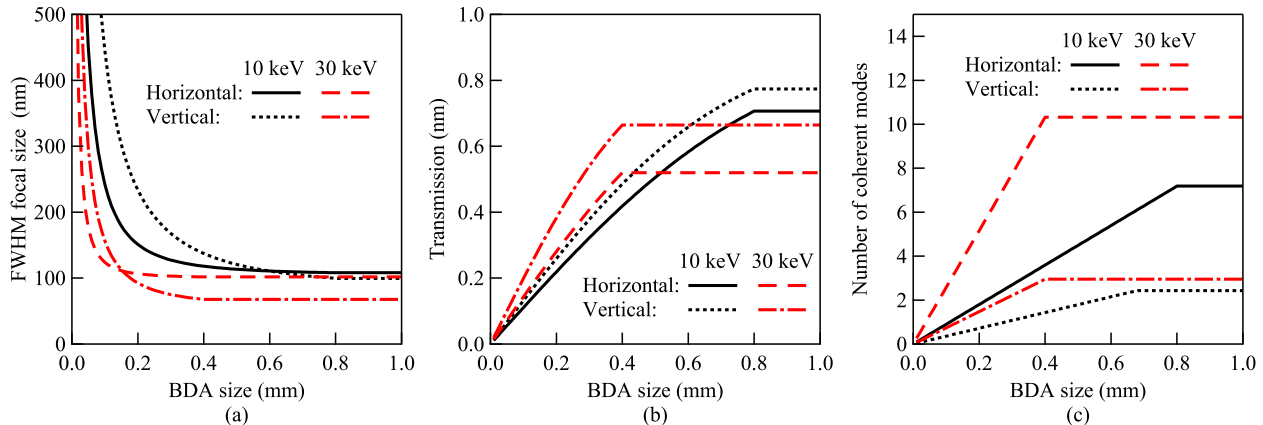


Figure 2. (a) The FWHM focal spot sizes, (b) the total transmission, and (c) the number of coherence modes calculated for case 1 in Fig. 1 with different BDA sizes at 10 keV and 30 keV.

3. ANALYTICAL COMPARISON OF FOCUSING GEOMETRIES

Three general focusing cases (cf. Fig. 1) are compared in terms of controlling beam coherence, focusing capabilities, and the vibration effects from optics using the analytical approach described in section 2. In the calculations, the horizontal and vertical focusing are treated independently. In case 1, the beam coherence is controlled by the beam defining aperture (BDA) in front of the focusing optical element (OE). The OE focuses the source directly to the sample position. In case 2, the BDA controls the coherence and defines the new source which is imaged by the OE. In case 3, the first focusing optics (FO) focuses the source into a secondary source at the BDA position. The BDA controls the coherence and the size of the secondary source. The OE focuses the secondary source to the sample position. To compare the three cases, we consider a beamline with the following parameters: the source is a 4.8 m long undulator with electron beam sizes of $\sigma_x = 14.5 \mu\text{m}$ and $\sigma_y = 2.8 \mu\text{m}$ and divergences of $\sigma'_x = 2.9 \mu\text{rad}$ and $\sigma'_y = 1.5 \mu\text{rad}$; the source-to-sample distance is 70 m; the OE is a KB mirror pair with two 200 mm long mirrors and with 90% reflectivity on each mirror; the working distance between the downstream end of OE and the sample is 100 mm.

Case 1 is studied with different BDA sizes at 10 keV and 30 keV. The mirror grazing angles are 4 mrad and 2 mrad for 10 keV and 30 keV, respectively. In order to match the beam size in both directions, the horizontal mirror is placed downstream of the vertical mirror. The results are shown in Fig. 2. At large BDA sizes, the focal size is determined by the geometric demagnification of the source (Fig. 2a), the transmission is very high (Fig. 2b) but this is at the expense of many coherent modes in the focus (Fig. 2c). When the BDA size is small, the focal spot size is broadened by diffraction, the transmission and the number of coherent modes decrease. The BDA size controls the trade-off between spot size, beam coherence, and flux. Evidently, the transmission and the number of modes reach a maximum when the diffraction is dominated by the mirror size. This occurs at a smaller BDA size for 30 keV than 10 keV since the angle of incidence is smaller at 30 keV.

In practice, the length of the two mirrors can be optimized by maximizing the quantity $T/(S_x S_y)^w$, where T is the total transmission of the focusing system. w is a weighing factor on the focal size taking into account the experimental needs. Fig. 3 shows the above quantity as a function of the length of the two mirrors with $w = 1$ and $w = 2$. The maximum is achieved at ($L_{\text{HKB}} = 155 \text{ mm}$ and $L_{\text{VKB}} = 286 \text{ mm}$) and ($L_{\text{HKB}} = 101 \text{ mm}$ and $L_{\text{VKB}} = 244 \text{ mm}$) for $w = 1$ and $w = 2$, respectively. As seen in this example, $w = 2$ yields a smaller spot size

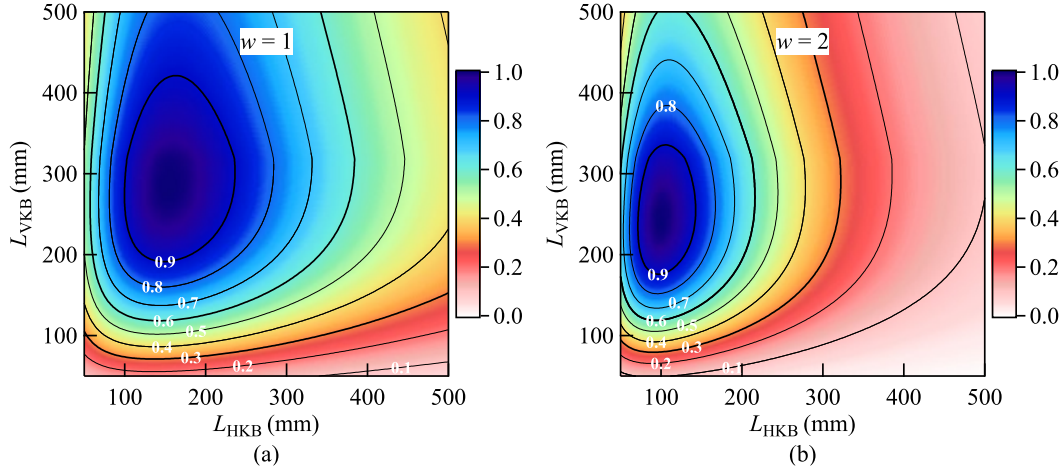


Figure 3. Normalized $T/(S_x S_y)^w$ as a function of the length of the two mirrors with (a) $w = 1$ and (b) $w = 2$. The horizontal mirror (HKB) is downstream of the vertical mirror (VKB).

($89 \times 77 \text{ nm}^2$) and a lower transmission (36%) in comparison with the $w = 1$ case ($98 \times 91 \text{ nm}^2$ and 52%). In most cases, we choose $w = 1$, where the quantity $T/(S_x S_y)$ becomes the flux density.

The disadvantage of the optical design described above (case 1) is that there is no isolation to the vibration from the source and upstream optics (e.g., the monochromator). Considering a double-crystal monochromator (DCM), the relative angular vibration between the two crystals enlarges the virtual source size (Σ_{vir}) as

$$\Sigma_{vir} = \sqrt{\Sigma^2 + (2\sigma_{vib}d_{sm})^2}, \quad (10)$$

where d_{sm} is the source-to-monochromator distance, σ_{vib} here stands for the RMS relative pitch vibration of the DCM. Fig. 4 shows the relative virtual source size broadening (Σ_{vir}/Σ) calculated using Eq. (10) due to the relative pitch vibration of a DCM, diffracting horizontally or vertically, with an RMS value of σ_{vib} . For the horizontal and vertical calculation, we used the 48 bunch mode ($\kappa = 0.99$) with $\Sigma_x = 12.9 \text{ }\mu\text{m}$ and the 324 bunch mode ($\kappa = 0.1$) with $\Sigma_y = 3.6 \text{ }\mu\text{m}$ at 30 keV, which give the smallest source size achievable in each direction with the MBA lattice design.²⁵ As seen in Fig. 4, in order to keep the source size broadening less than 10%, the relative pitch vibration needs to be smaller than 100 nrad and 30 nrad for the horizontal and vertical DCM, respectively. In general, a horizontal monochromator is preferred for the APS-U because of the less stringent stability requirement. We note on passing that a horizontal DCM with a relative pitch vibration < 25 nrad RMS over 1-2500 Hz frequency range has been recently demonstrated.²⁶

Case 2 is mostly used at the current APS in the horizontal direction. Since the horizontal beam size of the current APS (as most of the third generation synchrotron facilities) is very big, it is beneficial to use the BDA as the secondary source to achieve small focal spots. For the APS-U, this is no longer the case because of the small source size. Let's consider a BDA located at a source-to-BDA distance of d_{sb} ; and let's neglect the diffraction effects from all optics. In order to achieve smaller focal sizes than in case 1, the BDA size in case 2 should be

$$\Delta < 2.35\Sigma \frac{d_{so} - d_{sb}}{d_{so}}, \quad (11)$$

where d_{so} is the distance between the source and the focusing OE. In other words, the BDA is the preferred source only when Eq. (11) is satisfied. For a 4.8 m long undulator with a resonant energy of 10 keV, the horizontal source sizes calculated using Eq. (2) are $\Sigma_x = 273 \text{ }\mu\text{m}$ and $\Sigma_x = 15.5 \text{ }\mu\text{m}$ for the current APS and the APS-U (324 bunch mode, $\kappa = 0.1$), respectively. Based on Eq. (11) with $d_{so} = 70 \text{ m}$ and $d_{sb} = 25 \text{ m}$, we have $\Delta < 413 \text{ }\mu\text{m}$ and $\Delta < 23.5 \text{ }\mu\text{m}$ for APS and APS-U, respectively. In the existing lattice, the RMS beam size at 25 m is 403 μm , and an aperture of 413 μm accepts 39% of the beam. At APS-U, the RMS beam size at 25 m is 116 μm , and an aperture of 23.5 μm only accepts 8% of the beam. Another argument showing nothing is gained by such aperture in the APS-U is as follows: The coherence length in the horizontal direction of the APS-U at

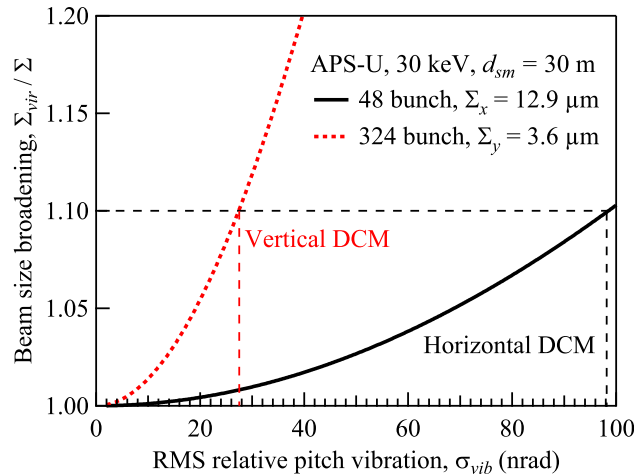


Figure 4. Virtual source size broadening (Σ_{vir}/Σ) as a function of the RMS relative pitch vibration σ_{vib} for a horizontal DCM (solid line) and a vertical DCM (dotted line) at $d_{sm} = 30$ m.

the BDA position calculated by Eq. (7) gives $L_c = 40$ μm . Therefore, the criteria $\Delta < 23.5$ μm means that the BDA selects less than one coherent mode.

Case 3 is a preferred geometry for APS-U because of the planned low emittance, high stability, high tunability, and high flexibility in beamline optimization. Normally, since the FO position is fixed (e.g., 30 m in the following calculation), the demagnification of the FO can be varied by changing the BDA position. Table 1 compares the calculated results with different BDA sizes for the FO-to-BDA distances of 30 m (FO demagnification factor of 1:1) and 10 m (FO demagnification factor of 3:1). In general, a larger BDA size provides higher flux, but larger focal sizes and lower coherence.

For the FO demagnification of 1:1, the total beamline transmission is dominated by the BDA acceptance. The focal size is dominated by the geometrical demagnification of the BDA size. Thus, the relative flux density almost remains constant.

For the FO demagnification of 3:1, the total transmission is determined by the BDA size as well as the acceptance of the OE (cf. Fig. 1). When the BDA size is smaller than $2L_c$, the focal spot is mainly due to

Table 1. Analytical calculation of the focusing property of case 3 in Fig. 1 with different BDA sizes at 10 keV. All mirrors are 200 mm long with 4 mrad grazing angle.

FO demagnification	1:1				3:1			
$L_{c,H}$ (μm) at BDA	5.3				1.8			
$L_{c,V}$ (μm) at BDA	6.4				2.1			
BDA size H (μm)	$L_{c,H}$	$2L_{c,H}$	$4L_{c,H}$	open	$L_{c,H}$	$2L_{c,H}$	$4L_{c,H}$	open
BDA size V (μm)	$L_{c,V}$	$2L_{c,V}$	$4L_{c,V}$	open	$L_{c,V}$	$2L_{c,V}$	$4L_{c,V}$	open
Focal size H (nm)	111	213	410	732	29	35	52	85
Focal size V (nm)	265	510	621	629	61	76	85	85
Total transmission	3.5%	12%	32%	66%	0.51%	3.8%	14%	32%
Relative flux density*	1	1	1	1.2	2.3	12	26	37
Number of coherent modes	1	4	9.7	18	1	2.8	6.8	12

* The relative flux density is defined as total transmission/focal size H/focal size V, and normalized to the value in the FO demagnification of 1:1 case with a BDA size of $L_{c,H} \times L_{c,V}$ (first column).

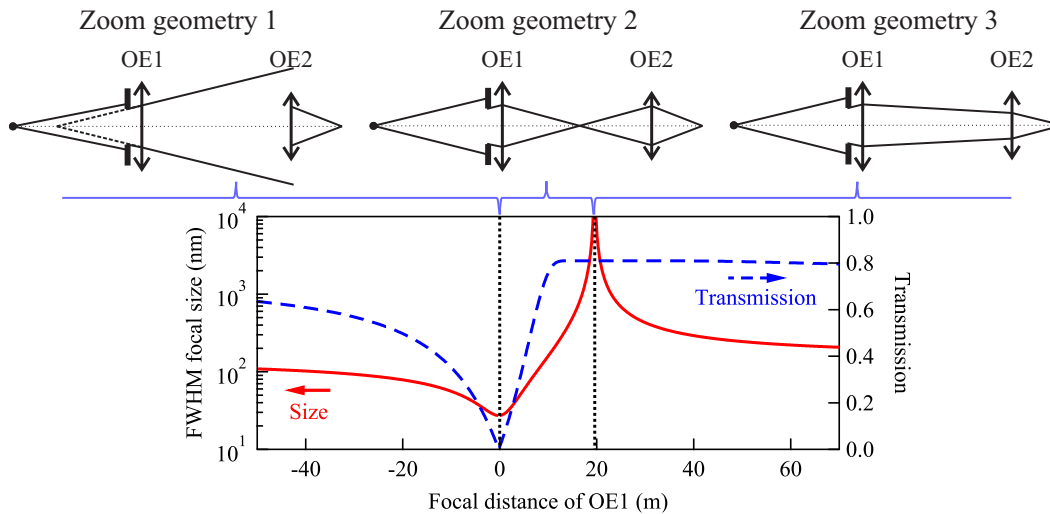


Figure 5. Three zoom geometries and the calculated focal spot sizes (solid line) and transmission (dashed line) as a function of the focal distance of OE1.

the diffraction by the finite OE size. The relative flux density is higher and increases faster than the 1:1 FO demagnification case as the BDA size increases.

In general, a larger FO demagnification ratio provides smaller beam size but lower flux. Based on the requirement of the experiment, one can optimize the beamline design by choosing the appropriate FO demagnification, or the BDA position. One should also note that a large FO demagnification design will require the accurate control of the BDA size down to one micron level, which is an engineering challenge.

The major advantage of case 3 over case 1 is that the BDA isolates the vibration effects from the source, the monochromator, and other upstream optics. Once the FO demagnification factor is determined, the two mirror length of OE can be optimized similarly as shown in Fig. 3 for case 1.

4. ZOOM OPTICS

Many APS-U beamlines have been demanding variable focal spot sizes over a large range of values to adapt to different sample sizes while maintaining the same focus position. In general, this “zoom optics” arrangement can be achieved (in each orthogonal direction) by using two focusing elements at different distances upstream of the sample. The optics can be either transmission optics (e.g., CRLs) or reflective optics (e.g., mirrors) or a combination of the two. For the APS-U, four beamlines are under design with the CRL or/and mirror based zoom system. The zoom capability of the system depends on the focusing condition and positions of the two optics.

Fig. 5 shows the three zoom geometries and the calculated horizontal focal spot size and transmission as a function of the focal distance of the first focusing optics (OE1). In this calculation, the source is the same as in Section 3; OE1 located at 50 m from the source is a 400 mm long mirror that takes the full horizontal beam; and OE2 located at 69.8 m from the source is a 200 mm long mirror; the working distance between the downstream end of OE2 and the sample is 100 mm. Both mirrors have a grazing angle of 4 mrad with a reflectivity of 90%. The zoom geometry 2 is the most common setup using deformable mirrors because that it can provide a large range of spot sizes. The creation of a real secondary source is also beneficial for cleaning the beam with slits.²⁷ The zoom geometry 3 is normally used with CRLs. By changing the number of lenses in the two sets of CRLs, discrete focal spot sizes can be achieved. In this case, using OE1 (CRL1) alone to focus directly gives the largest focal spot size, while using OE2 (CRL2) alone gives the smallest focal spot size. The zoom geometry 1 is less common but accessible if convex lenses or mirrors are used.

In this section, we take one of the APS-U feature beamlines, ATOMIC, as an example to discuss the design of a KB mirror-based zoom optics using the concept that was demonstrated previously.^{28,29} Fig. 6 shows the

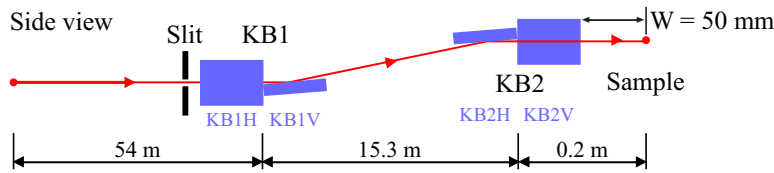


Figure 6. Schematic of the zoom KB system for the ATOMIC beamline.

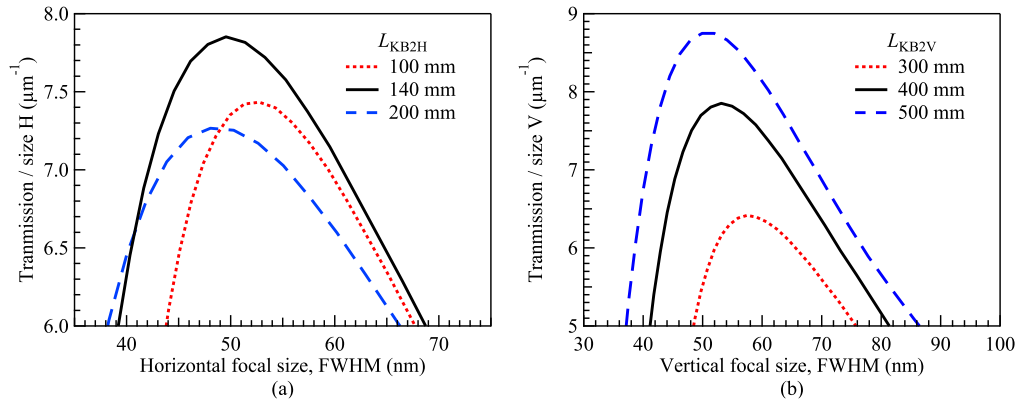


Figure 7. Calculated flux density at the focal plane of the zoom KB system as a function of the focal size with different lengths of (a) KB2H and (b) KB2V.

schematic of the zoom KB system for the ATOMIC beamline. The designed focusing range is 50 nm to 1.5 μm . The source is a 2.1 m long undulator with a position offset of $\delta_u = 1.25$ m from the center of the straight section. The beam waist is assumed to be at $d_w = 1.07$ m, and it is assumed to be Gaussian with a RMS size of 15×5.0 μm^2 (H \times V) and a RMS divergence of 6.2×5.6 μrad^2 (H \times V). The first KB pair (KB1) and the second KB pair (KB2) are located at 54 m and 69.3 m from the center of the straight section, respectively. All four mirrors are having a grazing angle of 3 mrad. There is a 10 mm separation between the edges of the two mirrors in each KB pair. The slit before KB1 used in this example is open to one coherent length in each direction as defined by Eq. 7. The length of the horizontal (KB1H) and vertical mirror (KB1V) of the KB1 pair is determined by the largest beam acceptance of the slit (lowest coherence acceptable by the experiment). Here we assume both KB1H and KB1V are 350 mm long. On the other hand, the length of the horizontal (KB2H) and vertical mirror (KB2V) of the KB2 pair is determined by optimizing the flux density for a 50 nm focus. Fig. 7(a) and (b) show the analytical calculation of the flux density as a function of the focal size with different KB2H and KB2V lengths, respectively. Increase the length of KB2H increases the total acceptance of the beam, but enlarges the focal spot size. To achieve the maximum flux density for a 50 nm focus, the optimum KB2H length is around 140 mm. On the other hand, increasing the KB2V mirror length up to 500 mm has a continuous increase in the flux density. Considering the manufacture challenges, the KB2V length will be mostly driven by the procurement. In the following simulation we use a KB2V length of 400 mm.

The figure error specification of these nano-focusing mirrors is the next essential step in the design process. It has been shown that the power spectrum density (PSD) function of the mirror figure profile is needed to simulate the effects on the focused beam.¹² Here we use the KB2V mirror as an example. The error profile of an elliptical cylinder (dabam-020 from the DABAM database,¹³ measured at Helmholtz-Zentrum Berlin) was scaled to the length of KB2V [cf. Fig. 8(a)]. *SHADOW-HYBRID* was used to calculate the effects of figure errors on the focused beam. The KB1V mirror was assumed to be a perfect elliptical cylinder focusing the source to a secondary source at 3.5 m downstream of KB1V. The KB2V mirror parameters are set to focus the secondary source to the image plane at 400 mm downstream from the center of KB2V. Fig. 8(b) shows the simulated vertical beam profiles at the focal plane with the figure error profile in Fig. 8(a) scaled to different RMS height errors. The FWHM size for the case with no slope errors [the bottom curve in Fig. 8(b)] is 46 nm, slightly less than the analytical calculations. Since the figure errors give rise to additional structures in the profile, FWHM

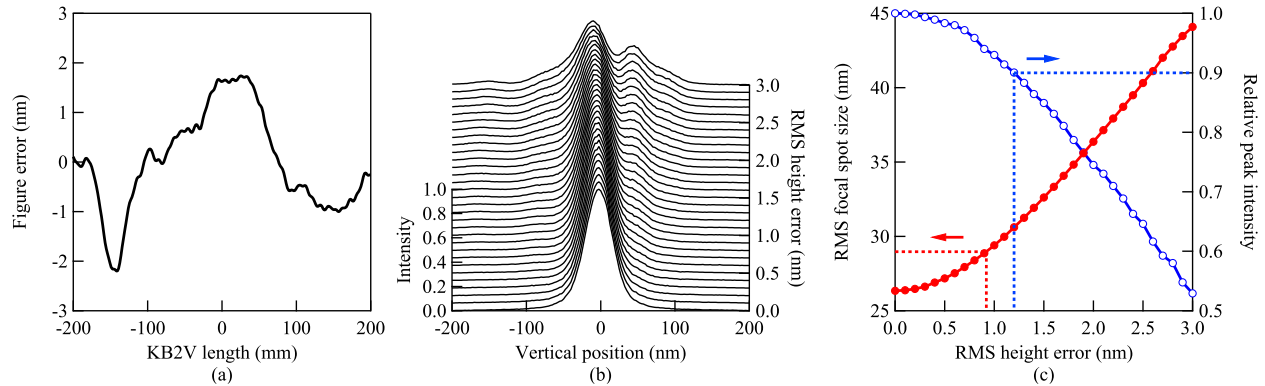


Figure 8. (a) The mirror figure error profile scaled from the dabam-020 mirror in the DABAM database¹³ with an RMS height error of 1 nm. (b) *SHADOW-HYBRID* simulations of the vertical beam profiles at the focal plane with the figure error profile in (a) scaled to different RMS height errors. (c) RMS focal spot sizes within the (-100 nm, 100 nm) range (solid circles) and relative peak intensities (open circles) of the focal beam as a function of the RMS height error extracted from (b). The dotted and dashed lines indicate the 10% increase in focal spot size and the 10% loss in peak intensity, respectively.

is not a good measure of the beam quality. Instead, the RMS size within the (-100 nm, 100 nm) range and the relative peak intensity of the focused beam were extracted from Fig. 8(b) and presented in Fig. 8(c). From Fig. 8(c) one concludes that the RMS height error needs to be less than 0.9 nm to ensure that the focal spot size broadening and the peak intensity reduction are both less than 10%. One should note that, once the figure error on KB1V is also considered, the specification of KB2V will need to be studied accordingly. Otherwise cleanup slits can be installed.²⁷

Finally, the full mutual coherence function can be simulated with more advanced codes, e.g., the MOI model.^{18,19} The source MOI, $J(y_1, y_2)$, in the y direction is simplified by using the Gaussian Schell Model (GSM),³⁰ given by

$$J(y_1, y_2) = I_0 \sqrt{\exp\left(-\frac{y_1^2 + y_2^2}{2\sigma_y^2}\right)} \exp\left[-\frac{(y_1 - y_2)^2}{2\xi_y^2}\right], \quad (12)$$

where I_0 is the maximum intensity, y_1 and y_2 are the coordinates at the source plane, and σ_y and ξ_y are the source size and transverse coherence length, respectively. The MOI source with parameters $\sigma_y = 5.0 \mu\text{m}$ and $\xi_y = 3.7 \mu\text{m}$ along the vertical direction was propagated through KB1V and KB2V using the same parameters as in the *SHADOW-HYBRID* case for three cases: without figure errors on KB2V and assuming RMS height errors of 0.5 nm and 1.0 nm on this mirror

The lower part of Fig. 9(a) shows the simulated local degree of coherence between any two points along the vertical axis (y axis) and $x = 0$ (horizontal axis) at the image plane without figure errors on KB2V. The middle part in the figure shows a cut of the two dimensional results at $y_2 = 0$. The top figure shows the beam intensity along the vertical direction obtained from the MOI propagation. As seen in the figure, the beam is highly, but not fully, coherent. The local coherence function is almost symmetric for the perfect mirrors.

Figs. 9(b) and 9(c) include the figure errors which were scaled from the profiles in Fig. 8(a) to have a RMS height error of 0.5 nm and 1.0 nm. Clearly, the figure errors redistribute the local correlation at the image plane, though the global degree of coherence is not altered.¹⁹ As seen in the upper figure of Fig. 9(b) the additional structure in the intensity graph corresponds to the region where the local degree of coherence is mostly affected. The RMS figure error of 1.0 nm (see Fig. 9(c)) has a significant effect on the local degree of coherence over all the region where the beam has intensity.

5. DISCUSSIONS AND CONCLUSIONS

We have shown the different levels of optics simulation and their usage in the design and optimization of beam-lines. The simple analytical approach can provide lots of useful information very quickly, such as the optics

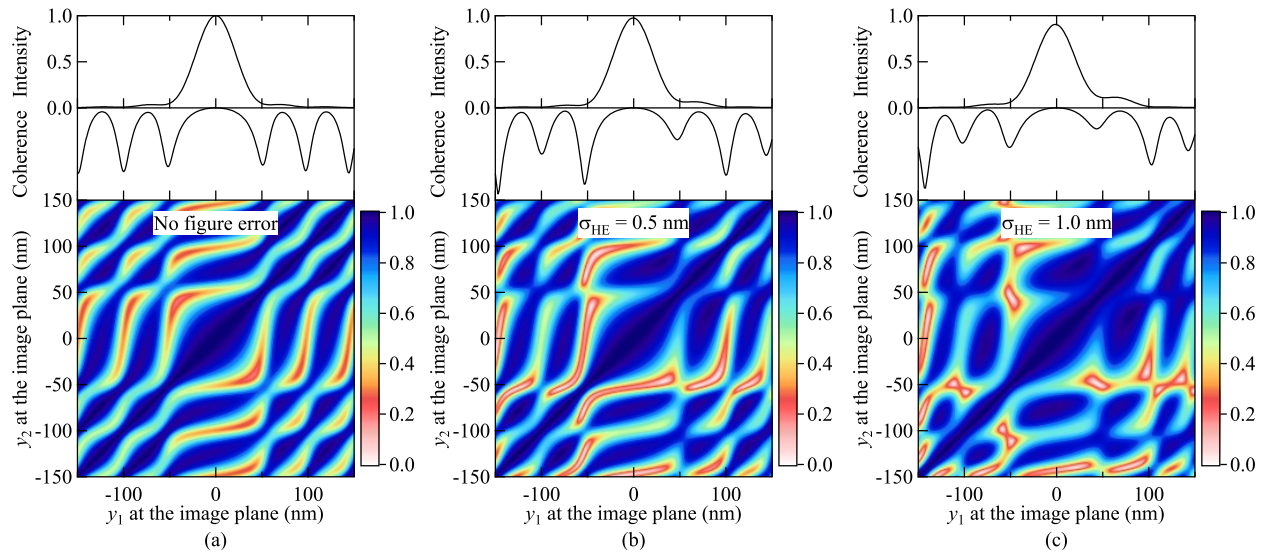


Figure 9. (Bottom figures) local degree of coherence between positions y_1 and y_2 , (middle figures) local degree of coherence between position y_1 and $y_2 = 0$, and (top figures) intensity profile in the vertical direction at the image plane calculated with the MOI model. The simulations were performed (a) without figure errors, (b) with 0.5 nm RMS height error, and (c) with 1.0 nm RMS height error on the KB2V mirror.

layout comparison, the optics position and size optimization, and the optics stability requirement. Ray-tracing and partially coherent beam propagation provides additional information for the expected beamline performance with non ideal optical elements and allows to determine the optics specification and mechanical requirements. There are general guidelines for selecting beamline layouts and optics. In this work, we show that the direct focusing geometry (case 1 in Fig. 1) and the secondary focusing geometry (case 3 in Fig. 1) are both compatible with the low-emittance storage rings. The case 3 is preferred to isolate vibrations of the upstream elements and to achieve small focal spots. Of course, the beamline design also needs to be optimized individually to accommodate requirements from various of X-ray techniques.

The zoom optics is a new concept that many beamlines are considering because of the broad range of sample environments and size scales. The initial choice of parameters is done with the analytical method, the design is confirmed and tested with *SHADOW-HYBRID* where the effect of figure errors is investigated. Finally the effect of figure errors on the local degree of coherence is investigated using the newly developed MOI model. The MOI model is currently under development to include real undulator sources and its extension to full two-dimensional calculation incorporating non-ideal optics.

This work is one of the steps towards the goal of performing simulations with the MOI model (or another development) that should allow to specify the required mirror quality that will fulfill the experimental needs on the local coherence.

Apart from the design challenge, the development of the zoom optics system also requires R&D on adaptive optics, which includes the manufacture of ultra-precision deformable mirrors, the in-situ optical metrology for monitoring the mirror surface profiles, the (non-invasive) wavefront sensor for measuring the beam shape, and the close-loop control system.

ACKNOWLEDGMENTS

This work was supported by the US Department of Energy, Office of Science, Office of Basic Energy Sciences, under Contract No. DE-AC02-06CH11357. The authors would like to thank Mr. Xiangyu Meng and Dr. Yong Wang from the Shanghai Synchrotron Radiation Facility for the useful discussion on the MOI calculation.

REFERENCES

- [1] Wolfram Research, Inc., “Mathematica 11.”
- [2] Cerrina, F., “Ray tracing of recent VUV monochromator designs,” *Proc. SPIE* **503**, 68–77 (1984).
- [3] Sanchez del Rio, M., Canestrari, N., Jiang, F., and Cerrina, F., “SHADOW3: a new version of the synchrotron X-ray optics modelling package,” *J. Synchrotron Rad.* **18**, 708–716 (2011).
- [4] Feldhaus, J., “RAY (unpublished),” (1984).
- [5] Schäfers, F., “The BESSY Raytrace Program RAY,” in [*Modern Developments in X-Ray and Neutron Optics*], Erko, A., Idir, M., Krist, T., and Michette, A. G., eds., ch. 2, 9–41, Springer-Verlag Berlin Heidelberg (2008).
- [6] Bergbäck Knudsen, E., Prodi, A., Baltser, J., Thomsen, M., Kjær Willendrup, P., Sanchez del Rio, M., Ferrero, C., Farhi, E., Haldrup, K., Vickery, A., Feidenhans'l, R., Mortensen, K., Meedom Nielsen, M., Friis Poulsen, H., Schmidt, S., and Lefmann, K., “McXtrace: A Monte Carlo software package for simulating X-ray optics, beamlines and experiments,” *J. Appl. Cryst.* **46**, 679–696 (2013).
- [7] Klementiev, K. and Chernikov, R., “Powerful scriptable ray tracing package xrt,” *Proc. SPIE* **9209**, 92090A (2014).
- [8] Shi, X., Reininger, R., Sanchez Del Rio, M., and Assoufid, L., “A hybrid method for X-ray optics simulation: combining geometric ray-tracing and wavefront propagation,” *J. Synchrotron Rad.* **21**, 669–678 (2014).
- [9] Shi, X., Sanchez Del Rio, M., and Reininger, R., “A new SHADOW update: integrating diffraction effects into ray tracing,” *Proc. SPIE* **9209**, 920911 (2014).
- [10] Rebuffi, L. and Sanchez del Rio, M., “ShadowOvi: a new visual environment for X-ray optics and synchrotron beamline simulations,” *J. Synchrotron Rad.* **23**, 1357–1367 (2016).
- [11] Sanchez del Rio, M., Rebuffi, L., Demsar, J., Canestrari, N., and Chubar, O., “A proposal for an open source graphical environment for simulating x-ray optics,” *Proc. SPIE* **9209**, 92090X (2014).
- [12] Shi, X., Assoufid, L., and Reininger, R., “How to specify super-smooth mirrors: simulation studies on nano-focusing and wavefront preserving x-ray mirrors for next-generation light sources,” *Proc. SPIE* **9687**, 968703 (2016).
- [13] Sanchez, M., Bianchi, D., Cocco, D., Glass, M., Metz, J., Raimondi, L., Rebuffi, L., Reininger, R., Shi, X., Siewert, F., Spielmann-jaeggi, S., Takacs, P., Tomasset, M., Vivo, A., and Yashchuk, V., “DABAM : an open-source database of x-ray mirrors metrology Contact author :,” *J. Synchrotron Rad.* **23**, 665–678 (2016).
- [14] Chubar, O., Berman, L., Chu, Y. S., Fluerasu, A., Hulbert, S., Idir, M., Kaznatcheev, K., Shapiro, D., Shen, Q., and Baltser, J., “Development of Partially-Coherent Wavefront Propagation Simulation Methods for 3rd and 4th Generation Synchrotron Radiation Sources,” *Proc. SPIE* **8141**, 814107 (2011).
- [15] Canestrari, N., Chubar, O., and Reininger, R., “Partially coherent X-ray wavefront propagation simulations including grazing-incidence focusing optics,” *J. Synchrotron Rad.* **21**, 1110–1121 (2014).
- [16] Singer, A. and Vartanyants, I. A., “Modelling of partially coherent radiation based on the coherent mode decomposition,” *Proc. SPIE* **8141**, 814106 (2011).
- [17] Glass, M., “Coherent modes for synchrotron light (comsyl),” <https://www.github.com/markglass/comsyl>.
- [18] Meng, X., Xue, C., Yu, H., Wang, Y., Wu, Y., and Tai, R., “Numerical analysis of partially coherent radiation at soft x-ray beamline,” *Opt. Express* **23**, 29675 (2015).
- [19] Meng, X., Shi, X., Wang, Y., Reininger, R., Assoufid, L., and Tai, R., “Mutual optical intensity propagation through non-ideal optics,” *J. Synchrotron Rad.* **24** (2017, accepted).
- [20] Elleaume, P., “Undulator radiation,” in [*Undulators, Wigglers and Their Applications*], Onuki, H. and Elleaume, P., eds., ch. 3, 69–107, CRC Press (2002).
- [21] Tanaka, T. and Kitamura, H., “SPECTRA: A synchrotron radiation calculation code,” *J. Synchrotron Rad.* **8**, 1221–1228 (2001).
- [22] Tanaka, T. and Kitamura, H., “Universal function for the brilliance of undulator radiation considering the energy spread effect,” *J. Synchrotron Rad.* **16**, 380–386 (2009).
- [23] van Cittert, P., “Die Wahrscheinliche Schwingungsverteilung in Einer von Einer Lichtquelle Direkt Oder Mittels Einer Linse Beleuchteten Ebene,” *Physica* **1**, 201–210 (1934).

- [24] Névot, L. and Croce, P., “Caractérisation des surfaces par réflexion rasante de rayons X. Application à l’étude du polissage de quelques verres silicates,” *Rev. Phys. Appl.* **15**, 761–779 (1980).
- [25] Borland, M., Sun, Y., Sajaev, V., Lindberg, R. R., and Berenc, T., “Lower emittance lattice for the advanced photon source upgrade using reverse bending magnets,” *Proc. of North American Particle Accelerator Conference (NAPAC’16)*, 877–880 (2016).
- [26] Kristiansen, P., Johansson, U., Ursby, T., and Jensen, B. N., “Vibrational stability of a cryocooled horizontal double-crystal monochromator,” *J. Synchrotron Rad.* **23**, 1076–1081 (2016).
- [27] Khakurel, K. P., Kimura, T., Nakamori, H., Goto, T., Matsuyama, S., Sasaki, T., Takei, M., Kohmura, Y., Ishikawa, T., Yamauchi, K., and Nishino, Y., “Generation of apodized X-ray illumination and its application to scanning and diffraction microscopy,” *J. Synchrotron Rad.* **24**, 142–149 (2017).
- [28] Kimura, T., Matsuyama, S., Yamauchi, K., and Nishino, Y., “Coherent x-ray zoom condenser lens for diffractive and scanning microscopy,” *Opt. Express* **21**, 9267 (2013).
- [29] Matsuyama, S., Nakamori, H., Goto, T., Kimura, T., Khakurel, K. P., Kohmura, Y., Sano, Y., Yabashi, M., Ishikawa, T., Nishino, Y., and Yamauchi, K., “Nearly diffraction-limited X-ray focusing with variable-numerical-aperture focusing optical system based on four deformable mirrors,” *Sci. Rep.* **6**, 24801 (2016).
- [30] Vartanyants, I. A. and Singer, A., “Coherence properties of hard x-ray synchrotron sources and x-ray free-electron lasers,” *New J. Phys.* **12**, 035004 (2010).